

The Interaction of Silicon Self-Interstitials and Substitutional Carbon in
Silicon Based Heterostructures

Malcolm S. Carroll

A DISSERTATION
PRESENTED TO THE FACULTY
OF PRINCETON UNIVERSITY
IN CANDIDACY FOR THE DEGREE
OF DOCTOR OF PHILOSOPHY

RECOMMENDATION FOR ACCEPTANCE
BY THE DEPARTMENT OF
ELECTRICAL ENGINEERING

JUNE 2001

© Copyright 2001 by Malcolm S. Carroll.
All rights reserved.

Welcome, O life! I go to encounter for the millionth time the reality of experience and
to forge in the smithy of my soul the uncreated conscience of my race.

J. Joyce, Portrait of an Artist as a Young Man

The Interaction of Silicon Self-Interstitials and Substitutional Carbon in Silicon-Based Heterostructures

Malcolm S. Carroll

Abstract

The increasing drive to reduce the size of transistors to sub-100 nm dimensions for overall improved performance is ultimately limited by the control over the dopant profiles. Ultra-sharp profiles can be obtained by techniques like ion-implantation or low-temperature epitaxy, making the primary challenge to control thermal diffusion of dopants during subsequent fabrication steps after the initial profile is formed. This work examines two approaches to obtain structures with sharp doping profiles: (1) reduce the dopant diffusivity through the incorporation of substitutional carbon; and (2) reduce the thermal budget of the preparation steps for silicon epitaxy creating additional growth flexibility for novel design of structures with sharp dopant profiles.

This work's contribution to the first approach include: (i) development of a new gas chemistry in the Princeton rapid thermal chemical vapor deposition (RTCVD) reactor for increased substitutional carbon incorporation in low germanium concentration films, (ii) quantification of the substitutional carbon effect on the dopant diffusivities in and near SiGeC layers, (iii) discovery and understanding that substitutional carbon reacts directly with the silicon self-interstitial in a one-for-one "kick-out" like

diffusion promotion reaction, (iv) measurement of the interstitial injection rate during oxidation, (v) demonstration that the carbon-interstitial reaction can effectively “sink” all excess interstitials introduced by ion-implantation or oxidation. Finally, a low temperature surface cleaning technique for RTCVD epitaxy was also developed as part of the second approach, which has been used to fabricate ultra-sharp phosphorus profiles.

Acknowledgements

However disproportionately small these acknowledgements are to my gratitude, I hope nevertheless that the following acknowledgements are appreciated.

Developing understanding is often necessarily a lonely pursuit but for those times that it wasn't I wish to express great appreciation for the unguarded and genuinely enjoyable exchange of perspective and insight between the students of EMD. I especially appreciate the cooperative efforts throughout my first year here with Pavel Studenkov, Jie Yao, Amlan Majumdar, and Xin Wan, the impressions of which go very deep. To all of Sturm group I am grateful for making a great laboratory atmosphere in which to work. Special thanks, goes to the RTCVD crowd, Chia-Lin Chang for his introduction to and help with the reactor and later to Eric Stewart and Haizhou Yin with whom I have enjoyed countless lively discussions ranging from siphons and gaskets to atomic hopping and Aharonov-Bohm oscillations. What fun it has been! I will miss it. To all the EMD faculty I am thankful for providing an excellent and exciting program. I am furthermore grateful to professors Lyon and Wagner for reviewing this thesis.

I am most deeply thankful to my thesis advisor Jim Sturm, from whom I have learned the most of all. The combined aggressive optimism, limitless well of insight, and rare talent to communicate it all has been a remarkable laboratory inspiration. I consider myself extremely lucky to have had the opportunity to work with such a rare combination of excellence both as innovator, researcher and teacher.

A special thanks is reserved for Tom Hebner for introducing the basketball hoop to C424-28 (although office baseball was a really bad idea!) and to Gautam Parthasarathy and Florian Pschenitzka for making a supportive and entertaining office atmosphere.

Some direct contributors to this work, which can not go without mention: M. Valenti, L. D. Lanzerotti, T. Büyüklımanlı, M. Yang, M. Gokhale, C. Rafferty, H. Rucker, J. Stangl, E. Napolitani, and D. De Salvador.

Special mention also goes to family and friends all of whom knowingly or not were giving me most appreciated support. To Irena, I am especially grateful for the serenity she has brought to my often angst-full soul. To my parents and brother I dedicate this thesis. My ways, so much a synthesis of yours, this work, so much then yours as mine.

Thank you all.

Contents

Abstract	iv
Acknowledgements	vi
1. Introduction	
1.1 Motivation	1
1.2 Outline	2
2 Growth and Characterization of Pseudomorphic $\text{Si}_{1-x-y}\text{Ge}_x\text{C}_y$	
2.1 Introduction	5
2.2 <100> SiGe Layers Pseudomorphically Strained to <100> Silicon	5
2.2.1 SiGe lattice constant	5
2.2.2 SiGe Epitaxy	7
2.3 Carbon Alloyed with Silicon and SiGe	11
2.3.1 Carbon incorporation in Silicon and SiGe	11
2.3.2 Substitutional Carbon in Silicon and Germanium	12
2.4 Measuring Substitutional Carbon	13
2.5 Carbon solid solubility in epitaxially grown Si	15

2.5.1	Carbon solid solubility in epitaxially grown SiGe	18
2.6	Low temperature epitaxy with Disilane	19
2.6.1	Si epitaxy grown by disilane	19
2.6.2	SiGe epitaxy grown by disilane	21
2.6.3	Substitutional Carbon Incorporation in Si and SiGe grown with Disilane	27
2.7	Summary	20
2.8	References	41

3 Reduced Boron Diffusion in the Presence of Substitutional Carbon

3.1	Introduction	43
3.2	Boron Diffusion in Silicon	44
3.2.1	Boron diffusion mediated by Si interstitials	44
3.2.2	Oxidation enhanced diffusion	52
3.2.3	Transient enhanced diffusion	54
3.3	Boron diffusion in SiGeC	55
3.3.1	Introduction of Cs to reduce boron diffusion	56
3.3.2	HBT Process Conditions	57
3.3.3	Extraction of diffusion constant (method)	60
3.3.4	Boron diffusivity found in SiGe and SiGeC HBT bases	61
3.4	Summary	67
3.5	References	69

4 Substitutional Carbon as a Silicon Self-Interstitial Sink

4.1 Introduction	71
4.2 Previous reports on reduced boron diffusivity in the presence of carbon	72
4.3 Phosphorus diffusion above the SiGeC layer	83
4.4 Carbon profile after annealing	88
4.5 Summary	90
4.6 References	92

5 Quantitative Measurement of the Surface Silicon Interstitial Boundary Condition and Silicon Interstitial Injection into Silicon during Oxidation

5.1 Introduction	94
5.2 Interstitial profile above buried SiGeC layers	95
5.2.1 Test structures	95
5.2.2 Extraction of Diffusivity Enhancement and Interstitial Profile	100
5.3 Boron Diffusion in a Linear Diffusivity Gradient	105
5.4 Interstitial Injection Rate	107
5.4.1 Calculation of Interstitial Injection Rate	107
5.4.2 Discussion and Comparison to Other Work	111
5.5 Summary	115
5.6 References	116

6 Diffusion Enhanced Carbon Loss from SiGeC Layers due to Oxidation

6.1 Introduction	118
6.2 Substitutional carbon loss after oxidation	119
6.3 Quantification of carbon loss	128
6.4 Double carbon layer experiment	133
6.5 Simulations	138
6.5.1 Model of carbon diffusion	138
6.5.2 Modelling of carbon diffusion profiles	142
6.6 Summary	152
6.7 References	154

7 Low-Temperature Preparation of Oxygen- and Carbon-Free Silicon and Silicon-Germanium Surfaces for Silicon and Silicon-Germanium Epitaxial Growth by Rapid Thermal Chemical Vapor Deposition

7.1 Introduction	156
7.2. Standard Growth and Characterization Procedures	158
7.2.1 Cleaning and Growth Procedures	158
7.3 Characterization of Interfaces	160
7.4. Ex-situ wet cleaning	162
7.4.1 Introduction	162

7.5. Contamination from Reactor, Load-Lock, and Laboratory Environment	168
7.5.1 Experiment	168
7.5.2 Discussion	174
7.6. In-situ Wafer Cleaning	174
7.6.1 200-400°C pre-bakes	174
7.6.2 700-800°C Bakes in Hydrogen	176
7.6.2.1 700°C Bakes in Hydrogen	177
7.6.2.2 800°C Bake in Hydrogen	180
7.6.3. Discussion	184
7.7. Summary	190
7.8 References	192
8 Conclusion	
8.1 Summary	194
8.2 Future Work	195
Appendix A	200
Appendix B	213
Publications and Presentations Resulting from this Thesis	213
Journal Articles	213

Refereed Conference Papers	214
Conference Presentations	215

Figure 2.1 Lattice constant of silicon, relaxed SiGe and strained SiGe	7
Figure 2.2 Schematic of the Princeton RTCVD	9
Figure 2.3 Growth rates of Si and SiGe	11
Figure 2.4 Substitutional C incorporation vs. temperature and partial pressure	18
Figure 2.5 O, C, Ge profiles of Si _{0.93} Ge _{0.07} layer grown using disilane	23
Figure 2.6 Ge concentration vs. germane (0.8% in hydrogen) flow rate	24
Figure 2.7 XRD rocking curve of Si _{0.93-x} Ge _{0.07} C _x layers vs. carbon content	25
Figure 2.8 PL spectra of Si _{0.93} Ge _{0.07} layer	26
Figure 2.9 O, C, Ge profiles of (a) Si _{0.926} Ge _{0.07} C _{0.004} layer and (b) Si _{0.996} C _{0.004}	28
Figure 2.10 Total C vs. methylsilane flow for both SiC and SiGeC	29
Figure 2.11 Growth rates for SiC and SiGeC grown w/ disilane	30
Figure 2.12 XRD rocking curve of Si _{0.996} C _{0.004} layer	32
Figure 2.13 Substitutional carbon vs. total carbon	33
Figure 2.14 FTIR absorbance spectra	35
Figure 2.15 Integrated absorbance vs. integrated substitutional carbon	37
Figure 3.1 Schematic representation of diffusion	46
Figure 3.2 OED of boron and phosphorus in silicon	47
Figure 3.3 Energy level diagram for interstitial-boron diffusion	48
Figure 3.4 Boron profiles in silicon before and after annealing	53
Figure 3.5. Schematic diagram of SiGe HBT structure	56
Figure 3.6 Schematic conduction band diagram reduction of collector current	57
Figure 3.7 HBT Gummel plots and collector current vs. base-collector voltage	58
Figure 3.8 B, C, Ge profiles of SiGe and SiGeC HBT's after implant	60
Figure 3.9 HBT saturation currents extracted from Gummel plots	62
Figure 3.10 B diffusivities from fitted collector saturation currents	64
Figure 3.11 Calculated Early voltages for adjusted excess interstitials	66
Figure 4.1 Test structure to study boron or phosphorus OED/TED	74
Figure 4.2 B profiles in pure Si of as-grown and annealed (897°C for 30 min)	76
Figure 4.3 B profiles from sample w/ SiGeC layer before and after annealing	78
Figure 4.4 Diffusivity enhancement vs. carbon in SiGe(C)	80
Figure 4.5 Schematic diagram of the interstitial concentration for three cases	82
Figure 4.6 TED dependence on carbon levels in SiGe(C) barrier layer	83
Figure 4.7 P profiles of before and after annealing in nitrogen	85
Figure 4.8 P profiles before and after annealing in oxygen ambient	86
Figure 4.9 Relative P diffusivity vs. carbon levels in buried Si(GeC) layers	88
Figure 4.10 C profiles before and after annealing	90

Figure 5.1. Schematic diagram of the test structures	96
Figure 5.2. B and C profiles before and after annealing (30 minutes at 850°C)	97
Figure 5.3. B and C profiles before and after annealing (120 minutes at 850°C)	98
Figure 5.4. B and C profiles before and after annealing (240 minutes at 750°C)	99
Figure 5.5. B and C profiles before and after annealing (960 minutes at 750°C)	100
Figure 5.6. Boron diffusivity enhancements for all samples and depths (750°C)	102
Figure 5.7. Boron diffusivity enhancements for all samples and depths (850°C)	103
Figure 5.8. Interstitial super-saturation at the surface	105
Figure 5.9. Simulation of boron diffusion profile in self-interstitial gradient	107
Figure 5.10. Total interstitial injected into the silicon	110
Figure 5.11. Comparison to loop-defect measurement	114
Figure 6.1 Schematic cross section of structures	120
Figure 6.2 C profiles from samples of structure A	121
Figure 6.3 C profiles from samples of structure B	122
Figure 6.4 XRD rocking curves of structure B before and after annealing at 850°C	123
Figure 6.5 Total carbon in SiGeC layer (SIMS & XRD) vs. time (structure B)	125
Figure 6.6 Summary of total carbon lost from the SiGeC layers	129
Figure 6.7 Summary of oxidation enhanced carbon loss from the SiGeC layers	130
Figure 6.8 Schematic diagram of the kick-out recycling mechanism	133
Figure 6.9 Schematic cross section of the double SiGeC layer structure	134
Figure 6.10 B and C profiles from the double buried SiGeC layer and B diffusivity	135
Figure 6.11 C profiles from the double buried SiGeC layer and simulation	144
Figure 6.12 Simulated substitutional, interstitial C and interstitial silicon profiles	145
Figure 6.13 Simulated defect currents	149
Figure 7.1. Typical PL spectrum at 77 K of a Si _{0.8} Ge _{0.2}	161
Figure 7.2. Relative SiGe/Si (PL) intensity vs. HF pH used	166
Figure 7.3. C, O and F detected at Si/SiGe interfaces	167
Figure 7.4. O, C and Ge profiles at 700°C hydrogen bake interface	170
Figure 7.5. O, C and Ge profiles at SiGe/Si test interfaces	172
Figure 7.6. Integrated O and C vs. different conditions w/out high T cleaning step	173
Figure 7.7. SiGe/Si PL from SiGe/Si after 300°C bake for different times	176
Figure 7.8. SiGe/Si PL from SiGe/Si layers after 1 min. 800°C bakes vs. pressure	181
Figure 7.9. C and O levels at SiGe/Si interfaces after 1 min., 800°C bake vs. P	183
Figure 7.10. C and O level vs. time at 800°C	184
Figure 7.11. O, C and P after interrupt growth to form ultra-sharp P layer	186

Figure 7.12. Schematic diagram of contributions in RTCVD reactor to O desorption/
absorption 188

Figure 8.1. Boron diffusivity vs. germanium content 197

Introduction

1.1 Motivation

The scaling of transistors to ever smaller sizes has created an increasing demand for control over dopant profiles in silicon devices. Production of source-drain profiles long ago moved away from solid-source in-diffusion techniques to relying on ion implantation to form tailor made dopant profiles for devices. As device dimensions have shrunk control of the dopant diffusion length has become ever increasingly critical in defining the minimum size of a device. Past generations of dopant profile engineering have relied on shrinking the thermal budgets of the device fabrication process to reduce the thermal broadening of profiles enough to remain within the limits of the design parameters for junction depth and gate-lengths. Smaller sizes have, therefore, traditionally meant lower temperatures, however, processing steps like ion implantation, which create point defects like the silicon self-interstitial that promote diffusion of common dopants like boron and phosphorus, limit the success of this approach. Ion implantation is known to produce enough excess silicon self-interstitials to enhance boron and phosphorus diffusivities thousands of times above their intrinsic diffusivities, making this effect the dominant source of diffusion at low temperature.

One novel approach to control boron diffusion has been the incorporation of carbon in Si or SiGe, which dramatically reduces the boron diffusivity and has been shown to suppress the otherwise enhanced diffusivities resulting from processing steps

like ion-implantation. For this reason, the incorporation of carbon has been used to significantly improve the thermal stability of some important device structures, e.g. the SiGeC heterojunction bipolar transistor (HBT). However, neither the mechanism responsible for the reduced diffusivity nor a quantitative understanding of the carbon effect are well established. In this work, the local and non-local effects of the presence of substitutional carbon on the boron diffusivity in Si and SiGe is quantitatively examined, the thesis of which is that the substitutional carbon reacts directly with the silicon self-interstitial in a simple one-to-one reaction (“kick-out”), depleting the local interstitial concentration and thereby reducing the local boron or phosphorus diffusivities. Also during this thesis work, a low temperature cleaning step for RTCVD epitaxy was developed for the fabrication of novel device structures. This step is useful for device structures that require the growth sequence to be interrupted so that epitaxial layer may be processed and returned to the reactor for a subsequent growth of a second epitaxial layer.

1.2 Outline

In [chapter 2](#), growth of thin $\text{Si}_{1-x-y}\text{Ge}_x\text{C}_y$ epitaxial alloy layers by rapid thermal chemical vapor deposition (RTCVD) at Princeton is reviewed. This chapter includes a discussion of new work on the introduction of the gas (disilane) into the Princeton reactor for the successful incorporation of high substitutional carbon concentrations (~ 0.5% C) in Si and low germanium fraction SiGe (7%). In [chapter 3](#), the technological moti-

variation for RTCVD grown device structures with sharp dopant profiles is illustrated by demonstrating the increased thermal stability of the SiGeC HBT over the SiGe HBT. It is found that a typical high performance design using a thin (~ 20 nm) highly boron doped base ($\sim 10^{20}$ cm $^{-3}$) is very sensitive to small boron diffusion lengths ~ 1 -2 nm that significantly reduce the electrical performance of the transistor, and increased control over the dopant profiles in the HBT structure is established by incorporating 0.5% substitutional carbon in the base. In [chapter 4](#), the enhanced boron diffusion below SiGeC layers, resulting from excess interstitials injected by oxidation or ion-implantation, is found to depend on the amount of substitutional carbon in the SiGeC layer. The dependence of the boron enhanced diffusion on substitutional carbon concentration introduces the question of how many substitutional carbon are necessary to react with a single self-interstitial? Using boron marker layers to map out the silicon self-interstitial profile under different oxidation conditions above the SiGeC layer, in [chapter 5](#), the interstitial surface boundary condition is determined and the number of injected interstitials during oxidation is quantified. In [chapter 6](#), using the injection rates determined in the previous chapter, a single injected interstitial is found to remove one substitutional carbon from the SiGeC layer in the simplest case consistent with a simple interstitial “kick-out” mechanism. Finally an indirectly related work is discussed in [chapter 7](#) on the production of sharp dopant profiles by an interrupt and regrowth technique, which depends critically on a low thermal budget cleaning step. Finally in [chapter 8](#) a summary of the results is combined with a short discussion of

some suggestions for future directions of research in this area.

Growth and Characterization of Pseudomorphic $\text{Si}_{1-x-y}\text{Ge}_x\text{C}_y$

2.1 Introduction

In the following chapters the reaction of substitutional carbon in silicon and SiGe with crystal point defects will be discussed. That work required the growth of test structures containing, pseudomorphically strained SiGeC and SiC layers, and required the characterization of the total substitutional carbon content in those alloy layers. This chapter, therefore, reviews epitaxial growth of pseudomorphically strained SiGe to silicon by rapid thermal chemical vapor deposition (RTCVD) and then discusses how the substitutional carbon concentration in SiC and SiGeC is measured in order to describe growth and characterization of SiC and SiGeC alloys at Princeton.

2.2 $\langle 100 \rangle$ SiGe Layers Pseudomorphically Strained to $\langle 100 \rangle$ Silicon

2.2.1 SiGe lattice constant

Silicon and germanium both crystallize in the diamond lattice structure, and the two elements are completely miscible forming a random alloy $\text{Si}_{1-x}\text{Ge}_x$ with a lattice constant that can vary between a_{Si} (0.5431 nm) and a_{Ge} (0.5675 nm) [1], and a bandgap

that likewise varies between the silicon and germanium bandgaps of roughly 1.1 and 0.67 eV (room temperature), respectively [2, 3]. The two elements are isoelectronic and the alloy has been very useful providing device designers a way to engineer the band-gap of devices for improved transistor performance [4]. However, because there exists a lattice constant mismatch between the SiGe alloy and silicon, the SiGe alloy layer must be strained to the silicon lattice (Si is the widely available substrate) to avoid undesirable misfit defects. If the strained layer is too thick it is energetically favorable for the strained layer to relax even at the expense of forming interface defects. Therefore, defect-free strained SiGe layers are constrained to a maximum critical thickness [5].

The SiGe layer commensurate to the silicon substrate is compressively strained in the plane parallel to the surface of the silicon, which leads to an increase of the vertical $\text{Si}_{1-x}\text{Ge}_x$ lattice constant, a_{SiGe}^\perp , in the direction perpendicular to the silicon substrate surface. The vertical lattice constant of the resulting pseudomorphically strained tetragonal crystal can be described using the elastic theory,

$$a_{\text{SiGe}}^\perp(x) = a_{\text{Si}} \cdot \left[1 + \frac{C_{11}(x) + 2C_{12}(x)}{C_{11}(x)} \cdot \frac{a_{\text{SiGe}}(x) - a_{\text{Si}}}{a_{\text{Si}}} \right] \quad (2.1)$$

where $C_{11}(x)$ and $C_{12}(x)$ are the elastic constants of $\text{Si}_{1-x}\text{Ge}_x$ and can be linearly interpolated between Si and Ge [5], and the relaxed lattice constant is approximated as the weighted average $a_{\text{SiGe}}(x) = a_{\text{Si}} \cdot (1-x) + 0.225 \cdot x \text{ \AA}$ [1, 5]. The strained and relaxed

$\text{Si}_{1-x}\text{Ge}_x$ lattice constants are plotted versus germanium concentration in Fig. 2.1. The germanium fraction of a pseudomorphically strained $\text{Si}_{1-x}\text{Ge}_x$ crystal layer with uniform composition may, thereby, be deduced from the vertical lattice constant of the layer using x-ray diffraction techniques.

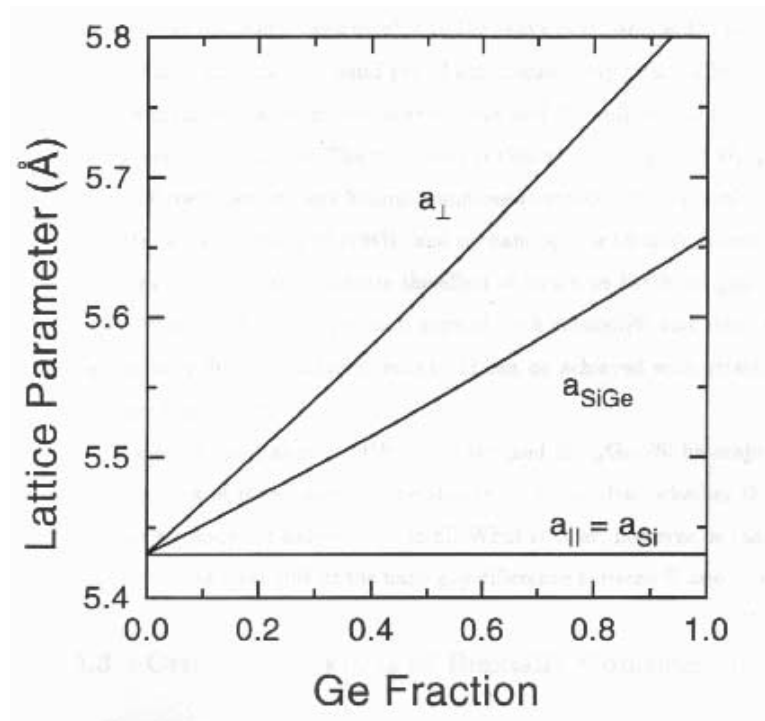


Figure 2.1 Lattice constant of silicon, relaxed SiGe and strained SiGe as a function of germanium fraction.

2.2.2 SiGe Epitaxy

On a regular basis, high quality, uniform, defect free thin films of $\langle 100 \rangle$ SiGe are grown on $\langle 100 \rangle$ silicon substrates in the Princeton RTCVD [6, 7] reactor. All test structures presented in the following chapters were grown in the Princeton reactor. A

schematic, Fig 2.2, shows the essential elements of the system. A single 4" wafer is introduced into an evacuated quartz chamber on a quartz stand through a load-lock. The load-lock is critical to maintain low oxygen backgrounds in the chamber, necessary to produce silicon with low oxygen concentrations (10^{18} cm^{-3} or less) [8]. During growth the wafer and stand are exposed to a constant flow of H_2 , 3 slpm, while maintaining the chamber pressure at 6 or 10 torr. Source gases such as dichlorosilane (SiCl_2H_2) are mixed into the H_2 to supply the silicon. The crystal growth is initiated by thermal decomposition of the source gases on the silicon wafer surface. The silicon wafer is heated radiatively by a bank of twelve 6 kW tungsten-halogen lamps located below the quartz tube capable of delivering a maximum power of 72 kW. A gold reflector assembly is situated around the quartz tube to more efficiently couple light into the wafer.

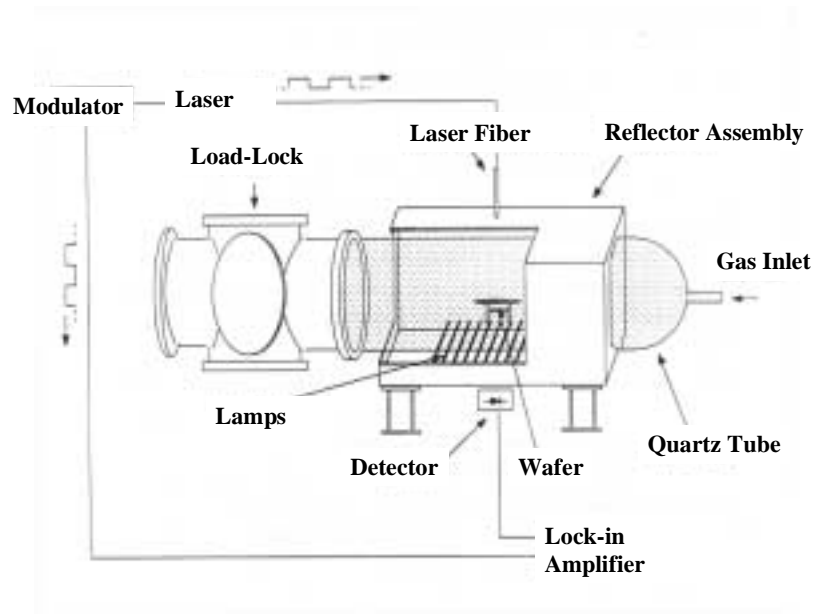


Figure 2.2 Schematic of the Princeton rapid thermal chemical vapor deposition chamber.

All gases injected into the reactor are exhausted by a rotary vane mechanical pump. The absorption of infrared light by silicon is very temperature sensitive due to the temperature dependence of the intrinsic carrier concentration and the band gap edge. Therefore, the transmission of infrared light relative to its transmission at room temperature is a measurement of the wafer temperature. Modulated infrared laser light (1.3 and 1.55 μm) is passed through the wafer during growth and detected below the wafer before and during wafer heating to determine the wafer temperature. Because the growth rate and material composition are strongly temperature dependent the temperature of the wafer must be controlled accurately within a few degrees of the desired

temperature. Throughout the growth the temperature is maintained with a feedback loop using the supplied lamp power and wafer absorption as the input and output signals, respectively [9].

Growth of the SiGe alloy is initiated by introduction of germane (0.8% GeH₄ in hydrogen) while growing silicon into the reactor atmosphere, which then decomposes with the silicon source gas resulting in a fraction of silicon lattice sites replaced with germanium. Likewise the silicon or SiGe may be doped n or p type by introducing phosphine (PH₃) or diborane (B₂H₆) to supply the phosphorus or boron, respectively. Typical growth conditions for this reactor include flows of 3 slpm H₂ and 26 sccm dichlorosilane (DCS) holding the reactor pressure at 6 or 10 torr. The resulting growth rates for these conditions at temperatures between 675-800°C are shown in Fig 2.3.

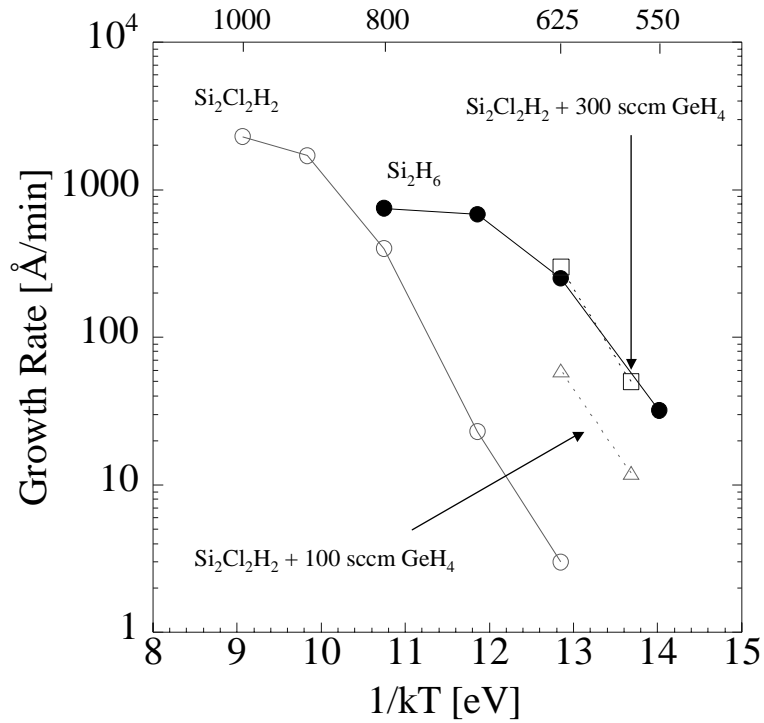


Figure 2.3 Growth rates of single crystal silicon grown using dichlorosilane at 6 torr flowing 26 sccm and 3 slpm of hydrogen with or without the addition of germane (0.8% in hydrogen) compared to the growth rate of poly-silicon grown using 3 slpm of hydrogen and 50 sccm of disilane (10% in hydrogen) at 10 torr for temperatures between 550 and 1000°C.

2.3 Carbon Alloyed with Silicon and SiGe

2.3.1 Carbon incorporation in Silicon and SiGe

Because carbon is isoelectronic to both germanium and silicon and also may crystallize in a diamond structure, carbon is also another available element to alloy with silicon and germanium, which provides more material flexibility to the device designer. Furthermore, the $\text{Si}_{1-x}\text{C}_x$ random alloy is very appealing to device designers, because there is a conduction band offset between silicon and $\text{Si}_{1-x}\text{C}_x$, making it ideal for elec-

tron-based devices [10], which is absent in the system using SiGe strained commensurately to silicon. Because the lattice constant of carbon crystallized in the diamond structure is considerably smaller than that of silicon (a_C is 0.3546 nm), carbon incorporation in SiGe to form SiGeC is also of great interest for its potential to compensate the compressive strain in SiGe layers grown commensurate to silicon [11] and therefore relax the critical thickness constraint on SiGe layers.

2.3.2 Substitutional Carbon in Silicon and Germanium

Below the solid solubility concentration in silicon or germanium carbon occupies substitutional sites and is relatively benign as *substitutional* carbon, C_s . The bulk solid solubility of carbon is high in neither silicon ($3-4 \times 10^{17} \text{ cm}^{-3}$ near the melting point [12]) nor germanium ($10^8-10^{10} \text{ cm}^{-3}$ [13]). No stable Ge-C phases are known above the solid solubility limit of germanium [14]. In silicon, silicon-carbide (SiC) is the only thermally stable phase. The precipitation of silicon-carbide in silicon with carbon concentrations far above the solid solubility is, however, known to be extremely slow without the presence of other catalytic elements such as oxygen [15]. It has been proposed that the slow precipitation of SiC is due to the unusually high surface energies required to form the silicon carbide precipitate in silicon (8000 erg cm^{-2} , 15 times that of SiO_2 precipitates) [15]. Above solid solubility in silicon or germanium, carbon has been identified in various meta-stable states including substitutional carbon, *intersti-*

tial carbon C_i , and several carbon interstitial complexes $X-C_i$ including B_S-C_i , and C_S-C_i [12]. These different states of carbon in silicon are all undesirable, except for substitutional carbon, because of their effects on the electrical properties of the material.

2.4 Measuring Substitutional Carbon

Total carbon concentrations in silicon and SiGe may be measured by secondary ion mass spectrometry (SIMS). SIMS is an often utilized tool for determining the chemical composition of semiconductors and is sensitive to carbon concentrations as low as $5 \times 10^{16} \text{ cm}^{-3}$. However, no information about the carbon state, i.e. whether it is substitutional, is obtained by this measurement. Uncertainty in SIMS obtained carbon concentrations is relatively high and is often as great as 20% [16], leading to significant difficulties in quantifying the fraction of carbon that is substitutional.

Many states of carbon in silicon are identifiable by their local vibration modes and their number in silicon are quantifiable by the strength of the absorption line. There are a large number of carbon local vibration modes, some of which are: interstitial carbon at 922 and 932 cm^{-1} ; C_S-C_i (A-Mode) at 594, 722, and 872 cm^{-1} ; C_S-C_i (B-Mode) at 842, 730, 7819 cm^{-1} (G-Line); C_i-I (silicon interstitial) 959 and 966 cm^{-1} ; C_i-O_i at 865 and 1115 cm^{-1} (the two most intense); $C_i-O_i + I$ at 940 and 1024 cm^{-1} and silicon-carbide at 796 and 960 cm^{-1} . Substitutional carbon is identifiable by its local vibrational mode at 607 cm^{-1} or 531 cm^{-1} in pure silicon or germanium, respectively.

In pure silicon the oscillator strength of the C_s mode is known and the concentration of carbon in silicon can, therefore, be measured. Using Beer's law, the peak absorption coefficient of the 605 cm^{-1} line with a full-width-half-max of 6 cm^{-1} at room temperature has been correlated to the substitutional carbon concentration as:

$$[C_s] = 1.1 \times 10^{17} \text{ cm}^{-2} \times \alpha \quad (2.2)$$

where α is measured in units of cm^{-1} with an uncertainty of $\sim 20\%$ in the proportionality constant [17]. Because there is interference with both substitutional carbon in the substrate on which the alloy layers are grown and also with a nearby absorption line, 610 cm^{-1} , due to the emission of two phonons in the silicon lattice [18], a careful procedure of subtracting a substrate IR spectrum (identical to the sample substrate) from the sample IR spectrum is required to remove the interfering components.

Quantification of substitutional carbon in layers with low total carbon areal densities (less than $1\text{-}2 \times 10^{15} \text{ cm}^{-2}$) requires a more sensitive indirect technique to determine the amount of substitutional carbon, due to the uncertainties inherent in the IR absorption technique. X-ray diffraction is an extremely sensitive method for determining the lattice constant of crystals. Because the lattice constant of silicon and $\text{Si}_{1-x}\text{Ge}_x$ shrink due to the incorporation of the smaller carbon atoms on substitutional sites in the crystal, the total amount of substitutional carbon may be deduced by the lattice constant of the SiGeC alloy layer, in a similar way as described in section 2.2.1 for strained SiGe, by using a Ge to C strain compensation ratio n (i.e. if 1 carbon atom

compensates the strain produced by 10 Ge atoms then $n = 10$). This method requires that the germanium concentration be determined by an independent measurement. Values of n range from 8-12 in the literature [19-21] due to uncertainties about the relaxed lattice constant of SiGeC and the validity of linearly interpolating the elastic constants in eq'n. 2.1, however, reasonable success has been reported with $n = 12$ [21], which is used in this work. Therefore, if a (004) Bragg reflection from a SiGeC layer with 20% Ge is located at the same angle as that expected from a SiGe layer with 8% Ge, then we conclude that the SiGeC layer contains 1% C_s .

Substitutional carbon content in $Si_{1-x}C_x$ can likewise be deduced from the tensile strained lattice constant as was described in section 2.2.1. The tensile strained lattice constant is predicted by the elastic theory as:

$$a_{SiC}^{\perp}(x) = a_{Si} \cdot \left[1 + \frac{C_{11}(x) + 2 \cdot C_{12}(x)}{C_{11}(x)} \cdot \frac{a_{SiC}(x) - a_{Si}}{a_{Si}} \right] \quad (2.3)$$

where $C_{11}(x)$ and $C_{12}(x)$ again are the elastic constants of $Si_{1-x}C_x$ and $a_{SiC}(x)$ is the relaxed lattice constant of carbon. All of these constants are linearly interpolated between silicon and diamond (i.e. using Vegard's law).

2.5 Carbon solid solubility in epitaxially grown Si

As discussed in previous sections, carbon has a very low solubility in silicon and germanium, and the only thermally stable form of carbon in silicon, above the solid-solu-

bility ($3 \times 10^{17} \text{cm}^{-3}$ at the melting point), is silicon carbide (SiC). This makes it difficult to alloy an appreciable amount of carbon on substitutional sites in either silicon or SiGe at thermal equilibrium. It takes, therefore, non-equilibrium crystal growth circumstances to alloy high concentrations of carbon on substitutional sites of silicon and SiGe. Kinetically dominated crystal growth, like that in the case of rapid thermal chemical vapor deposition or molecular beam epitaxy, indeed, has demonstrated the ability to incorporate up to 2.5% substitutional carbon in silicon and SiGe [22, 23].

The remarkably high substitutional carbon concentrations reported in epitaxially grown materials has been attributed to a higher solubility of carbon on the surface of silicon than in the silicon bulk. The surface solubility has been predicted to be as much as 10^4 times greater than that in the silicon bulk [24]. However, the fraction of carbon that is grown on substitutional sites has been found to be very sensitive to the growth conditions. Using molecular beam epitaxy (MBE), Osten et al. demonstrated that the fraction of substitutional carbon depended on two key parameters: temperature and growth rate. By increasing the growth rate, while maintaining the same material composition they showed that the fraction of substitutional carbon increased with increasing growth rate for a given temperature. Furthermore, an increase in substitutional carbon fraction was also observed as the temperature was decreased, while maintaining the same growth rate and material composition. The substitutional fraction dependence on growth rate and temperature was modeled as a competition between an energy activated time for the carbon species to move from a substitutional

surface site to a defect site and the time taken to grow a monolayer of the alloy, after which the buried carbon would be immobilized on the substitutional site [25]. The time for defect formation on the surface was proposed to be much faster than in the bulk, where the substitutional carbon is bound on the substitutional site more strongly by the additional surrounding atoms.

Initial attempts to grow $\text{Si}_{1-x}\text{C}_x$ by CVD using dichlorosilane and methylsilane for the silicon and carbon, respectively, were relatively unsuccessful incorporating at best 20% of the total carbon on substitutional sites [26]. However, growth of $\text{Si}_{1-x}\text{C}_x$ alloys containing 100% substitutional carbon were demonstrated by Mitchell et al., when using silane and methylsilane as precursors for silicon and carbon, respectively [26]. They reported that it was necessary to use low growth temperatures or high silane partial pressures to achieve high substitutional carbon fractions, Fig. 2.4. These results are consistent with Osten's work and suggest that high growth rates and low growth temperatures are indeed critical for high C_s incorporation.

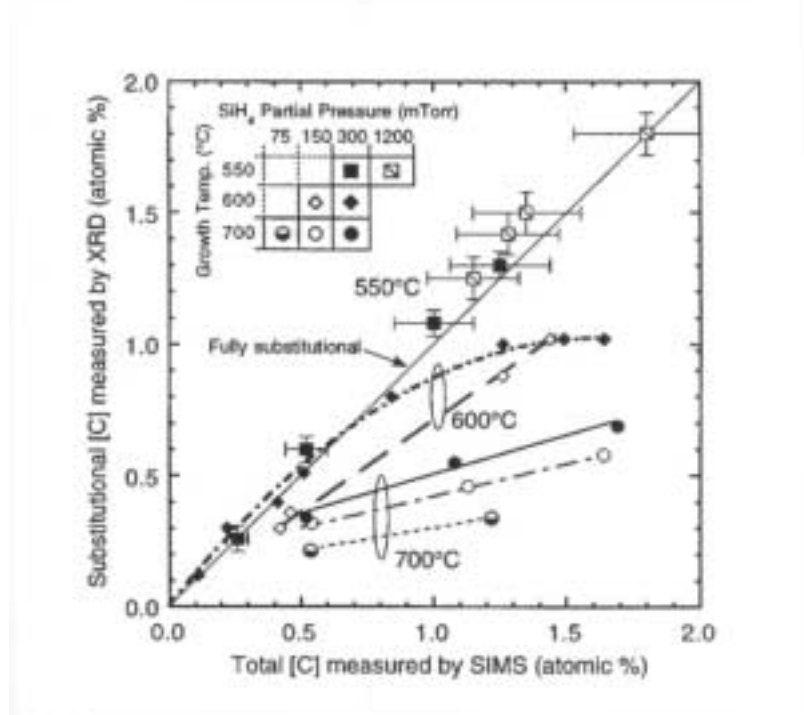


Figure 2.4 Substitutional carbon incorporation as a function of growth temperature and silane partial pressure [26].

2.5.1 Carbon solid solubility in epitaxially grown SiGe

Incorporation of substitutional carbon in SiGe has been demonstrated using CVD or MBE and carbon concentrations as high as 2.5% have been reported in the Princeton RTCVD reactor using dichlorosilane, germane, and methylsilane as source gases for silicon, germanium and carbon respectively [27]. The ability to incorporate relatively high carbon concentrations in CVD epitaxially grown SiGe films, despite using dichlorosilane gas chemistry (slow silicon growth rate) and reports of lower solid solubility in pure germanium [13] and SiGe [27], is presumably because of the catalytic-

cally enhanced growth rates (Fig 2.3) of the SiGe epitaxial films when germane is added to the gas chemistry [28]. However, incorporation of high concentrations of substitutional carbon in pure silicon and SiGe alloys with low germanium concentration until this work has remained undemonstrated at Princeton. Because it is well established that the silicon growth rate is significantly higher when using disilane for the silicon source [29, 30] and for this work it was necessary to grow $\text{Si}_{1-x}\text{C}_x$ and $\text{Si}_{1-x-y}\text{Ge}_x\text{C}_y$ with low germanium fraction we explore the introduction of disilane for higher substitutional carbon fraction in low germanium fraction alloys in the following sections.

2.6 Low temperature epitaxy with Disilane

2.6.1 Si grown by disilane

Silicon dioxide, 85 nm thick, was grown on <100> double side polished p-type silicon wafers, over which poly silicon was grown in the Princeton RTCVD reactor at temperatures between 550-800°C using disilane as a source gas. The oxidized wafers were inserted into the reactor after oxidation without additional cleaning steps. All epitaxy using disilane was done using a growth pressure of 10 torr while flowing 3 slpm of H_2 and 50 sccm of 10% disilane 90% hydrogen mixture. Growth rates for the poly-silicon (Fig 2.3) were found using the thickness after growth, determined by fitting the optical reflectance spectra of the poly-silicon on oxide using the Nanospec Automated Film Thickness System (Model No. 4100), and dividing by the deposition time. Because

the growth rate varies across the wafer surface due to temperature variation, all thickness measurements were taken within a 1 cm radius of the center of the substrate, where the temperature is measured during growth. Growth rates may be slightly higher than reported because they are calculated using the total growth time, which does not account for any poly-silicon nucleation time on the oxide. However, nucleation times reported for disilane-grown silicon on oxide for similar temperatures in other CVD systems represent less than 5% of the total growth times for each temperature examined in this experiment [31]. The polycrystalline nature of the deposited silicon was confirmed by the observation of a reflectance peak at 276 nm, which is not present in amorphous silicon [32]. All UV reflectance measurements were also done with the 4100 Nanospectrometer.

Growth rates of single crystal silicon or SiGe grown at 625°C using a flow rate of 26 sccm of dichlorosilane (3 slpm H₂, 6 torr) and germane flow rates of 0-300 sccm are compared to the growth rate of poly-silicon using disilane (Fig. 2.3). The growth rate of poly-silicon displays a strong temperature dependence increasing rapidly from 30 to 253 Å/min. for temperatures of 550°C and 625°C, respectively, which is characteristic of a reaction-limited growth. At higher growth temperature, 700-800°C, the growth rate rolls off and is not as temperature sensitive indicative of mass-transport limited growth. The growth rates of poly-silicon at lower temperatures, 550°C to 625°C, are much higher than those obtained with dichlorosilane and they are comparable to or higher than the growth rate of SiGe grown using dichlorosilane and germane,

in which substitutional carbon concentrations as high as 2.5% were achieved. If the critical conditions for high substitutional carbon incorporation are primarily high growth rates and low growth temperatures, then this is very promising for the growth of $\text{Si}_{1-x}\text{C}_x$. Indeed, in the following sections 100% substitutional carbon incorporation to form $\text{Si}_{1-x}\text{C}_x$ and low Ge (7%) content SiGeC alloys are demonstrated.

2.6.2 SiGe epitaxy grown by disilane

Pseudomorphically-strained (100) SiGe layers were grown using disilane and germane and examined using secondary ion mass spectrometry, photoluminescence and X-ray diffraction. Float-zone <100> silicon substrates polished on both sides were cleaned using a standard ex-situ and high temperature in-situ clean. Growth commenced with a thick (~0.25 μm) silicon buffer layer grown at 6 torr flowing 26 sccm dichlorosilane and 3 slpm of H_2 at 1000°C. After the buffer layer was grown and the dichlorosilane was switched off, the wafer was allowed to cool for 10 minutes. The hydrogen flow rate was maintained constant throughout the entire growth sequence even during cooling. As discussed on page 9, the temperature of the wafer is monitored by comparing the infrared transmission at the growth temperature to that at room temperature.

Because the room temperature transmission is sensitive to both changes in thickness and surface roughness it may change appreciably due to the growth of the silicon buffer layer. The growth was interrupted, therefore, at this time to remeasure the room temperature infrared transmission through the silicon wafer to improve the accuracy of

the temperature control. The wafer was then reheated to 625°C and the reactor pressure was adjusted to 10 torr, after which 50 sccm of disilane (10% Si₂H₆ in hydrogen) was injected growing silicon for 30 seconds (~15 nm) followed by the SiGe layer initiated by germane injection (27 sccm of 0.8% germane in H₂ in this case). The SiGe layers were then capped with a silicon layer grown by turning off the germane flow at 625°C for 15 seconds then turning off the disilane flow, increasing the temperature to 800°C and injecting dichlorosilane for 10 minutes maintaining the reactor pressure at 10 torr. SIMS of the SiGe layer (Fig. 2.5) show a low oxygen and carbon backgrounds, very sharp junctions and uniform germanium concentrations throughout the layer. The germanium concentration

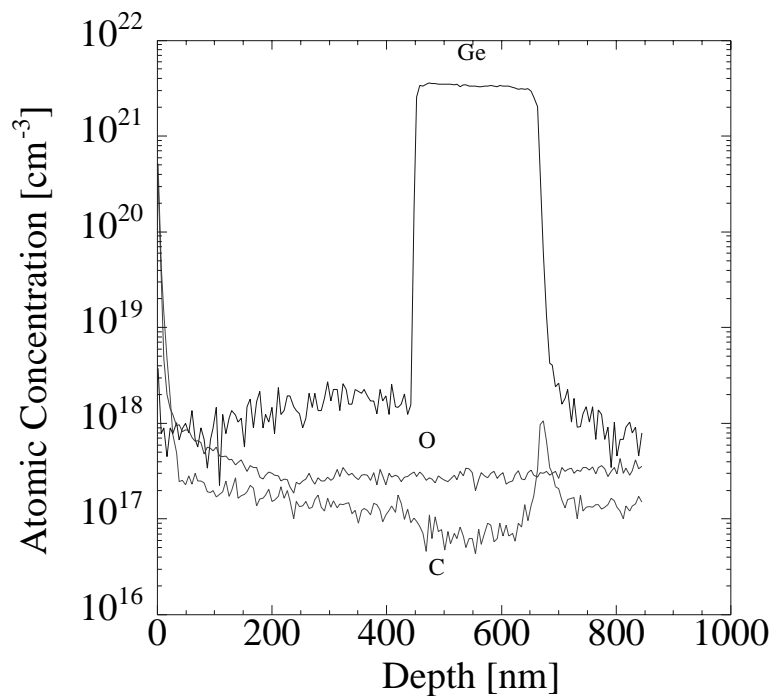


Figure 2.5 Oxygen, carbon and germanium profile obtained by SIMS of a $\text{Si}_{0.93}\text{Ge}_{0.07}$ layer grown using disilane (sample 2800). The buffer layer and cap were grown using dichlorosilane.

dependence on germane flow rate for layers grown at 625°C is compared to the concentration dependence observed in films grown with dichlorosilane at 625°C in Fig 2.6. The germanium incorporation is higher in the films grown using dichlorosilane for the same germane flows, which may be in part due to the smaller growth rate of the SiGe films grown using dichlorosilane. The growth rate for $\text{Si}_{0.93}\text{Ge}_{0.07}$ at 625°C was faster than polysilicon grown with disilane, 314 Å/min and 253 Å/min, respectively. The faster growth rate of SiGe compared to silicon is consistent with reports of cata-

lytic increased growth rates when germane is added to disilane [29] or dichlorosilane [28].

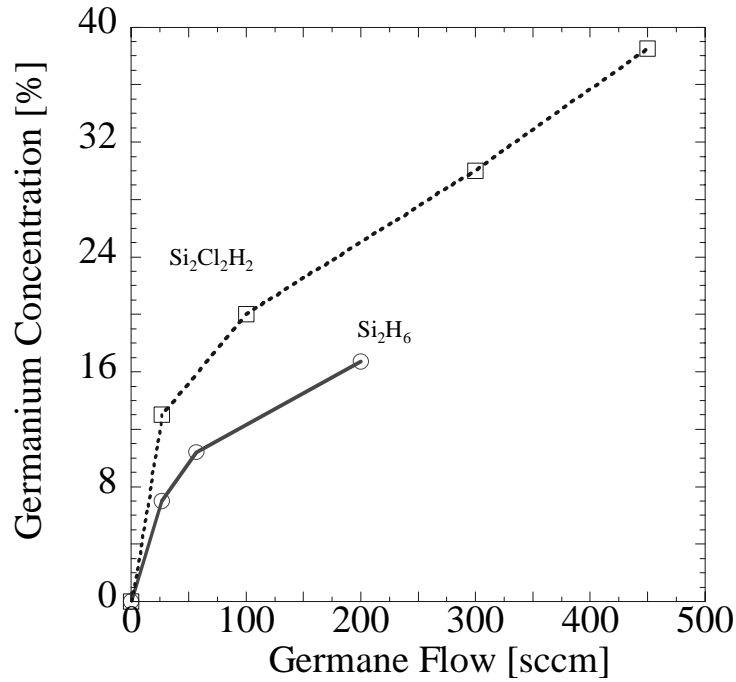


Figure 2.6 Germanium concentration of SiGe layers grown at 625°C using 3 slpm of hydrogen and dichlorosilane (26 sccm) or disilane (50 sccm, 10% in hydrogen) at 6 or 10 torr respectively as a function of germane (0.8% in hydrogen) flow rate. Germanium concentrations were determined by X-ray diffraction. Note: growth rates vary with germane flow rate.

X-ray diffraction rocking curves around the silicon 004 Bragg reflection show two peaks, Fig 2.7. The narrow satellite peak centered around -700 arcseconds is the Bragg reflection from the larger lattice constant of the crystalline SiGe layer. The peak position corresponds to a lattice constant expected from a 100% strained layer

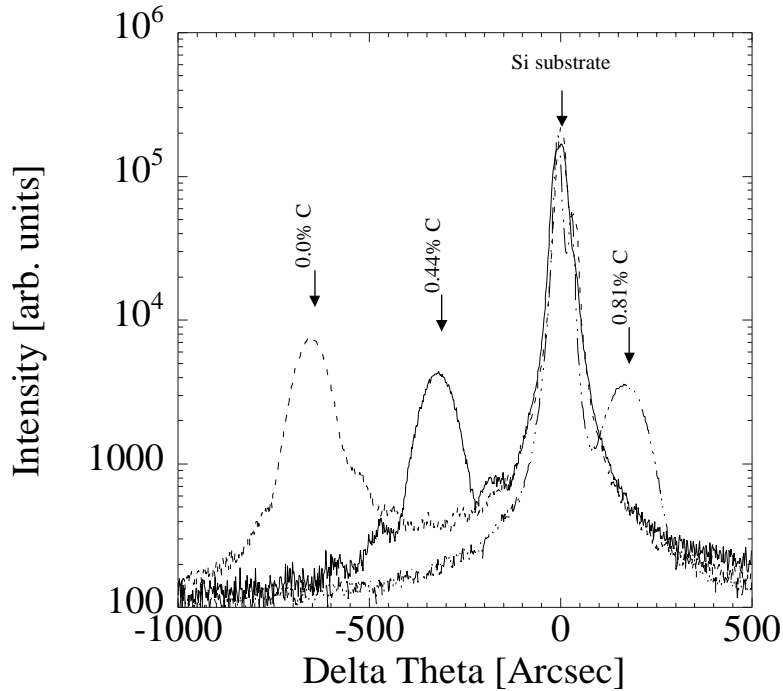


Figure 2.7 X-ray diffraction rocking curve around the (004) Bragg reflection of $\langle 100 \rangle$ $\text{Si}_{0.93-x}\text{Ge}_{0.07}\text{C}_x$ layers grown on $\langle 100 \rangle$ silicon with carbon content varying from $x=0$ - 0.0081 measured in Princeton. Note: the total carbon content is indicated above each of the corresponding $\text{Si}_{0.93-x}\text{Ge}_{0.07}\text{C}_x$ Bragg reflections (samples 2800, 2798, 2827 with increasing carbon respectively).

with 6.88% Ge agreeing well within the uncertainty of the SIMS measurement. Furthermore, photoluminescence measurements of the silicon capped $\text{Si}_{0.93}\text{Ge}_{0.07}$ layer at 77 K using an argon-ion laser as an excitation source (Fig 2.8) show two bright luminescence peaks corresponding to the transverse optical (TO) phonon replicas from the silicon substrate and the SiGe layer. The separation in energy between the silicon and SiGe TO replicas is a measure of the difference of energy bandgaps between the two

materials, ~ 56 meV. The bandgap of strained SiGe can be roughly estimated as that of silicon reduced by $\sim 7\text{-}8$ meV/ %Ge, which is consistent with XRD and SIMS measurements of the germanium concentration and the bright luminescence from the layer indicates the high quality defect free nature of the layer [6]. Note that the no-phonon line usually observed from strained SiGe layers, located 58 meV greater than the SiGe TO line (the energy of the TO phonon), is much less intense in low germanium fraction SiGe [33] and is obscured by the interference with the silicon TO line.

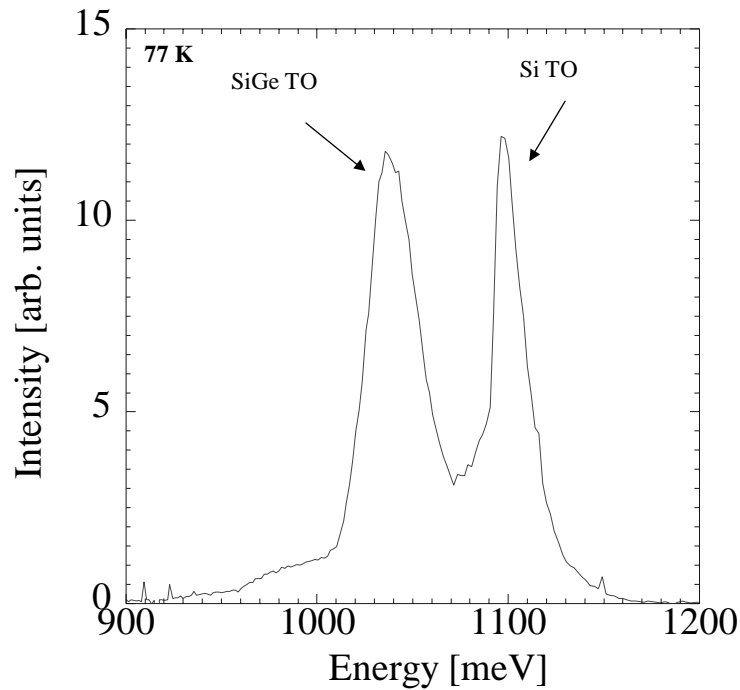


Figure 2.8 Photoluminescence (PL) spectra of a Si_{0.93}Ge_{0.07} layer (Sample #2800) capped with ~ 45 nm of silicon. The PL was done at 77 K and the excitation power was 1.5 W/cm².

2.6.3 Substitutional Carbon Incorporation in Si and SiGe grown with Disilane

Thick layers of $\text{Si}_{1-x}\text{C}_x$ and $\text{Si}_{1-x-y}\text{Ge}_x\text{C}_y$ were grown using disilane, methylsilane and germane as source gases and examined using XRD, SIMS, and PL. In the case of the $\text{Si}_{1-x-y}\text{Ge}_x\text{C}_y$ layers, the exact same procedures were followed as described in the previous section for the growth of the $\text{Si}_{1-x}\text{Ge}_x$ layers except that while growing the $\text{Si}_{1-x}\text{Ge}_x$ layers at 625°C different flows rates (0.09-1 sccm) of methylsilane were introduced into the gas stream. In the case of $\text{Si}_{1-x}\text{C}_x$, the growth procedure was identical to that described in the previous section except that germane is never introduced to the gas stream, thinner silicon caps were grown (17 minutes, 700°C, grown with dichlorosilane), and after the silicon cap was finished the wafer was annealed in-situ at 800°C for 5 minutes with a constant flow of 3 slpm of H_2 . It has been proposed, as discussed earlier, that carbon can incorporate on interstitial sites as well as substitutional sites. This final thermal anneal is done to drive any interstitial carbon out of the alloy layer and corresponds to an interstitial carbon diffusion length of ~ 1 mm [12], which is much greater than the alloy layer thickness of approximately 100-300 nm. Substitutional carbon has been shown to be thermally stable in silicon and SiGe for short (i.e. 5 minute) anneals at 800°C [25], so no appreciable loss of substitutional carbon is expected due to this thermal anneal. The concentration profiles of a $\text{Si}_{1-x-y}\text{Ge}_x\text{C}_y$ and a $\text{Si}_{1-x}\text{C}_x$ layer are shown in Fig 2.9 (a) and (b), respectively. High carbon incorporation is achieved in the SiGe and silicon layers while maintaining a very simi-

lar germanium fraction and a relatively low oxygen background. The dependence of total carbon incorporation, measured using SIMS, on methylsilane flow rate for all SiGeC and SiC samples grown using disilane is shown in Fig 2.10.

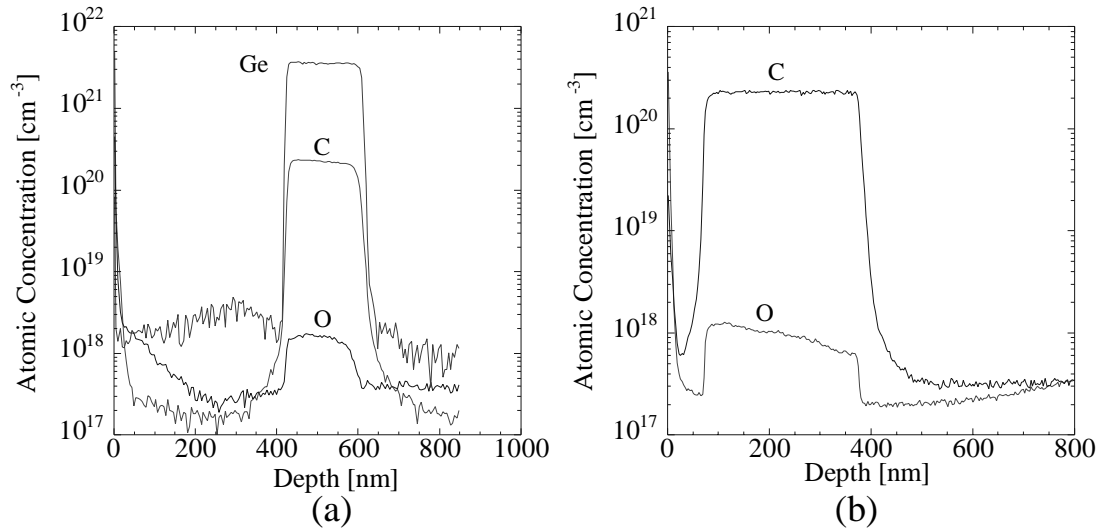


Figure 2.9 Oxygen, carbon and germanium profile obtained by SIMS of (a) Si_{0.926}Ge_{0.07}C_{0.004} layer and (b) Si_{0.996}C_{0.004} layer grown using disilane (samples 2798 and 2963, respectively). The alloy layers were grown at 625°C at 10 torr using 50 sccm of disilane (10% in hydrogen), and 3 slpm of hydrogen.

No significant germanium fraction dependence was observed on carbon concentration. However, increases in oxygen concentration have been observed in all layers with increased carbon concentration, and those layers with the highest carbon concentrations also tend to have the highest oxygen backgrounds. The cause for the increased oxygen concentrations in the carbon layers is not known at this time and could be due to contamination in the methylsilane or perhaps is caused by surface

chemistry involving carbon that is inherently more susceptible to oxygen incorporation.

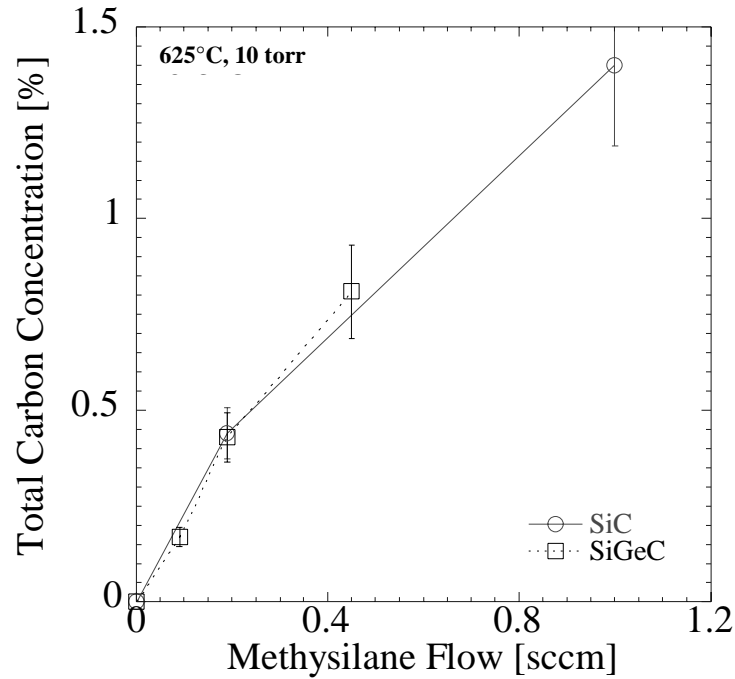


Figure 2.10 Total carbon concentrations determined by SIMS are displayed as a function of methylsilane flow rate for both SiC and SiGeC samples. Note: the methylsilane flow rates are plotted as total methylsilane content in the gas stream (not including the hydrogen content flowed at the same time)

Growth rates for SiGeC and SiC were also determined from SIMS measurements and growth times (Fig 2.11). The methylsilane flow rate has very little influence on the growth rate of the SiGeC layer. However, the growth rate of SiC with the higher methylsilane flow rate (167 Å/min) is ~ 27 % less than that grown with the lower flow rate (230 Å/min). Layer thickness can vary as much as 30% over the cen-

ter of the wafer surface due to temperature variation, therefore, it can not be concluded from just these two measurements whether the growth rate depends on the methylsilane flow rate.

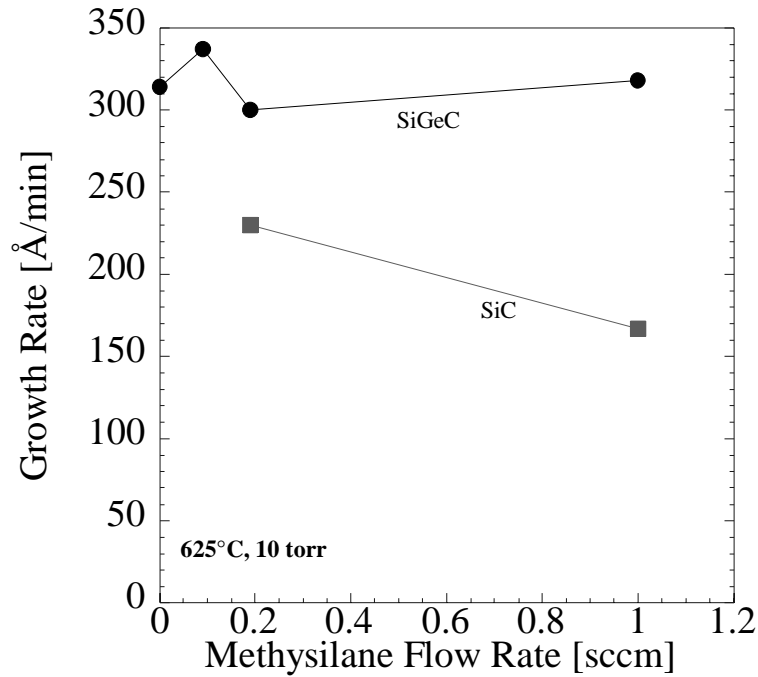


Figure 2.11 Growth rates determined from SIMS and layer growth times as a function of methylsilane flow rate for SiC and SiGeC samples. Note: the methylsilane flow rates are plotted as total methylsilane content in the gas stream (not including the hydrogen content flowed at the same time).

The X-ray diffraction rocking curves from the $\text{Si}_{0.93-x}\text{Ge}_{0.07}\text{C}_x$ structures ($x = 0.0044$ or 0.0081) are overlaid on the rocking curve obtained from the $\text{Si}_{0.93}\text{Ge}_{0.07}$ structure and a clear positive peak shift due to the strain compensation of the substitutional carbon is observed, Fig 2.7. Furthermore, the sample with 0.81% total carbon

has a lattice constant smaller than that of silicon (indicated by the positive shift from the silicon substrate Bragg reflection), demonstrating that the amount of substitutional carbon is more than enough to fully compensate the compressive strain from the 7% Ge in the layer. The intensity of photoluminescence of the TO phonon replica from the SiGeC layers at 77 K is slightly less intense than that from the SiGe layer consistent with previous reports of reduced carrier lifetimes due to carbon incorporation in SiGe [25, 34]. The x-ray rocking curve of the $\text{Si}_{0.996}\text{C}_{0.004}$ structure (measured by SIMS) has a Bragg reflection from the SiC layer 500 arcsec from the silicon Bragg reflection (Fig 2.12). The magnitude of angular shift in this case also corresponds to ~100% substitutional carbon. No photoluminescence at 77 K was observed from this layer, however, because the bandgap offset (~ 25 meV, 68 meV / %C [11]) is small it is unclear whether this is because of poor carrier confinement, high recombination due to carbon defects or perhaps a combination of both. The total carbon measured by SIMS

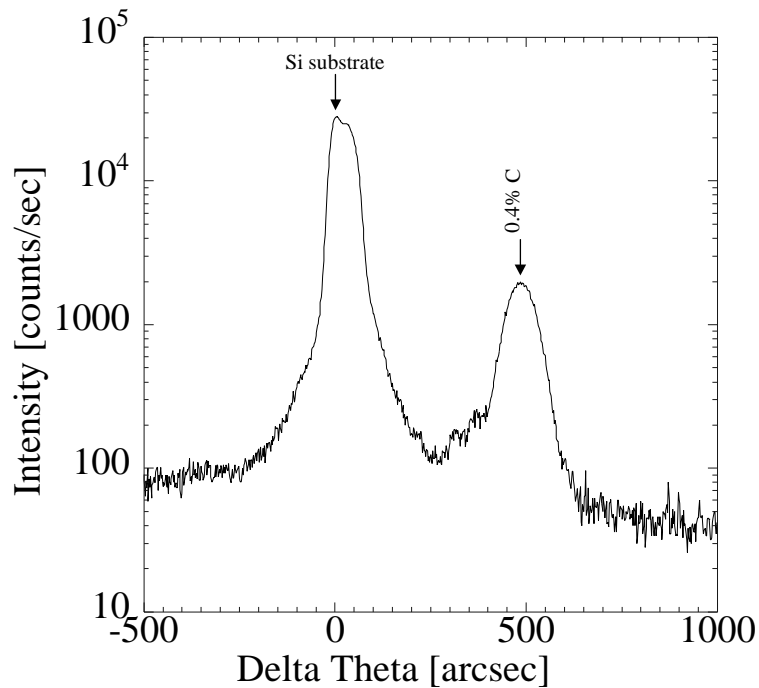


Figure 2.12 X-ray diffraction rocking curve around the (004) Bragg reflection of $\langle 100 \rangle$ $\text{Si}_{0.996}\text{C}_{0.004}$ layers grown on $\langle 100 \rangle$ silicon (sample 2963). The $\text{Si}_{0.996}\text{C}_{0.004}$ layer was grown at 625°C .

for all SiGeC and SiC samples grown using disilane are plotted against the substitutional carbon determined by XRD measurements and is summarized in Fig 2.13. The amount of substitutional carbon concentration measured in the alloy layer by XRD depends on the choice of relaxed lattice and elastic constants that are used in the linear interpolation (Vegard's law) for eq'n. 2.3. It is not known at this time what the appropriate choice of material should be for the necessary constants, e.g. diamond or silicon-carbide [21] or even whether Vegard's law is appropriate [35, 36]. Broad error bars on the substitutional carbon axis indicate the spread of possible values that can be

obtained using the range of material constants between diamond and silicon-carbide. Within the uncertainty of this measurement 100% substitutional carbon incorporation for carbon concentrations up to 0.81 % are possible.

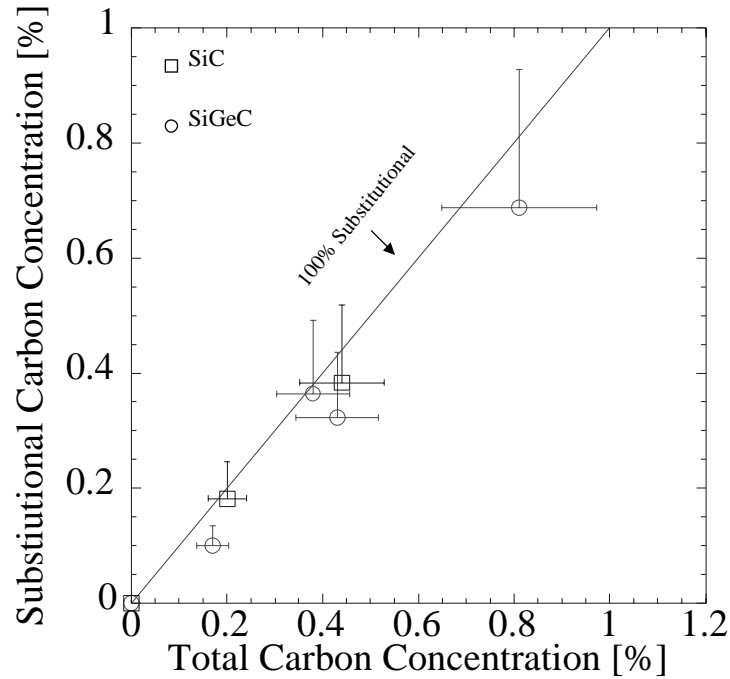


Figure 2.13 Substitutional carbon determined from Bragg reflection angular shifts (XRD) plotted against the total carbon measured in the sample using secondary ion mass spectrometry (SIMS). The solid line indicates the substitutional carbon concentration corresponding to 100% substitutional carbon in the layer. A 20% error range (due to uncertainty in SIMS) is indicated for total carbon and the range of uncertainty shown for the substitutional carbon represents different possible values that may be obtained based on Vegard's Law.

Normal incidence FTIR absorption measurements were made on 1 cm^2 samples of as-grown wafers at room temperature following the procedures outlined in the ASTM standard [17]. A typical absorbance spectra of infrared light transmitted

through a float-zone silicon sample 495 μm thick is displayed in Fig. 2.14 (a). The absorption peak centered at 610 cm^{-1} is due to the two-phonon emission in the silicon substrate. The phonon-line interferes with the substitutional carbon local mode absorption at 605 cm^{-1} and dominates the absorption signal. As discussed in section 2.4, it is necessary to subtract the two-phonon absorption from the total absorption spectra to quantitatively measure the substitutional carbon concentration in the alloy layer grown on the substrate. This can be done by measuring the absorption spectra of an identical silicon substrate and subtracting it from the absorption spectra of the alloy layer and substrate. To illustrate the sensitivity of this method to differences in the substrate thickness, the absorption of the 495 μm thick float-zone substrate is subtracted from a different 505 μm float-zone substrate. A difference of 10 microns between two different silicon float-zone substrates produces an observable contribution to the absorption signal (Fig. 2.14 (a)) and would introduce an error in the quantification of the carbon concentration. Special care, therefore, is taken to use the identical substrate for subtraction. The identical substrate for subtraction is prepared by etching the epitaxial layers off the top and bottom surface of a part of the same wafer with the epitaxially grown alloy layer (a micron or less on each side). The layers were wet-etched with a solution of $\text{HF}:\text{NH}_3:\text{H}_2\text{O}$ (1:9:10). The reflectivity is uniform between $500\text{-}1000\text{ cm}^{-1}$ after etching and is similar to the original polished substrates. The resulting difference in thickness resulted in no appreciable two-

phonon emission or carbon signals (Fig. 2.14 (b) labeled background). A typical absorption spectrum of a $\text{Si}_{1-x}\text{C}_x$ sample (Fig 2.14 (b)) after subtracting its identical substrate spectra, shows no signs of carbon in defect states (location of the defect lines are indicated on the figure (see section 2.4 for references), while exhibiting a strong absorption line at 605 cm^{-1} corresponding to the substitutional carbon local mode at room temperature.

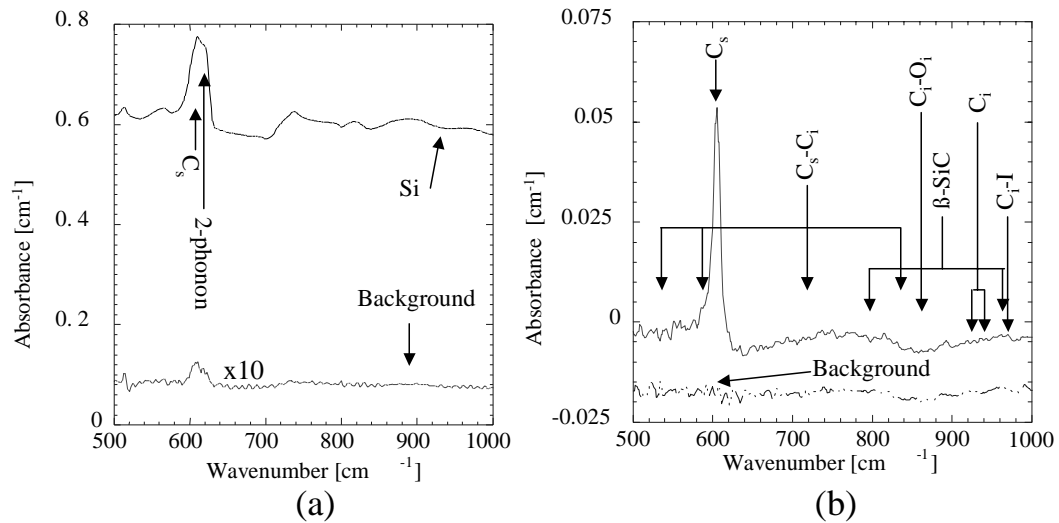


Figure 2.14 (a) Above, the FTIR absorbance spectra of a pure FZ silicon $495\ \mu\text{m}$ thick substrate (subtraction of only the surrounding nitrogen ambient). Below, the spectra of the substrate from above after subtracting the spectra of a second pure silicon FZ wafer $505\ \mu\text{m}$ thick. (b) Above, the FTIR absorbance spectra of a $300\ \text{nm}$ thick $\text{Si}_{0.996}\text{C}_{0.004}$ layer (sample 2963) grown on a FZ silicon substrate after subtracting the absorption spectra of its own substrate after wet-etching the epitaxially grown $\text{Si}_{0.996}\text{C}_{0.004}$ layer off. Below, the absorbance spectra of a Si control sample after subtracting the absorption spectra of the same silicon sample after undergoing the same wet etch used to remove the epi-layers from the other samples.

The integrated absorption measured in each of the SiGeC (squares) and SiC (circles) layers is plotted against the integrated substitutional carbon. The integrated substitutional carbon is calculated from the substitutional carbon concentration determined by X-ray diffraction (Fig. 2.13) multiplied by the thickness of the layer (determined by SIMS) and includes the contribution from both the layers grown on top and bottom surfaces of the substrate (Fig. 2.15). The measured absorption is compared to an estimate of that expected based on the absorption strength of the substitutional carbon local mode from the literature (solid line in Fig. 2.15) [17]. The relatively good agreement and the lack of signal from other common carbon defect local modes further supports the assertion that the carbon incorporated into the alloy layers using disilane and methylsilane gas chemistry is substitutional carbon.

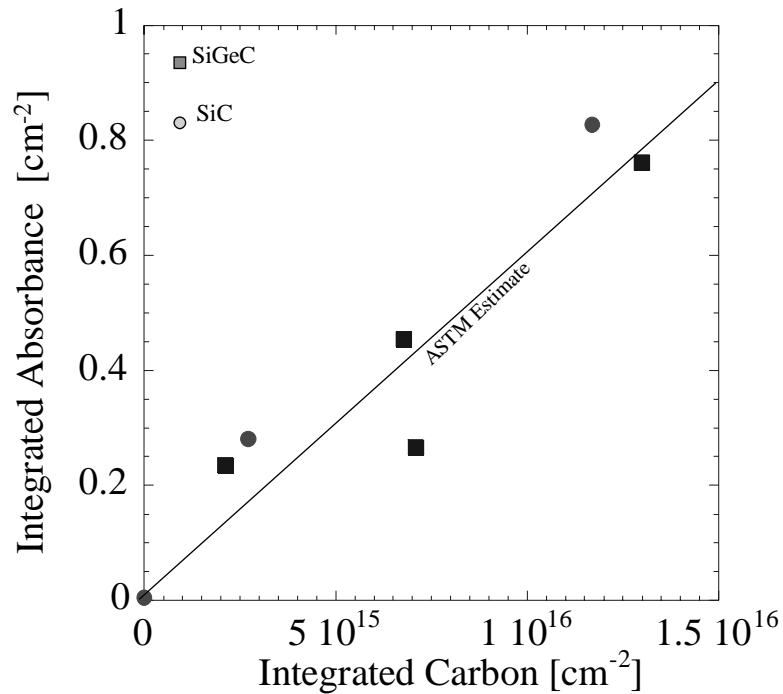


Figure 2.15 Integrated absorbance of the 605 cm^{-1} substitutional carbon local vibration mode as a function of integrated substitutional carbon deduced from XRD measurements. The solid line indicates the expected integrated absorbance from the literature [17].

The maximum substitutional carbon concentration attainable with these growth conditions remains unexamined. The highest carbon incorporation attained in the Princeton reactor was 2.5% grown at 575°C flowing 400 sccm germane [23, 34]. This resulted in a growth rate of $\sim 25\text{ \AA}/\text{min}$, which is slightly less than the expected silicon growth rate using disilane. Supposing that the amount of substitutional carbon is limited only by growth rate and temperature of the growth, $\text{Si}_{1-x}\text{C}_x$ layers with $\sim 2.5\%$ appear attainable from the Princeton reactor. Furthermore, incorporation of

substitutional carbon in silicon may be more efficient than in SiGe grown at the same temperature and growth rate because germanium is suggested to reduce the carbon solubility [13, 27]. For this work, however, such high carbon concentrations were unnecessary. $\text{Si}_{1-x}\text{C}_x$ alloys with high substitutional carbon concentrations have been reported grown using disilane in ultra high vacuum chemical vapor deposition systems but this is the first report, to the authors knowledge, of $\text{Si}_{1-x}\text{C}_x$ alloys grown using disilane in a low pressure (LP)CVD system. A table summarizing all the measurements of all disilane grown layers discussed in this chapter is included for the reader's reference (Table 2.1).

Sample	2765	2963	2799	2964	2827	2798	2825	2801	2800	2826	2824	2961
Si ₂ H ₆ Flow [sccm]	5	5	5	5	5	5	5	5	5	5	5	5
GeH ₄ Flow [sccm]	-	-	-	-	0.22	0.22	0.22	0.22	0.22	0.22	0.44	0.9
SiCH ₄ Flow [sccm]	1.0	0.19	0.19	0.19	0.45	0.21	0.19	0.09	0	0	0	0
Temp. (set-point) [Celsius] ± 10 °C	625	625	625	550	625	625	625	625	625	625	625	625
Time [min] ± 0.5	3	11	3	60	5.5	7	5.5	7	7	5.5	1	0.5
Layer Thickness [nm]	50 ± 5	305 ± 15	55 ± 8	150 ± 8	200 ± 15	210 ± 15	195 ± 10	210 ± 15	220 ± 10	-	-	-
Ge (SIMS) [atomic %] ± 2 %	-	-	-	-	6.8	7	6.8	6.4	6.5	-	-	-
Ge (XRD) [atomic %] ± 1 %	-	-	-	-	7.2	6.9	7.2	7.0	7.3	7.2	10.4	17.0
C (SIMS) [cm ⁻³] ± 20 %	7x10 ²⁰	2.2x10 ²⁰	2x10 ²⁰	1x10 ²⁰	4.05x10 ²⁰	2.15x10 ²⁰	1.9x10 ²⁰	8.5x10 ¹⁹	-	-	-	-
C (XRD) [cm ⁻³] ± 5x10 ¹⁹ cm ⁻³	-	1.92x10 ²⁰	-	9.08x10 ¹⁹	3.44x10 ²⁰	1.62x10 ²⁰	1.82x10 ²⁰	5.04x10 ¹⁹	-	-	-	-
Integrated FTIR absorb. [cm ⁻²] ± 0.04	-	0.827	-	0.281	0.762	0.454	0.266	0.235	-	-	-	-
PL (E ^{Si} -E ^{SiGe}) _{TO} [meV] ± 1 meV	x	x	x	x	x	45	x	52.5	57.5	58	85	-

Table 2.1 Summary of Samples Grown using Disilane

Note: The difference between location of the TO peaks (photon energy) coming from the SiGe(C) layer and the Si bulk is listed in the PL column. X indicates that the measurement was taken but no signal was obtained from the sample and - indicates that no measurement was taken. The volume of pure gas flow is listed rather than the total mixture, which includes hydrogen.

2.7 Summary

Growth and properties of <100> SiC and SiGeC commensurately strained to <100> silicon were discussed including the method of measuring substitutional and total carbon in the alloy layers. The growth of SiC required the introduction of disilane to the Princeton reactor, which provided the appropriate gas chemistry to incorporate relatively high concentrations of substitutional carbon in silicon and germanium poor SiGeC layers. The work on disilane is believed to be the first demonstration of disilane grown SiC with low pressure chemical vapor deposition. In the following chapter one technological advantage of carbon incorporation in the SiGe(C) base layer of the heterojunction bipolar transistor (HBT), the effect of substitutional carbon on boron diffusion, will be discussed. This motivates the discussion in later chapters of the relationship between substitutional carbon and boron diffusion.

2.8 References

- [1] J. Dismukes, L. Ekstrom, and R. Paff, *J. Phys. Chem.*, vol. 68, pp. 3021, 1964.
- [2] D. Lang, R. People, J. Bean, and A. Seargent, *Appl. Phys. Lett.*, vol. 47, pp. 1333, 1985.
- [3] R. Braunstein, A. Moore, and F. Herman, *Phys. Rev.*, vol. 109, pp. 695, 1958.
- [4] H. Kroemer, *Proc. IEEE*, vol. 70, pp. 13-25, 1982.
- [5] C. Van de Walle and R. Martin, *Phys. Rev. B*, vol. 34, pp. 5621, 1986.
- [6] J. C. Sturm, P. V. Schwartz, E. J. Prinz, and H. Manoharan, *J. Vac. Sci. Tech. B*, vol. 9, pp. 2011, 1991.
- [7] J. C. Sturm, H. Manoharan, L. Lenchyshyn, M. Thewalt, N. Rowell, J. P. Noel, and D. Houghton, *Phys. Rev. Lett.*, vol. 66, pp. 1362, 1991.
- [8] P. V. Schwartz and J. C. Sturm, *J. Electrochem. Soc.*, vol. 141, pp. 1284, 1990.
- [9] J. C. Sturm, P. M. Garone, and P. V. Schwartz, *J. Appl. Phys.*, vol. 69, pp. 542, 1990.
- [10] W. Faschinger, S. Zerlauth, G. Bauer, and L. Palmeshofer, *Appl. Phys. Lett.*, vol. 67, pp. 3933, 1995.
- [11] O. G. Schmidt and K. Eberl, *Phys. Rev. Lett.*, vol. 80, pp. 3396, 1998.
- [12] G. Davies and R. C. Newman, "Carbon in monocrystalline Silicon," in *Handbook on Semiconductors*, T. S. Moss, Ed., 1994, pp. 1558.
- [13] R. I. Scace and G. A. Slack, *J. Chem. Phys.*, vol. 30, pp. 1551, 1959.
- [14] B.-K. Yang, M. Krishnamurthy, and W. H. Weber, "Incorporation and stability of carbon during low-temperature epitaxial growth of $\text{Ge}_{1-x}\text{C}_x$ ($x < 0.1$) alloys on Si(100): Microstructural and Raman studies," *J. Appl. Phys.*, vol. 82, pp. 3287, 1997.
- [15] W. J. Taylor, W. Y. Tan, and U. Goesele, *Appl. Phys. Lett.*, vol. 62, pp. 2336, 1995.
- [16] R. G. Wilson, F. A. Stevie, and C. W. Magee, "Test method for substitutional carbon atoms of silicon by infrared absorptions," in *ASTM Book of Standards*, 1989, pp. 252 (F123-86).
- [17] ASTM, "Test method for substitutional carbon atoms of silicon by infrared absorption," in *ASTM Book of Standards*, vol. F123-86, 1986.
- [18] F. Johnson, "Lattice absorption bands in silicon," *Proc. Phys. Soc. London*, vol. 73, pp. 265, 1959.
- [19] S. C. Jain, H. J. Osten, B. Dietrich, and H. Ruecker, *Semicond. Sci. Technol.*, vol. 10, pp. 1289, 1995.
- [20] J. L. Hoyt, T. O. Mitchell, K. Rim, V. Singh, and J. F. Gibbons, *Thin Solid Films*, vol. Aug., 1997.

- [21] D. De Salvador, M. Petrovich, M. Berti, F. Romanato, E. Napolitani, A. Drigo, J. Stangl, S. Zerlauth, M. Muehlberger, F. Schaeffler, G. Bauer, and P. C. Kelires, *Phys. Rev. B*, vol. 61, pp. 13005, 2000.
- [22] K. Brunner, K. Eberl, and W. Winter, *Phys. Rev. Lett.*, vol. 76, pp. 303, 1996.
- [23] C.-L. Chang, A. St. Amour, and J. C. Sturm, *Appl. Phys. Lett.*, vol. 70, pp. 1557, 1997.
- [24] J. Tersoff, *Phys. Rev. Lett.*, vol. 74, pp. 5080, 1995.
- [25] J. H. Osten, *Thin Solid Films*, vol. 367, pp. 101-111, 2000.
- [26] T. O. Mitchell, J. L. Hoyt, and J. F. Gibbons, *Appl. Phys. Lett.*, vol. 71, pp. 1688, 1997.
- [27] J. P. Liu and H. J. Osten, *Appl. Phys. Lett.*, vol. 76, pp. 3546, 2000.
- [28] P. M. Garone, J. C. Sturm, P. V. Schwartz, S. A. Schwartz, and B. J. Wilkens, *Appl. Phys. Lett.*, vol. 56, pp. 1275, 1990.
- [29] T. I. Kamins and D. J. Meyer, *Appl. Phys. Lett.*, vol. 61, pp. 90, 1992.
- [30] C. Li, S. John, and E. Quinones, *J. Vac. Sci. Technol. A*, vol. 14, pp. 170, 1996.
- [31] Y. Z. Hu, D. J. Diehl, C. Y. Zhao, C. L. Wang, Q. Liu, A. Irene, K. N. Christensen, D. Venable, and D. M. Maher, *J. Vac. Sci. Technol. B*, vol. 14, pp. 744, 1996.
- [32] K. Pangal, "Hydrogen-Plasma-Enhanced Crystallization of Hydrogenated Amorphous Silicon Films: Fundamental Mechanisms and Applications," in *Electrical Engineering*. Princeton: Princeton University, 1999.
- [33] V. Venkataraman, "Physics and Applications of Si/SiGe Modulation Doped Structures," in *Electrical Engineering*. Princeton: Princeton University, 1994.
- [34] C.-L. Chang, "Properties and Applications of Crystalline SiGeC alloys," in *Electrical Engineering*. Princeton: Princeton University, 1998.
- [35] J. Martins and A. Zunger, *Phys. Rev. Lett.*, vol. 56, pp. 1400, 1986.
- [36] P. C. Kelires, *Phys. Rev. B.*, vol. 75, pp. 8785, 1997.

Reduced Boron Diffusion in the Presence of Substitutional Carbon

3.1 Introduction

In the previous chapter the growth and characterization of $\text{Si}_{1-x-y}\text{Ge}_x\text{C}_y$ was described. In this chapter boron diffusion and the effect of substitutional carbon on boron diffusion in the base of the $\text{Si}_{1-x-y}\text{Ge}_x\text{C}_y$ heterojunction bipolar transistor (HBT) will be examined. This chapter includes a discussion of the microscopic model of boron diffusion in silicon, i.e. the role of silicon interstitials in solid-state diffusion of boron in silicon, and a quantitative examination of the effect of incorporation of substitutional carbon on the boron diffusivity in $\text{Si}_{1-x-y}\text{Ge}_x\text{C}_y$. This highlights the technological importance of controlling boron diffusion in the SiGe(C) HBTs. The introduction of substitutional carbon is found to significantly reduce the boron diffusivity improving the performance of the HBT, which motivates later chapters examining the detailed reaction between the substitutional carbon atoms and silicon interstitial. The work in this chapter was published largely in reference [1].

3.2 Boron Diffusion in Silicon

3.2.1 Boron diffusion mediated by Si interstitials

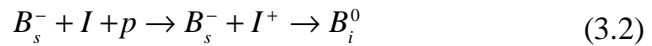
The random thermal motion of particles is described by diffusion theory. Diffusion has been extensively studied in various different states of matter, i.e. gas, liquid and in solids. Although diffusion theory is over a hundred years old and diffusion of boron in silicon has been technologically important for many decades, the detailed mechanisms that produce boron diffusion are still not completely understood. The description of boron diffusion that follows [2] is a predictive theory that adequately agrees with experiment in a vast regime of annealing conditions and is therefore used in many common process simulators, e.g. TSUPREM4 (commercially offered by Avant) or PROPHET [3].

Boron is known to dissolve onto the substitutional lattice sites of silicon when the concentration is below its solid solubility, and is designated as boron in the substitutional state B_s . The boron atom is relatively strongly bound in this state and is considered immobile, therefore the diffusivity of the B_s is for all intents and purposes zero. Early experiments using electron paramagnetic resonance (EPR) identified a boron atom that shares the same site as a silicon atom, named an Interstitials, which is mobile [4, 5]. It has been assumed, then, that the observed boron diffusion is mediated by the mobile boron defect state, B_i , that has non-zero diffusivity. The mobile boron defect state is formed when a silicon point defect, i.e. silicon vacancy or interstitial atom, is captured by the substitutional boron atom.

The observed intrinsic diffusivity results, therefore, from the B_s reaction with the intrinsic population of free silicon point defects, leading to the random thermal motion of the mobile B_i defects. The point defect responsible for boron diffusion in the temperature range of $700^\circ\text{C} < T < 900^\circ\text{C}$, which is considered in this work, has been experimentally determined as the silicon interstitial atom in various charge states [6, 7] (Fig. 3.1). The chemical reaction leading to the negatively charged defect is expressed as:



where B_s^- is the ionized substitutional boron atom and I is the silicon interstitial. It has also been experimentally determined that the boron diffusivity is linearly dependent on the hole concentration at hole concentrations above the intrinsic concentration. This has led to the proposal of an overall neutral mobile defect formed between a positively charged interstitial and a negatively charged ionized dopant [8-10]:



where p is a hole, I^+ is a silicon interstitial with a hole localized on it, and B_i^0 is the resulting neutral mobile boron defect.

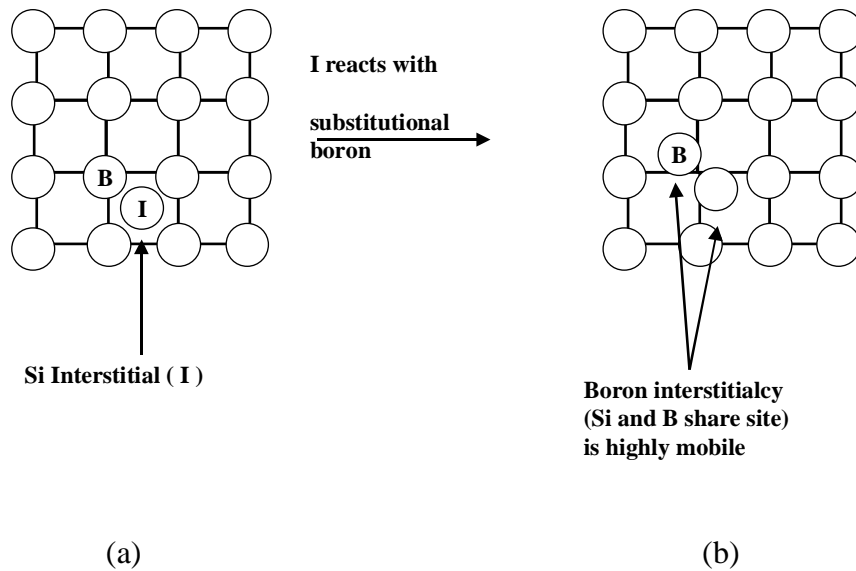


Figure 3.1 Schematic representation of (a) an interstitial silicon atom near a substitutional boron atom in a silicon lattice (for diagrammatic simplicity a square lattice is used) and (b) the resulting mobile boron interstitialcy formed by the binding of the interstitial silicon atom to a boron.

The temperature dependence of the intrinsic boron diffusivity is described well over a large temperature range by a thermal activation energy of ~ 3.4 eV [2], plotted in Fig. 3.2 (b). The activation energy describes the combined formation energy of the mobile defect and the boron defect's migration energy. The energy of formation of an

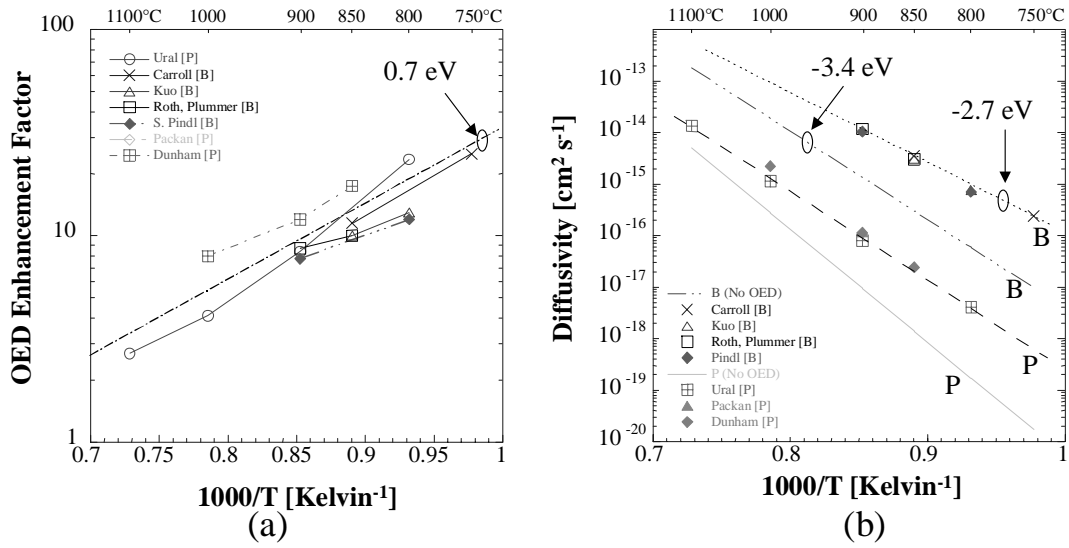


Figure 3.2 (a) diffusion enhancement ratios ($D_{ox} / D_{intrinsic}$) during oxidation for boron and phosphorus [7, 20, 31, 34-36], and (b) the boron and phosphorus diffusivities either during annealing in inert (intrinsic) or oxygen ambient [2, 7, 20, 31, 34-36].

interstitial defect is in the neighborhood of 3.7 eV [2, 11]. The binding energy of the silicon interstitial by the substitutional boron in the charge neutral state has been estimated to be 0.9 eV [2, 4, 12], which agrees relatively well with the experimentally determined activation energy of the total boron diffusivity of 0.6 eV, measured by electron paramagnetic resonance (EPR) [4] (Fig 3.3). However, the formation and binding energies of the silicon self-interstitial remains speculative [2, 12] and illustrates the lack of fundamental knowledge about the reaction mechanisms that lead to the boron diffusivity that still remain.

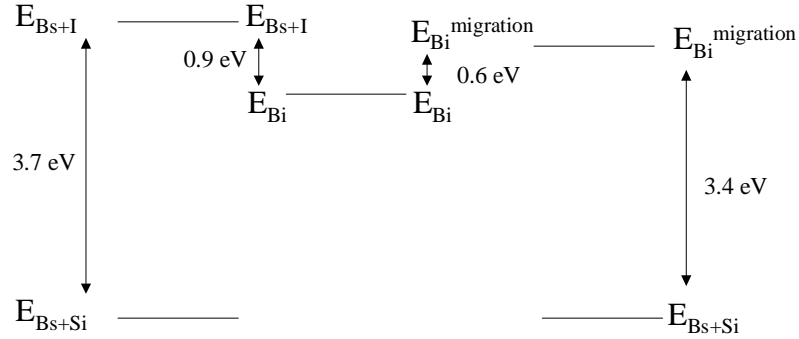


Figure 3.3 Energy level diagram for the dominant interstitial-boron species in boron diffusion. Note: neither the energy of formation for the free silicon interstitial or the binding energy of the silicon interstitial to the boron substitutional atom have been measured directly.

The reactions in equations 3.1 and 3.2 are assumed to occur rapidly relative to the diffusion time scale, which means that all species are in thermal equilibrium with one another at all times during diffusion:

$$B_i^{-1} = k_1 \cdot B_s^- \cdot I \quad (3.3)$$

$$B_i^0 = k_0 \cdot B_s^- \cdot I \cdot p \quad (3.4)$$

where $k_{0,1}$ are thermally activated equilibrium constants that describes the detailed balance between the species. The total flux of boron atoms must include the diffusive flux of both charged and neutral interstitial boron species and the drift flux of the charged mobile defect in an electric field (e.g. within the depletion region of a p-n junction). The combined flux of all species is, therefore [2, 3, 9, 13]:

$$J_B = \sum_{n=0,1} J_{B_i^{-n}} = \sum_{n=0,1} -\frac{\partial}{\partial x} (D_{B_i^{-n}} \cdot B_i^{-n}) - (nq) \cdot B_i^{-n} \cdot \frac{qD_{B_i^{-n}}}{k_B T} \cdot \vec{E} \quad (3.5)$$

where J_B is the total boron flux, B_i^{-n} is either the mobile boron defect in the neutral (n=0) or negatively charged state (n=1), $J_{B_i^{-n}}$ the flux of either the neutral or charged mobile boron defect, $D_{B_i^{-n}}$ is the diffusivity of one of the two species, n is the charge of the mobile defect, q is the charge of a single electron, k_B is the Boltzmann constant, T is the temperature and \vec{E} is the electric field. The last term of the flux describes the drift diffusion due to any built in fields from extrinsic doping conditions, which relies upon the Einstein relationship to express the mobility of the species as $\mu_{D_{B_i^{-n}}} = \frac{qD_{B_i^{-n}}}{k_B T}$.

Combining eq'n. 3.3, 3.4, and 3.5, the boron flux under intrinsic conditions can be rewritten as:

$$J_B^* = D_B^* \frac{\partial B_s}{\partial x} = \sum_{n=0,1} -D_{B_i^{-n}} \cdot \frac{\partial}{\partial x} B_i^{-n} = -(D_{B_i^{-1}} k_1 I^* + D_{B_i^0} k_0 p^* I^*) \cdot \frac{\partial B_s}{\partial x} \quad (3.6)$$

where the total boron flux in intrinsic silicon, J_B^* , from the mobile boron defect species is equated to Fick's 1st law of diffusion for the substitutional boron concentration, and D_B^* is the experimentally observed intrinsic boron diffusivity. The remaining variables are, I^* , the intrinsic interstitial concentration, and p^* the intrinsic free car-

rier concentration more frequently designated as n_i (p^* is used to avoid confusion in the notation). The observed diffusivity of the substitutional boron, D_B^* , can be equated to the mobile defect diffusivities, the equilibrium constants, and the intrinsic interstitial concentration from inspection of eq'n. 3.6,

$$D_B^* = D_{B_i^{-1}} k_1 I^* + D_{B_i^0} k_0 p^* I^* \quad (3.7).$$

The expression for the intrinsic boron diffusivity highlights its linear dependence on the silicon interstitial concentration. In cases when the interstitial concentration is perturbed from its intrinsic value the observed diffusivity increases proportionally to the relative interstitial concentration:

$$D_B = \frac{I}{I^*} \cdot D_{B_s}^* \quad (3.8)$$

where I is the local interstitial concentration. The relationship between the relative interstitial concentration and the observed extrinsic diffusivity is somewhat different. Starting from eq'n. 3.6 and assuming that there is no spatial gradient in the interstitial concentration the boron flux may be expressed as:

$$J_B = \sum_{n=0,1} -D_B^{-n} \times \frac{I}{I^*} \times \left(\frac{\partial}{\partial x} B_s^- + (nq) \cdot B_s^- \cdot \frac{q}{k_B T} \cdot \vec{E} \right) \quad (3.9)$$

where,

$$D_B^0 = D_{B_i^0} k_0 p I^* = D_{B_s}^0 \cdot \frac{p}{p^*} \quad (3.10)$$

$$D_B^{-1} = D_{B_i^{-1}} k_1 I^* = D_{B_s}^{-1} \quad (3.11)$$

$D_{B_s}^0$ and $D_{B_s}^{-1}$ are the observed substitutional boron diffusivities in the negatively charged and neutral states. All other variables are as previously defined [2, 3, 13]. This relationship is widely used in the extrinsic case to measure the local relative interstitial concentration by comparing the observed diffusivity to the extrinsic diffusivity expected with no excess interstitials. The extrinsic diffusivity is calculated using the local hole concentration and the literature values for $D_{B_s}^0$ and $D_{B_s}^{-1}$. Determination of the relative interstitial concentration from a boron profile is complicated by the concentration dependent diffusivity. The relative interstitial concentration, therefore, is usually found by numerically fitting an experimentally obtained boron profile to simulated profiles with a constant extrinsic diffusivity multiplied by a single fitting variable, i.e. the relative interstitial concentration. It should be noted that the validity of eq'n 3.9 relies on an assumption that the diffusivity of the mobile defect and the interstitial concentrations are spatially uniform. If either of these vary spatially, there will be additional contributions to the flux. Except where otherwise noted, it is assumed in this work that the additional boron flux due to interstitial or diffusivity gradients is negligible.

3.2.2 Oxidation enhanced diffusion

Certain silicon fabrication steps result in an increase in the interstitial concentration above the intrinsic concentration. Increases of silicon interstitials in the silicon lattice have been identified, for example, by the growth of stacking faults or dislocation loops below the silicon surface after oxidation [14, 15], which grow by the addition of extra silicon atoms. Presumably, because of the large mismatch in molecular volume of silicon dioxide and silicon, silicon interstitials are formed at the interface to relieve the stresses created by the oxidation reaction [16-18]. The silicon interstitials created at the surface consequently migrate to the stacking faults where they are trapped and contribute to the growth of the extended defect.

Boron diffusion is also known to increase during oxidation and the oxidation enhanced boron diffusion (OED) is attributed to the interaction between the substitutional boron and the excess interstitials injected during oxidation. In typical OED experiments it is found that the boron diffusivity is relatively uniform under the oxidized surface (Fig. 3.4), which is attributed to the relatively uniform interstitial concentrations due to long diffusion lengths of the silicon interstitial compared to the boron diffusion length for the same anneal conditions [2, 19]. Boron and phosphorus OED have been examined extensively over a wide range of temperatures (Fig. 3.2 (a)), and the similar diffusivity enhancements are because phosphorus and boron both diffuse primarily by an interstitial mechanism [6, 7].

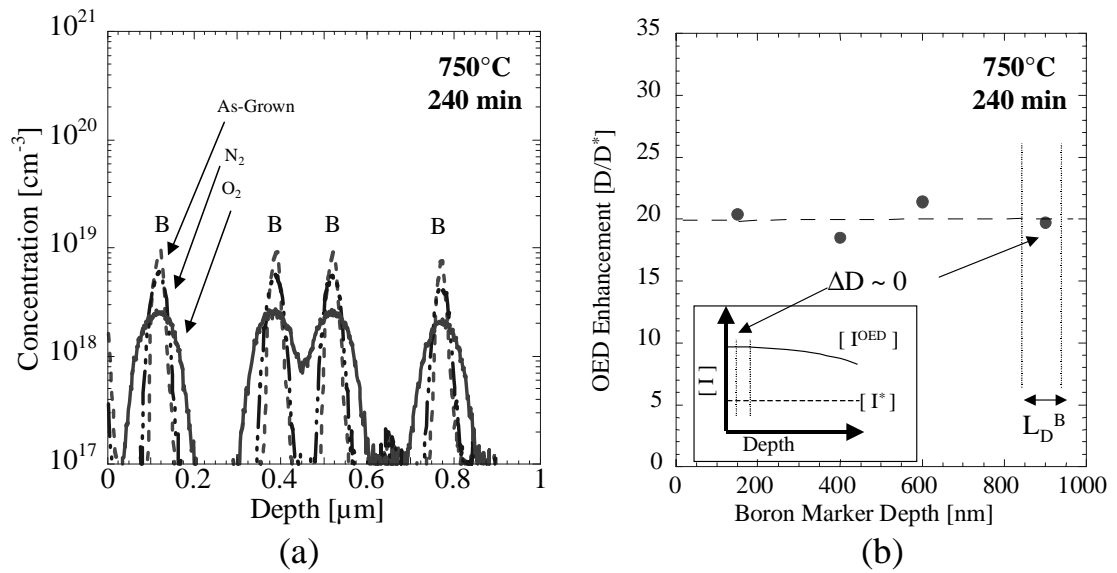


Figure 3.4 (a) boron concentration profiles in pure silicon before and after annealing at 750°C for 240 minutes in either nitrogen or oxygen ambient and (b) the depth dependence of the diffusivity enhancement during oxidation. A schematic inset is included to indicate the relative depth of decay of the interstitial profile (~ tens of microns) versus the diffusion length of the boron profiles examined in the near surface (top 1 micron).

Because of the technological demand for smaller device structures, it is increasingly important to be able to reduce the boron diffusion length for any given transistor fabrication process. This has traditionally been done by reducing the time and temperature of all thermal treatments in the fabrication process, i.e. using a smaller “thermal budget”. However, efforts to shrink the total boron diffusion length in the presence of an oxidation step are frustrated by the exponential increase in boron OED as the temperature is lowered, Fig. 3.2 (a). Clearly, a much lower temperature is required to achieve the same total diffusion lengths, when OED effects are present,

because of the smaller effective activation energy of the oxidation enhanced boron diffusivity, Fig. 3.2 (b). The primary point is that the boron diffusivity is sensitive to excess interstitials introduced by fabrication steps and that at lower temperatures the extra interstitials become the dominant source of boron diffusion. To further complicate matters, the absolute interstitial concentrations and diffusivity are notoriously difficult to directly measure and remain experimental unknowns [11]. Therefore, despite extensive research on silicon oxidation, a detailed quantitative understanding of the microscopic interstitial defect injection and formation physics does not exist [20].

3.2.3 Transient enhanced diffusion

As was discussed in the previous section, boron and phosphorus diffusion is enhanced during oxidation due to excess interstitials produced from the chemical reaction at the surface. Another important example of enhanced boron diffusion due to processing is transient enhanced diffusion (TED), which is the enhanced diffusion observed immediately after implantation of dopants. As is easy to imagine, the implantation process is very destructive to the silicon crystal lattice and therefore produces numerous point defects. After implantation it is necessary to anneal to recrystallize any silicon driven amorphous and electrically activate the implanted dopants. Boron diffusivities immediately after implantation have been reported to be thousands of times greater than the intrinsic diffusivities [21], due to the excess interstitial population created by the implantation. Furthermore, unimplanted dopants near implanted regions also experi-

ence similarly enhanced diffusivities, because the point defects created by the implant rapidly migrate to all nearby regions [21].

Because the enhanced diffusion from extra interstitials caused by processing dominate diffusion at lower temperatures, common steps like ion implantation (TED) and oxidation (OED) are recognized as significant challenges to the increased performance (scaling) of sub-micron devices [22]. In the next section the importance of controlling boron diffusion and reducing TED effects will be considered in the specific example of the SiGe HBT.

3.3 Boron diffusion in SiGeC

3.3.1 Introduction of C_s to reduce boron diffusion

In n-Si/p⁺SiGeC/n-Si HBTs, as boron diffuses from the p⁺SiGeC base into n-Si emitter and collector (Fig. 3.5), parasitic barriers are formed in the conduction band, which impede the flow of electrons from the emitter to collector [23, 24] (Fig. 3.6 (a)). The parasitic barrier that arises due to boron outdiffusion is strongly dependent on the boron concentration that diffuses into the silicon, and small amounts of boron outdiffusion $L_d \sim 10 \text{ \AA}$ can already cause large parasitic barriers evident in HBT's [24] because the collector current is exponentially dependent on the barrier height, schematically shown in Fig. 3.6 (b). This can be observed by directly measuring collector saturation current, or even more sensitively by observing the effect of collector-emitter bias on collector current (the Early effect). The Early voltage changes because the

barrier height, and hence the collector current, is affected by the collector-emitter bias [25].

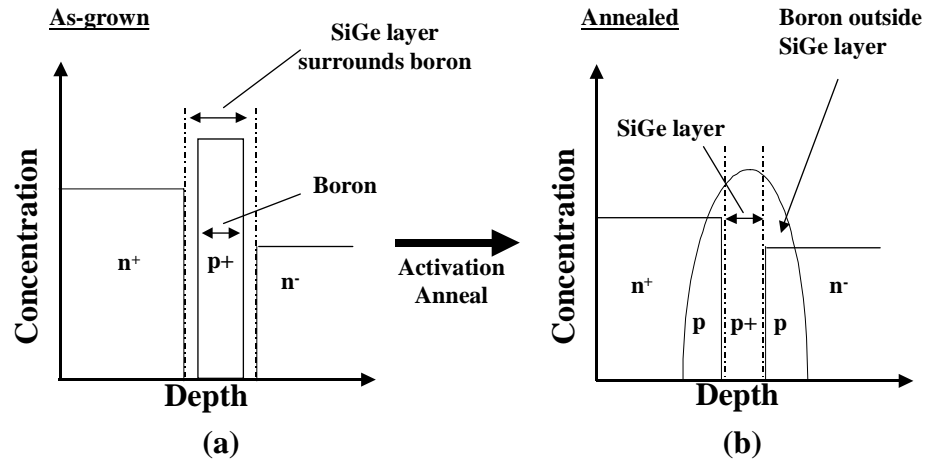


Figure 3.5. Schematic diagram of (a) the as-grown dopant profiles of a SiGe HBT structure and (b) the profile after annealing. Boron is shown to diffuse faster than the surrounding germanium (SiGe) layer forming a p-type region in the phosphorus doped silicon region.

Recently, the suppression of boron diffusion of both thermal and transient enhanced diffusion (TED) has been demonstrated through the incorporation of substitutional carbon in pure silicon and SiGe increasing the thermal budgets of the fabrication processes significantly [23, 26-28]. Because HBTs are so sensitive to boron diffusion from the base on a scale less than that detectable by SIMS, the HBT is an ideal probe to examine the effect that substitutional carbon has on boron diffusion. Therefore, we use HBT electrical characteristics to quantitatively compare boron diffusion in SiGe to boron diffusion in SiGeC for annealing or implant and annealing

conditions. Because the devices are greatly affected by diffusion at levels too small to be detected by SIMS, we use modeling of combined process and device simulators (TMA TSUPREM4 and MEDICI) to relate observed electrical characteristics (collector saturation currents and Early voltages) of the HBT's to infer the changes in boron profile and hence the changes in boron diffusion coefficients.

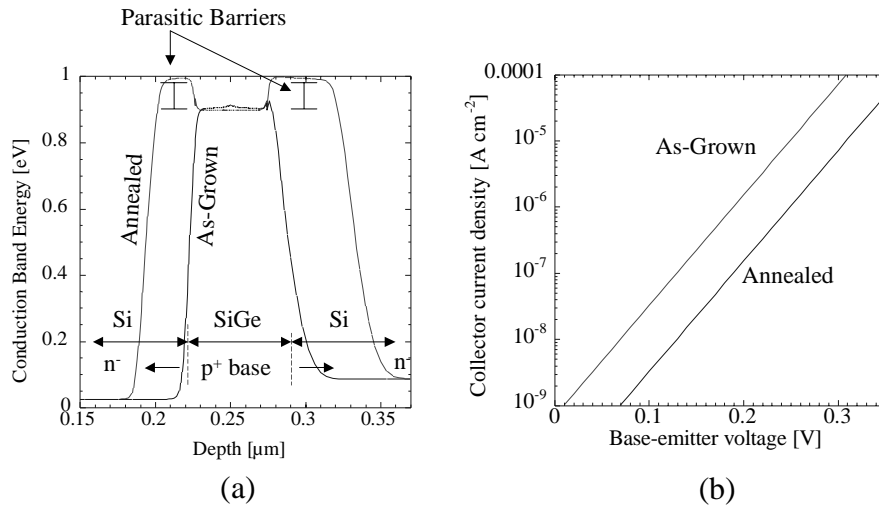


Figure 3.6 (a) schematic conduction band diagram of a (n-)Si/(p+)SiGeC/(n-)Si HBT as grown and after annealing showing the creation of a parasitic conduction band barrier as a result of boron diffusion from the base into the n-type Si emitter and collector region, and (b) the corresponding schematic reduction of collector current after annealing [24].

3.3.2 HBT Process Conditions

The HBT's were grown by RTCVD [29] at 575-700°C, with boron levels in the base of $\sim 10^{20} \text{ cm}^{-3}$ and bases of $\sim 20 \text{ nm}$ of $\text{Si}_{0.8}\text{Ge}_{0.2}$ or $\text{Si}_{0.795}\text{Ge}_{0.2}\text{C}_{0.005}$. The device fabrication was done using all low-temperature processing to avoid unnecessary diffusion and is described elsewhere [23, 26]. Photoluminescence and X-ray diffraction studies

on similar alloy layers show that the alloy layers are biaxially compressively strained to match the silicon lattice, and transmission electron microscopy (TEM) showed no dislocations, defects, or SiC precipitates in any of the as-grown layers [23, 26]. As-grown Gummel plots and common emitter characteristics of HBT's without and with 0.5% substitutional carbon in the bases are shown in Fig. 3.7 (a) and (b) respectively. High Early voltages and SIMS verifies that there is no significant boron outdiffusion [23, 26] in such HBT's fabricated without annealing.

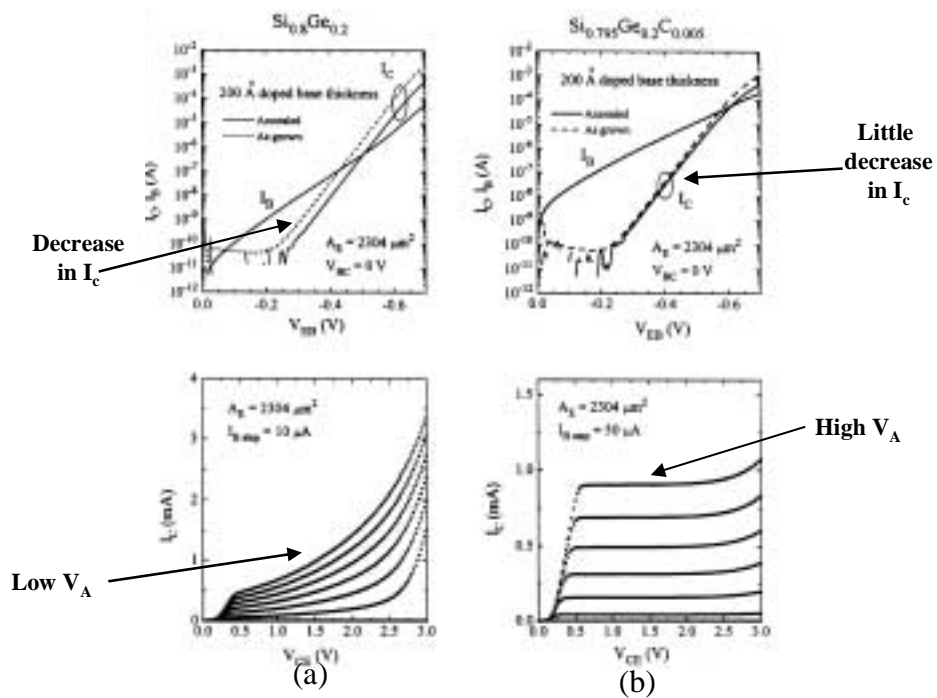


Figure 3.7 HBT Gummel plots and collector current vs. base-collector voltage after implant into 2000 Å Si n- emitter and 647°C anneal for HBT's with (a) SiGe or (b) SiGeC bases [23].

Two different cases are considered for HBT processing to study boron outdiffusion. Case (1): the effect that substitutional carbon has on the intrinsic boron diffusion rates (N_2 anneal, 15 minutes, 800-950°C); and case (2): The effect of substitutional carbon on the transient enhanced diffusion of boron due to ion implant damage in the overlying emitter layer ($1.5 \times 10^{15} \text{ cm}^{-2}$, As^+ , 30 keV and $3 \times 10^{14} \text{ cm}^{-2}$, As^+ , 15 keV into the silicon 2000 Å n^- emitter) with subsequent 15 minute activation anneals in N_2 at 647°C and 742°C. Note the range of the arsenic implant was at most 50 nm, so all damage occurs well above the base region.

SIMS, Gummel plots and common emitter characteristics of the processed HBT's with ion implant damage are shown in (Fig. 3.7). Saturation currents and Early voltages were then extracted from the electrical characteristics for comparison and fitting to simulated electrical characteristics. The decrease in I_c and reduced Early voltages in the transistors annealed at 647°C without carbon, Fig. 3.7 (a), show that boron has outdiffused significantly during this step even though this annealing condition is far less than the emitter thermal budget (i.e. the thermal budget required to grow the emitter by RTCVD). However the high Early voltages in the HBT devices with carbon show that much of the TED effects have been suppressed. Even in this case the Early voltage is not as high as that of the as grown HBT, ~ 10.5 V, evidence that some slight TED effects still remain, despite no evidence of boron outdiffusion at 647°C in boron profiles obtained using SIMS. Figure 3.8 shows that boron outdiffusion is

readily apparent for As implantation and a 755°C, 15 min N₂ anneal in the transistor without carbon, but is substantially reduced in the transistor with carbon.

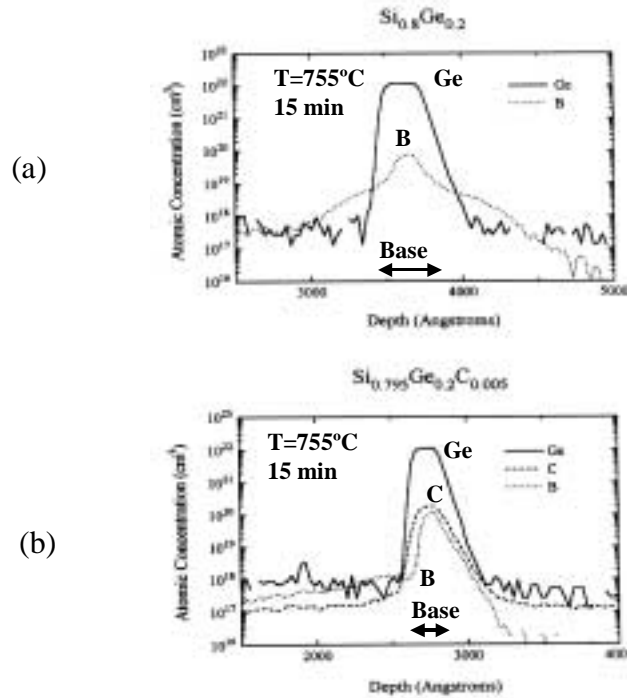


Figure 3.8 Boron, carbon and germanium profiles of the (a) SiGe and (b) SiGeC HBT's after implant into emitter and anneal at 755°C in N₂ for 15 minute [23, 26]. Note: no difference in boron concentration profiles of the implanted and 647°C annealed HBTs was observed from the SIMS profiles.

3.3.3 Extraction of diffusion constant (method)

Dopant profiles were modeled using TSUPREM4 (TMA), and the results were used in the device simulator MEDICI (TMA). The diffusion coefficient of boron in SiGeC (case 1) and excess interstitial concentration (case 2) were adjusted in TSUPREM4 so that the output of the device simulator matched the experimentally

measured Gummel plots and common-emitter characteristics. In case 1 a single effective diffusion constant, D_{eff} , for boron was used to fit electrical data for the entire device structure, maintaining the ratio of neutral and singly charged defect contributions to the diffusion constant and only varying the default magnitude by a constant. In case 2 (arsenic implant), the number of excess interstitials resulting from implant damage leading to enhanced boron diffusion was scaled to match the experimentally extracted electrical characteristics, while using a typical diffusion constant of boron in silicon at 647°C of $9.33 \times 10^{-10} \text{ um}^2 \text{ min}^{-1}$ corresponding to a boron diffusion length of approximately 1 Å after 15 minutes.

The HBT electrical characteristics were numerically simulated using the doping profiles obtained above to make comparison to experimental data. Bandgap differences of 160 meV and 147 meV were used for SiGe and SiGeC bases respectively.

The effective density of states in the $\text{Si}_{1-x}\text{Ge}_x$ base, approximately $\frac{N_C N_V^{\text{SiGe}}}{N_C N_V^{\text{Si}}} \cong 0.33$

for $x=0.2$, is assumed not to change in the SiGeC base; and a bandgap narrowing model commensurate with observed bandgap narrowing in SiGe due to high doping densities in SiGe [30], which is less than that observed in Si, was also included.

3.3.4 Boron diffusivity found in SiGe and SiGeC HBT bases

Collector saturation currents (y axis intercept) extracted from gummel plots (collector current vs. base emitter voltage) of fabricated HBT's for case 1, intrinsic diffusion, are

shown in Fig. 3.9. Typical boron diffusion lengths in silicon at 855°C for 15 minutes are $\sim 75 \text{ \AA}$ [2]. The saturation current of the Si/SiGe HBT's annealed at 855°C is already reduced nearly two orders of magnitude demonstrating the extreme HBT sensitivity to small boron diffusion lengths. For HBT processing this sensitivity is undesirable because it limits the total thermal budget available to the process engineer. Through the addition of substitutional carbon the onset of saturation current degradation can be shifted to higher temperatures increasing the available thermal budget, in this case, by as much as $\sim 100^\circ\text{C}$.

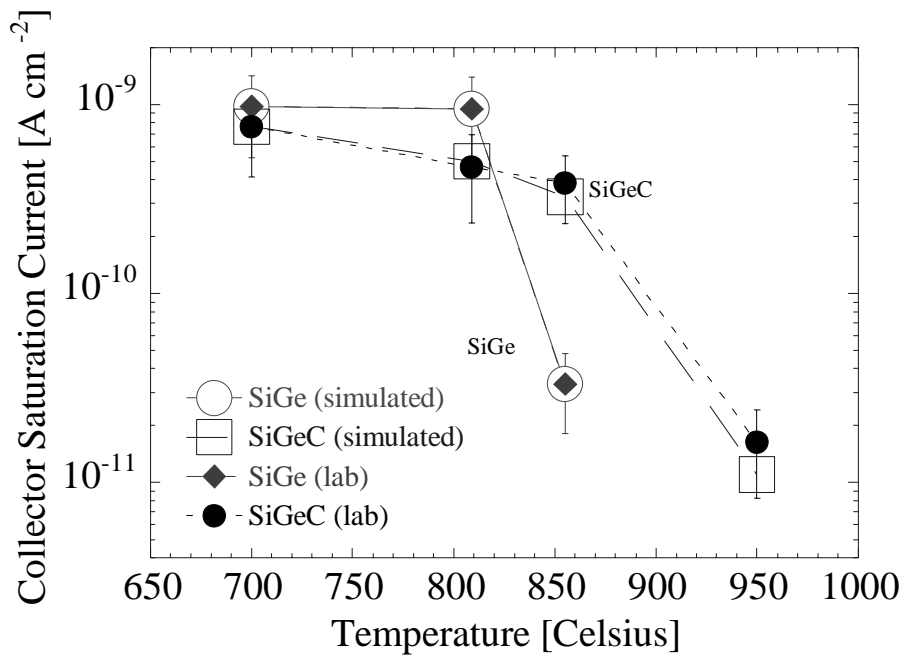


Figure 3.9 HBT saturation currents extracted from Gummel plots of fabricated and numerically simulated devices. Fabricated devices are indicated by solid markers, numerically simulated by hollow markers. Note carbon incorporation increases thermal budget of HBT process $\sim 100^\circ\text{C}$.

To quantitatively estimate the relative boron diffusion constants in SiGe and SiGeC, the experimentally observed collector saturation currents were numerically calculated and fit to the observed data by varying a single diffusion parameter, the relative interstitial concentration, as described above (eq'n. 3.11). The numerically obtained diffusion constants for boron in the SiGe and SiGeC are compared with the activation energy of boron diffusion in silicon [2] in Fig. 3.10. The fitted boron diffusivities in SiGeC are uniformly slower than those in Si and SiGe. The best fits yield boron diffusivities in SiGeC that are ~8 times less than that in SiGe and appear to have a similar activation energy as that of pure silicon, showing that the incorporation of carbon does not significantly change the energetics of boron diffusion compared to silicon. This also agrees with previously reported boron diffusivities in SiGe and SiGeC that find boron to move slower in SiGeC than in SiGe and both diffusivities to be slower than that in silicon [31-33], but the absolute diffusivities extracted from the HBT data are approximately 2-4 times faster than those reported. Various sources of error can contribute to disagreement with the referenced values. The numerically calculated profiles are simulated with a single diffusion constant for boron. The extracted diffusivity will represent an average diffusivity of that in the alloy layer and that in silicon. For long diffusion lengths, with respect to the width of the HBT base, the numerically found boron diffusivity in the alloy should be faster than that of the actual

boron diffusivities in the alloy. Other sources of the disagreement between the reported values and ours can come from errors in temperature calibration or not compensating for interface diffusion effects like the built in electric field. The combined effects can easily lead to factors of two in diffusivity.

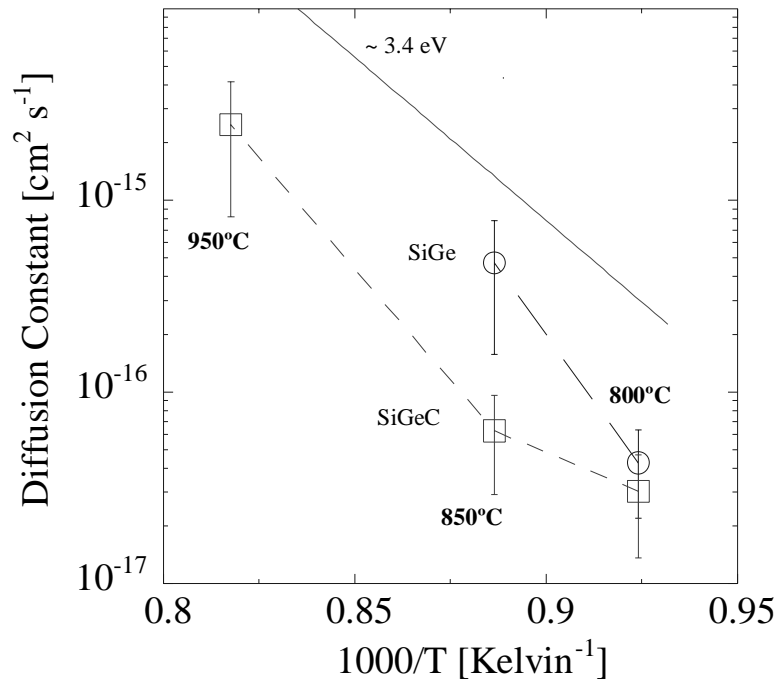


Figure 3.10 Boron diffusion constants obtained from fitted collector saturation currents in figure 3.8. Note boron diffusivity in SiGeC ~8 times less than that in SiGe. Reference line shows activation energy of 3.4 eV.

To illustrate the HBT sensitivity to boron diffusion, the extracted diffusion constant for boron in the 855°C annealed SiGeC device can be used to calculate an approximate boron diffusion length of ~25 Å [1]. This diffusion length is discernibly signaled by a one-half drop in collector saturation current compared to that of the as-

grown HBT. However, such a small diffusion length would be nearly impossible to resolve by SIMS since broadening of the boron profile in SIMS can be of the order of 20-40 Å [31]. Thus HBT electrical characteristics are more sensitive than SIMS to small diffusion lengths of boron. This highlights the necessity of minimal boron diffusion to maintain optimum performance of the SiGe HBT.

For case 2 (ion implant damage in overlying emitter layer), Early voltages were extracted from both fabricated devices, Fig. 3.11, and calculated using numerical simulations of the arsenic implant and anneal at 647°C. Excess interstitials due to ion implant damage lead to TED of boron and degrade device performance. The total excess interstitial concentrations were adjusted as the single parameter to fit the observed Early voltages of the devices. The unadjusted model estimates the excess interstitial concentration from implant damage to be $\sim 1.31 \times 10^{14} \text{ cm}^{-2}$ for an implant of 30 keV, $1.5 \times 10^{15} \text{ cm}^{-2} \text{ As}^+$ followed by 15 keV, $3 \times 10^{14} \text{ cm}^{-2} \text{ As}^+$. The resulting diffusion causes a predicted Early voltage of 0.3 V agreeing well with experiment for the SiGe case. In the case of a SiGeC base, the calculated Early voltage could only be made to agree with the observed device Early voltage after a reduction of over 99% of the excess interstitials [1]. This corresponds to a diffusion length of only a few Ångstroms, again showing the sensitivity of the device to minute amounts of boron diffusion, while no difference in SIMS profiles in that case could be seen.

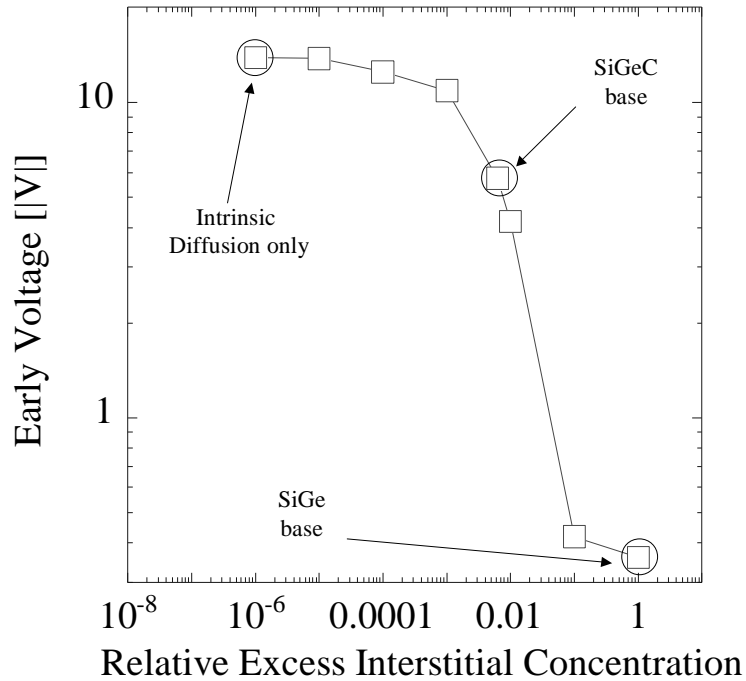


Figure 3.11 Calculated Early voltages for adjusted excess interstitials due to implant damage. Experimentally observed Early voltages obtained from HBT common-emitter electrical characteristics for asgrown HBTs with SiGeC bases, and implant and annealed HBTs with SiGe and SiGeC bases are indicated by circles.

It can be concluded that the SiGe(C) HBT is extremely sensitive to boron diffusion lengths as small as 10 \AA . Furthermore, the introduction of substitutional carbon clearly reduces boron diffusion and thereby increases the thermal budget for the fabrication of SiGe HBT. The intrinsic boron diffusivity in $\text{Si}_{0.795}\text{Ge}_{0.2}\text{C}_{0.005}$ is estimated to be 8 times less in $\text{Si}_{0.8}\text{Ge}_{0.2}$ and the substitutional carbon has been shown to sink approximately 99% of the interstitials that reach the SiGeC layer from the ion implant damage.

3.4 Summary

The microscopic mechanisms of solid-state boron diffusion in silicon were examined and boron diffusivity was shown to be linearly dependent on the silicon interstitial concentration. Because current transistor dimensions require extreme control over the boron profiles, common fabrication steps that produce extra silicon interstitials in the silicon lattice, e.g. ion implantation and oxidation, represent significant challenges to fabricating high performance transistors. Specifically, even in the case of ultra small thermal budgets (647°C, 15 minutes, $L_D \sim 1 \text{ \AA}$) boron TED still leads to noticeable decreases in the SiGe HBT's Early voltage and saturation currents, demonstrating the extreme sensitivity of the transistor to excess interstitials. The introduction of 0.5% substitutional carbon to the SiGe base is shown to reduce the effective intrinsic boron diffusivity by as much as a factor of 8 and sinks almost all excess interstitials that reach the SiGeC layer for this process. The success of substitutional carbon in reducing the boron diffusivity when introduced to the base of SiGe motivates the following chapters on determining what mechanism is responsible for the reduced boron diffusion when carbon is present. Some outstanding questions remaining to be answered are:

- (1) Why does the carbon reduce the boron diffusivity?
- (2) Is the lower diffusivity observed in SiGe vs. that in Si due to the same mechanism?

- (3) Does the carbon react with the boron directly?
- (4) Does the carbon react with the interstitials directly?
- (5) How much carbon is needed, i.e. what is the carbon concentration dependence?
- (6) Do carbon related defects form?

These critical questions are addressed in the following chapters.

3.5 References

- [1] M. S. Carroll, L. D. Lanzerotti, and J. C. Sturm, "Quantitative measurement of reduction of boron diffusion by substitutional carbon incorporation," presented at Diffusion Mechanisms in Crystalline Materials, San Francisco, 1998.
- [2] Fahey, P. B. Griffin, and J. D. Plummer, *Rev. Mod. Phys.* , vol. 61, pp. 289, 1989.
- [3] M. R. Pinto, D. M. Boulin, C. S. Rafferty, R. K. Smith, W. M. Coughran, I. C. Kizilyalli, and M. J. Thoma, *Tech. Digest IEDM* , pp. 923, 1992.
- [4] G. D. Watkins, *Phys. Rev. B* , vol. 12, pp. 5824, 1975.
- [5] R. D. Harris, J. L. Newton, and G. D. Watkins, "Negative-U defect: Interstitial boron in silicon," *Phys. Rev. B* , vol. 36, pp. 1094, 1987.
- [6] H.-J. Gossmann, T. E. Haynes, P. A. Stolk, D. C. Jacobson, G. H. Gilmer, J. M. Poate, H. S. Luftman, T. K. Mogi, and M. O. Thompson, *Appl. Phys. Lett.* , vol. 71, pp. 3862, 1997.
- [7] A. Ural, P. B. Griffin, and J. D. Plummer, "Fractional contributions of microscopic diffusion mechanisms for common dopants and self-diffusion in silicon," *J. Appl. Phys.* , vol. 85, pp. 6440, 1999.
- [8] R. B. Fair and P. N. Pappas, *J. Electrochem. Soc.* , vol. 122, pp. 1241, 1975.
- [9] R. F. Lever, J. M. Bonar, and A. F. W. Willoughby, *J. Appl. Phys.* , vol. 83, pp. 1988, 1998.
- [10] T. Y. Tan and U. Goesele, *Appl. Phys. A* , vol. 37, pp. 1, 1985.
- [11] H. Bracht, *MRS Bulletin* , vol. 25, pp. 22, 2000.
- [12] W. Windl, M. M. Bunea, R. Stumpf, S. T. Dunham, and M. P. Masquelier, *Phys. Rev. Lett.* , vol. 83, pp. 4345, 1999.
- [13] M. E. Law, C. S. Rafferty, and R. W. Dutton, "SUPREM IV User's Manual," . Stanford, CA: Stanford University, 1988.
- [14] Muraka, *J. Appl. Phys.* , vol. 48, pp. 5020, 1977.
- [15] D. Tsoukalas, D. Skarlatos, and J. Stoemenos, *J. Appl. Phys.* , vol. 87, pp. 8380, 2000.
- [16] S. T. Dunham and J. D. Plummer, "Point-Defect Generation during Oxidation of Silicon in Dry Oxygen Part 1: Theory," *J. Appl. Phys.* , vol. 59, pp. 2541, 1986.
- [17] G. Charitat and A. Martinez, *J. Appl. Phys.* , vol. 55, pp. 909, 1984.
- [18] W. Tiller, *J. Electrochem. Soc.* , vol. 127, pp. 625, 1980.
- [19] Y. Shibata, K. Taniguchi, and C. Hamaguchi, *J. Appl. Phys.* , vol. 70, 1991.
- [20] S. T. Dunham and J. D. Plummer, "Interactions of silicon point defects with SiO₂ films," *J. Appl. Phys.* , vol. 71, pp. 685, 1992.
- [21] P. A. Stolk, H.-J. Gossmann, D. J. Eaglesham, D. C. Jacobson, C. S. Rafferty, G. H. Gilmer, M. Jaraiz, J. M. Poate, H. S. Luftmann, and T. E. Haynes, "Physical

- mechanisms of transient enhanced dopant diffusion in ion-implanted silicon,” *J. Appl. Phys.* , vol. 81, pp. 6031, 1997.
- [22] P. Packan, *MRS Bulletin* , vol. 25, pp. 18, 2000.
- [23] L. D. Lanzerotti, J. C. Sturm, E. Stach, R. Hull, T. Buyuklimanli, and C. Magee, *Appl. Phys. Lett.* , vol. 70, pp. 23, 1997.
- [24] E. J. Prinz, P. M. Garone, P. V. Schwartz, X. Xiao, and J. C. Sturm, *IEEE Elec. Dev. Lett.* , vol. 12, pp. 42, 1991.
- [25] E. J. Prinz and J. C. Sturm, “Current Gain-Early Voltage Products in Hetero-junction Bipolar Transistors with Nonuniform Base Bandgaps,” *IEEE Elect. Dev. Lett.* , vol. 12, pp. 661, 1991.
- [26] L. D. Lanzerotti, J. C. Sturm, E. Stach, R. Hull, T. Buyuklimanli, and C. Magee, *IEDM Tech. Digest* , pp. 249, 1996.
- [27] R. Scholz, U. Goesele, J. Y. Huh, and T. Y. Tan, *Appl. Phys. Lett.* , vol. 72, pp. 2, 1998.
- [28] H. J. Osten, G. Lippert, P. Gaworzewski, and R. Sorge, *Appl. Phys. Lett.* , vol. 71, pp. 11, 1997.
- [29] J. C. Sturm, H. Manoharan, L. Lenchyshyn, M. Thewalt, N. Rowell, J. P. Noel, and D. Houghton, *Phys. Rev. Lett.* , vol. 66, pp. 1362, 1991.
- [30] Z. Matutinovic-Krstelj, V. Venkataraman, E. J. Prinz, and J. C. Sturm, *IEEE Trans. Elec. Dev.* , vol. 43, 1996.
- [31] P. Kuo, J. L. Hoyt, Gibbons, Turner, Jacowitz, and T. Kamins, *Appl. Phys. Lett.* , vol. 62, 1993.
- [32] A. F. W. Willoughby, J. M. Bonar, and A. D. N. Paine, “Diffusion in SiGe Alloys,” presented at Si Front-End Processing-Physics and Technology of Dopant-Defect Interactions, San Fransisco, 1999.
- [33] N. Larsen, “Impurity Diffusion in SiGe Alloys: Strain and Composition Effects,” presented at Diffusion Mechanisms in Crystalline Materials, San Fransisco, 1998.
- [34] Roth and Plummer, *J. Electrochem. Soc.* , vol. 141, pp. 1074, 1994.
- [35] S. Pindl, M. Biebl, and E. Hammerl, *J. Electrochemical Soc.* , vol. 144, pp. 4022, 1997.
- [36] P. Packan and J. D. Plummer, *J. Appl. Phys.* , vol. 168, pp. 4327, 1990.

Substitutional Carbon as a Silicon Self-Interstitial Sink**4.1 Introduction**

In the previous chapter the importance of limiting boron diffusion during processing was highlighted by the SiGe HBT's electrical characteristics, which are sensitive to boron diffusion lengths as small as 1-2 nm. One novel approach to reduce boron diffusion, discussed in the previous chapter, is the introduction of substitutional carbon into the SiGe base region. The incorporation of 0.5% carbon was found to be enough to reduce the intrinsic base boron diffusivity by as much as a factor of 8 and to eliminate ~99% of the boron diffusivity enhancement from the excess interstitials created by ion implant damage.

Because of the possible technological advantages of substitutional carbon incorporation a deeper understanding of the point defect relationship with the substitutional carbon is desirable in order to predict critical variables like the necessary carbon concentrations required to eliminate OED and TED effects in a device structure. In this chapter, a direct reaction between substitutional carbon and the silicon self-interstitials is established. In the following chapters the carbon-self-interstitial reaction in SiGe is quantified.

4.2 Previous reports on reduced boron diffusivity in the presence of carbon

As discussed previously, it is generally accepted that boron diffuses primarily via an interstitial mechanism and that the boron diffusivity is linearly dependent on the silicon interstitial concentration. Ion implant damage and oxidation are sources of excess interstitials, which enhance the boron diffusivity, therefore the reduction of TED and OED depend on the effective ability to trap or annihilate any excess interstitials that are produced during processing. The boron diffusivity has already been observed to strongly depend on the concentration of substitutional carbon in silicon [1-4]. Various approaches of carbon incorporation into silicon have been used to explore the carbon effect on enhanced boron diffusion including carbon-containing alloys (e.g. Si_xC_y [5] and $\text{Si}_{1-x-y}\text{Ge}_x\text{C}_y$ [1, 6]), uniform carbon doping of silicon [2], and localized carbon doping of silicon [7]. These approaches may be summarized in to two categories. First, silicon or carbon-silicon alloys that have a uniform distribution of carbon in them [5, 7]; and second, silicon with localized carbon doped regions or thin carbon containing alloy layers [6, 7]. Complete suppression of the TED and OED of boron has already been reported for the category of uniform carbon concentration [7]. However, for practical use in device applications this approach is hampered by concerns about the electrical activity of carbon-related defects in silicon [6, 8, 9].

Localized carbon doped regions, however, offer a potential solution to the difficulties presented by uniform carbon doping. Carbon containing regions may be placed away from the active region eliminating concerns about electrical defects, and

also creating a test structure with which to isolate carbon's effect on interstitial concentration without the complication of carbon or germanium's effects on the intrinsic boron diffusivity. However, no complete suppression of TED or OED was reported before this work with a localized carbon region. This work was reported in the following publications [10-12].

4.3 Interstitial filter experiment using SiGeC

The test structures were grown using rapid thermal chemical vapor deposition (RTCVD) [13], between 600 and 750°C using methylsilane as the carbon source. A phosphorus layer at the surface and two boron doped silicon layers with or without a $\text{Si}_{1-x-y}\text{Ge}_x\text{C}_y$ or $\text{Si}_{1-x}\text{Ge}_x$ layer placed between the boron-doped layers were grown above a boron doped buffer layer $\sim 1 \mu\text{m}$ thick. The structure is used to test the effect of the $\text{Si}_{1-x-y}\text{Ge}_x\text{C}_y$ layer on phosphorus and boron diffusivities at different locations (above and below) with respect to the SiGe(C) layer. The phosphorus layer concentration was $\sim 1 \times 10^{19} \text{ cm}^{-3}$ and approximately 1500 Å thick, and both boron peaks were approximately 250 Å thick and had a boron concentration of $\sim 5 \times 10^{19} \text{ cm}^{-3}$ centered 2000 Å and 3000 Å away from the surface respectively, while the 250 Å thick SiGe(C) layer was centered 2300 Å from the surface (Fig. 4.1).

I Intersitials & oxide forms during oxidation		
↓	Si : phosphorus $1 \times 10^{19}/\text{cm}^{-3}$	600 Å
↓	i-Si	2000 Å
I ↓	Si : boron $3 \times 10^{19}/\text{cm}^{-3}$	250 Å
↓	i-Si	100 Å
↓	i-Si_{1-x-y}Ge_xC_y	250 Å
↓	i-Si	400 Å
	Si : boron $3 \times 10^{19}/\text{cm}^{-3}$	250 Å
	i-Si	1000 Å
	Si buffer layer: boron $3 \times 10^{19}/\text{cm}^{-3}$	

Figure 4.1 Test structure to study boron or phosphorus oxidation enhanced diffusion and transient enhanced diffusion. Two boron markers are separated by a $\text{Si}_{1-x-y}\text{Ge}_x\text{C}_y$ interstitial barrier layer ($x = [0 - 0.2]$; $y = [0 - 0.005]$)

To study boron OED dependence on substitutional carbon level

as-grown samples were cleaved and annealed in nitrogen and oxygen ambient atmospheres for 30 minutes at 897°C. For this experiment, the temperature measured by the thermocouple in the annealing furnace are suspect because of poor alignment. The thermocouple was located improperly close to the cold-zone and therefore indicated an inaccurately low temperature. The temperature of the sample was determined, alternatively, by calculating the boron diffusivity from the annealing time and the mea-

sured boron diffusion length (using SIMS) in the pure silicon sample. The temperature of the sample was then deduced by comparing the well established temperature dependence of the boron diffusivity in silicon [14] to the measured boron diffusivity in the silicon sample. The deduced temperature also agrees with the resulting oxide thickness and amount of oxidation enhanced diffusion observed for these samples. Boron profiles were characterized using secondary ion mass spectroscopy (SIMS) with 2 keV Cs^+ ions a 15-20% error in boron and phosphorus concentrations and an estimated 1-5% error in depth scales. Figure 4.2 shows profiles of the boron concentration in a pure silicon sample, i.e. no SiGe(C) layer, with a background carbon concentration below SIMS detection limits. Broadening of both boron peaks is observed after the nitrogen anneal, and in the oxidation case clear enhancement of the boron diffusion is observed by the further broadening of the boron profile. Further evidence of the OED is the significant boron diffusion from the buffer layer that has diffused over 100 nm and now interferes with the boron profile of the bottom most marker layer.

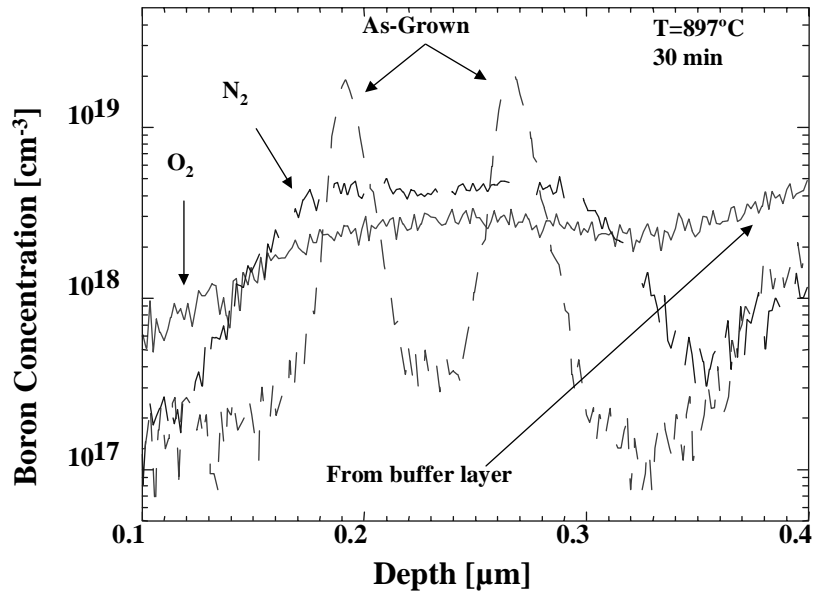


Figure 4.2 Boron concentration profiles (measured using SIMS) from samples of doped pure silicon (no intervening SiGeC layer) of as-grown and annealed for 897°C for 30 minutes in nitrogen ambient, or in oxygen ambient samples. Oxidation enhanced diffusion (OED) is demonstrated by the broader boron profile after anneal in oxygen ambient compared to that annealed in nitrogen.

To quantitatively compare the effect of different annealing conditions on the boron, boron diffusivities for each profile were obtained by fitting each concentration profile with the process simulator PROPHET [15] using a single variable fit (i.e. the ratio of excess self-interstitial to intrinsic self-interstitial concentrations I / I^*). In this case (Fig. 4.2), the boron diffusivity during oxidation is found to be 6 times that of the average boron diffusivity during the nitrogen anneal. Figure 4.3 shows boron profiles before and after anneals for the sample containing an intervening thin 250 Å

$\text{Si}_{0.795}\text{Ge}_{0.2}\text{C}_{0.005}$ layer between the boron markers. Two dashed lines are overlaid to indicate the location of the SiGeC layer. The same broadening is observed in the peak below the $\text{Si}_{1-x-y}\text{Ge}_x\text{C}_y$ layer after annealing in nitrogen, but in this case there is no additional broadening after oxidation, indicating that for this substitutional carbon level the oxidation-enhanced diffusion below the SiGeC has been completely suppressed. The excess interstitial concentration, therefore, has been reduced to zero below the carbon containing layer and shows that the $\text{Si}_{1-x-y}\text{Ge}_x\text{C}_y$ layer blocks interstitials from reaching the layer below completely suppressing boron OED.

We also conclude from this sample that the formation of an immobile complex like $\text{B}_i\text{-C}_s$ is not responsible for the “sinking” of the injected self-interstitials.

Although, in this case, some boron do migrate into the SiGeC layer and hypothetically might form immobile complexes trapping some self-interstitials this can not explain the “sinking” effect. Most interstitials pass through the top most boron layer, indicated by the similar enhanced diffusion in both boron peaks in the pure-silicon sample.

Since the B_i that form and migrate to the carbon layer in the carbon-containing sample represent only a small fraction of all the self-interstitials passing through the top boron marker layer, the subsequent hypothetical immobile $\text{B}_i\text{-C}_s$ cannot be responsible for trapping an appreciable number of the injected interstitials. Therefore, a $\text{B}_i\text{-C}_s$ complex can be ruled out as the primary interstitial trap.

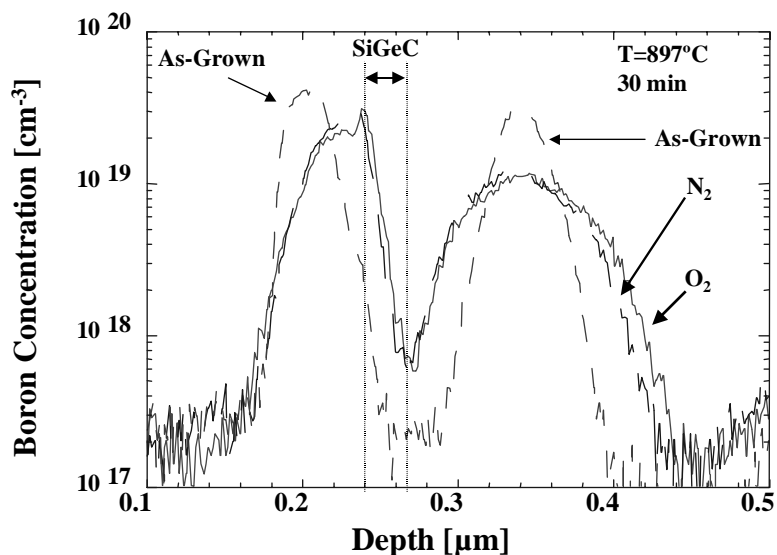


Figure 4.3 Boron concentration profiles from samples of doped silicon with the highest level of carbon in the SiGeC barrier layer of as-grown samples, and samples annealed for 897°C for 30 minutes in nitrogen ambient, or in oxygen ambient samples with. Boron OED is completely suppressed as indicated by no difference between boron profiles of the deepest marker after anneal in oxygen and anneal in nitrogen ambient.

The boron profiles of the boron marker above the $\text{Si}_{0.795}\text{Ge}_{0.2}\text{C}_{0.005}$ are also nearly identical after anneals in either oxygen or nitrogen, Fig. 4.3, indicating that the excess interstitial concentration must also be reduced to nearly zero even as far as 100-200 Å above the intervening $\text{Si}_{1-x-y}\text{Ge}_x\text{C}_y$ layer. The boron profile above the SiGeC layer after annealing is unusual because of the asymmetric broadening, spiked profile at the Si/SiGeC interface, and the overall peak shift towards the SiGeC layer. The

boron profile in the upper marker layer is not understood at this time but the behavior might be attributed to the combined effects of diffusion in an interstitial concentration gradient near the $\text{Si}_{1-x-y}\text{Ge}_x\text{C}_y$ layer (see next section and following chapter), diffusion into a $\text{Si}_{1-x-y}\text{Ge}_x\text{C}_y$ region of much slower boron diffusivity (previous chapter), and boron segregation into the $\text{Si}_{1-x-y}\text{Ge}_x\text{C}_y$ alloy layer (independent of the diffusivity differences). Boron segregation into strained $\text{Si}_{0.8}\text{Ge}_{0.2}$ from silicon in a ratio of 1.2 at 923°C with an activation energy of 0.3 eV has previously been reported, [16, 17] and further study is in progress to determine the boron segregation and diffusivity dependence on carbon content.

Samples with different substitutional carbon levels in the $\text{Si}_{1-x}\text{Ge}_x$ alloy layer were grown and annealed to test the OED carbon level dependence. Figure 4.4 summarizes the relative boron diffusivities of the boron peak under the $\text{Si}_{1-x-y}\text{Ge}_x\text{C}_y$ during anneals in oxygen versus nitrogen ambient, for carbon levels of 0 to 0.5%. To within experimental error there is no difference between the OED of boron in the cases of boron markers in pure silicon and that with an intervening $\text{Si}_{1-x}\text{Ge}_x$ alloy layer (no carbon) between the boron markers. This demonstrates that the interstitial trapping is not a result of the addition of the $\text{Si}_{1-x}\text{Ge}_x$ alloy layer and is in agreement with previous work [6, 18]. Finally, we observe a monotonic decrease in boron OED with increasing carbon level in the alloy layer indicating that as the carbon level is increased more interstitials from the surface region react with the carbon and fewer

interstitials pass through the layer, schematically represented in Fig. 4.5. The total carbon level required to completely suppress the OED for these conditions is bound between $4.56 \times 10^{13} \text{ cm}^{-2}$ and $5.57 \times 10^{14} \text{ cm}^{-2}$ integrated carbon level.

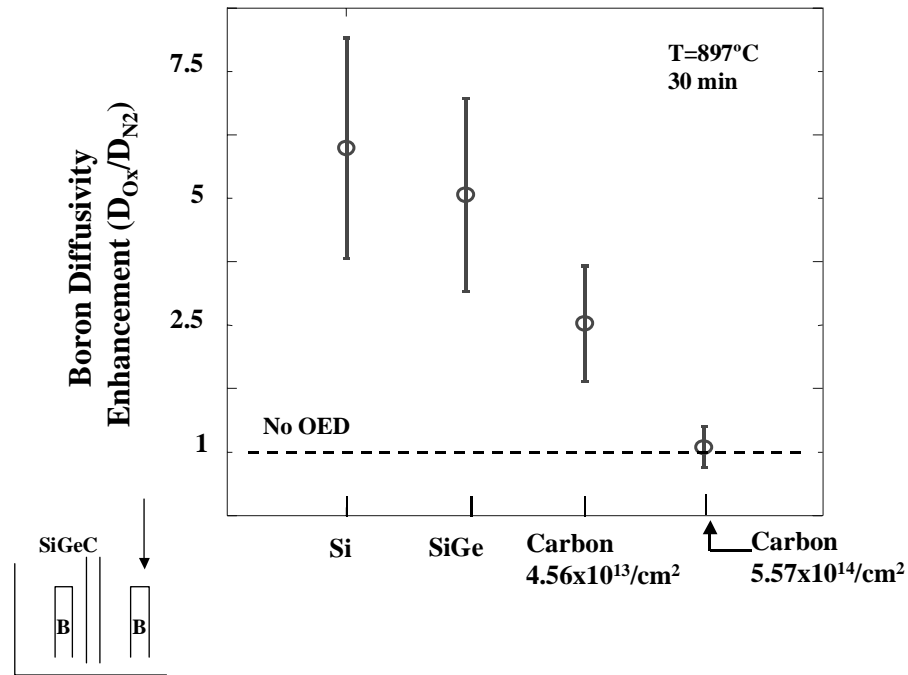


Figure 4.4 Average diffusivity (boron) enhancement's dependence on carbon levels in SiGe(C) barrier layer for oxidation 897°C for 30 min. Boron diffusivity of deepest marker is displayed relative to that of the average boron diffusivity during anneal in nitrogen ambient, 897°C for 30 min in nitrogen. The schematic diagram below the y-axis label is to indicate that these are the diffusivities of the bottom most boron marker layer.

The dependence of boron TED on substitutional carbon level as-grown samples (Fig. 4.1) with and without buried $\text{Si}_{1-x-y}\text{Ge}_x\text{C}_y$ layers were cleaved and subjected to implant levels of $5 \times 10^{13} \text{ cm}^{-2}$ and $5 \times 10^{14} \text{ cm}^{-2}$ silicon with an

implant energies of 30 keV, and then annealed in a nitrogen ambient for 15 minutes at 800°C. The depth of the silicon implanted profile is estimated to be 600 Å. Migration of interstitials from the ion implant damaged region lead to excess diffusion of the lower boron peak (as measured by SIMS), which decreases as the carbon level of the barrier layer is increased. At the highest carbon levels no significant difference in the lower boron profiles can be seen between samples with or without ion implant damage, again indicating complete filtering of the excess interstitials. Average boron diffusion constants were then extracted by fitting measured boron profiles to simulation. Figure 4.6 summarizes, for two different silicon implant doses and different carbon levels in the barrier level, the average boron diffusivity after ion implantation relative to the measured boron diffusivity without silicon ion implantation in the same samples. For both implant doses of $5 \times 10^{13} \text{ cm}^{-2}$ and $5 \times 10^{14} \text{ cm}^{-2}$ silicon the total carbon level required to completely suppress the TED for these conditions is bound between $4.56 \times 10^{13} \text{ cm}^{-2}$ and $5.57 \times 10^{14} \text{ cm}^{-2}$ carbon level.

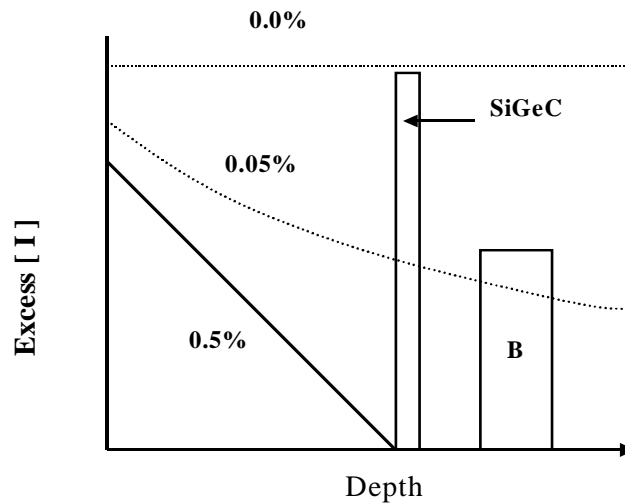


Figure 4.5 Schematic diagram of the interstitial concentration for three cases of carbon content in the buried SiGeC layer. As carbon level is increased, the interstitial concentration in both the surface region and below the SiGeC layer are reduced. The exact profile is yet to be determined.

For the case when the surface is not driven amorphous, implantation has been found to create a little over one excess interstitial for every implanted ion, which are known to condense into interstitial clusters for similar conditions [7]. An accurate estimate of the number of interstitials that are released and migrate to the carbon layer is not known at this time because detailed knowledge about the dynamics of how the interstitials are released and how many are annihilated at the nearby surface is not known. Note: the boron TED after implantation with the higher dose is only a little over three times as great as the lower dose although 10 times more silicon is implanted. In this case, the surface is driven amorphous and the number of excess

interstitials created by the implant no longer grows linearly with dose because the interstitials formed in the amorphous layer are annihilated during the subsequent solid-phase epitaxy.

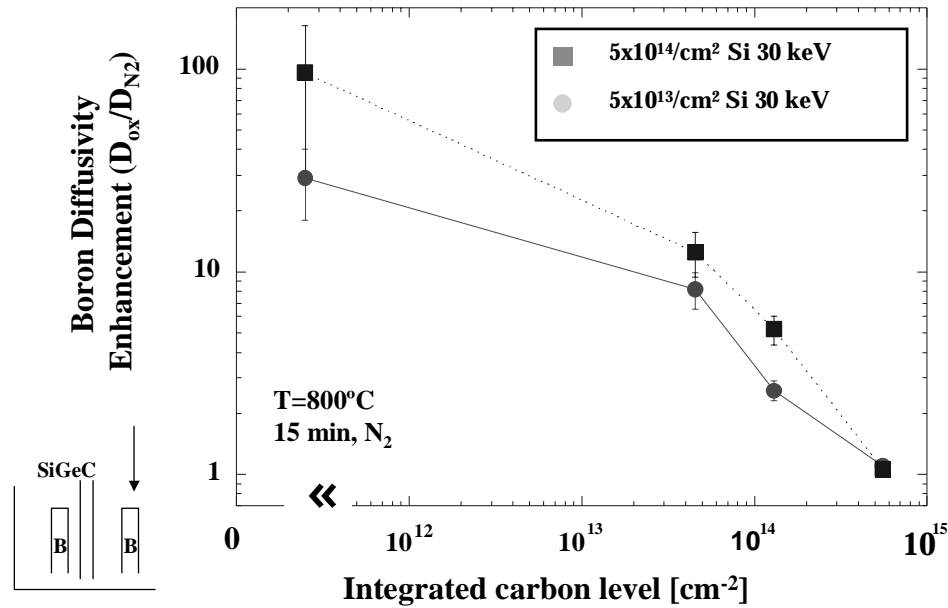


Figure 4.6 Average boron diffusivity (during 800°C 15 minute anneal after ion implantation for Si doses of $5 \times 10^{13}/\text{cm}^2$ or $5 \times 10^{14}/\text{cm}^2$ at 30 keV) dependence on carbon levels in SiGe(C) barrier layer. Boron diffusivities of deepest marker is displayed relative to that of the average boron diffusivity during an 800°C 15 minute anneal in nitrogen ambient atmosphere without ion implantation. The schematic diagram below the y-axis label is to indicate that these are the diffusivities of the bottom most boron marker layer.

4.3 Phosphorus diffusion above the SiGeC layer

Figure 4.7 shows profiles of the overlying phosphorus edge in the all-silicon control sample, with a background carbon concentration below SIMS detection limits. Broadening of the phosphorus edge is observed after the nitrogen anneal, and in the oxida-

tion case clear enhancement of the phosphorus diffusion is observed by the deeper location of the phosphorus. The phosphorus diffusivities for each case were obtained by fitting simulated diffused phosphorus profiles to experiment with PROPHET using a spatially constant phosphorus diffusivity. The measured diffusivity is, therefore, a spatial average of the actual diffusivity, which is not believed to be uniform above the SiGeC layer (Fig. 4.5). Because phosphorus is believed also to diffuse almost entirely by an interstitial mechanism [19], the enhanced phosphorus diffusivity is likewise a measure of the relative silicon interstitial enhancement,

$$\frac{D_P^{meas}}{D_P^*} \cong \frac{I}{I^*} \quad (4.1)$$

analogous to case of enhanced boron diffusion due to excess interstitial concentrations.

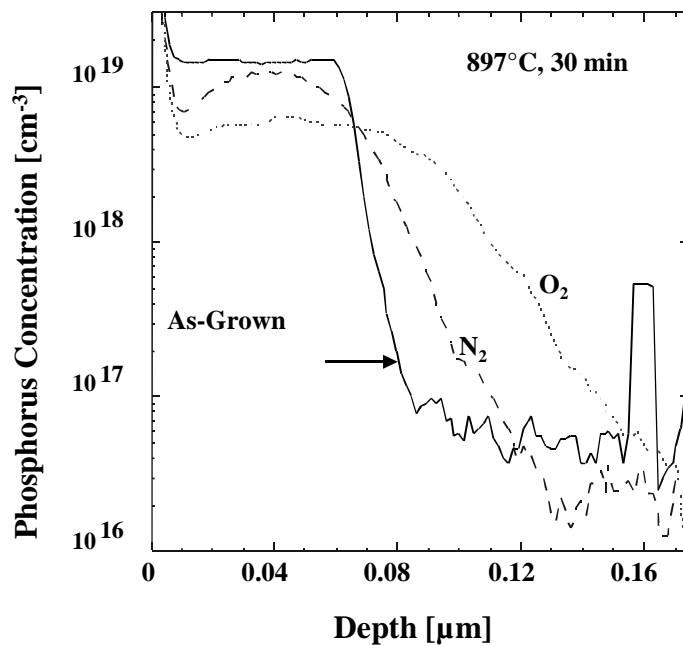


Figure 4.7 Phosphorus concentration profiles (measured using SIMS) of as-grown all-silicon sample and all-silicon annealed at 897°C for 30 minutes in nitrogen or oxygen ambient. Phosphorus OED is evident by the deeper phosphorus edge after oxidation.

The phosphorus diffusivity during oxidation is found to be 8 times that of the average phosphorus diffusivity during the nitrogen anneal in this case agreeing reasonably with previous reports (Fig 3.2). Note: the boron diffusivity was enhanced 6 times by oxidation in the same sample, which agrees with the phosphorus enhancement within the uncertainty of the measurement. In Fig. 4.8, the phosphorus profiles before and after oxidation in the all-silicon case is overlaid on that from the sample with a buried $\text{Si}_{0.795}\text{Ge}_{0.20}\text{C}_{0.005}$. The annealed carbon profile is overlaid on the phosphorus

profiles for reference. After oxidation the phosphorus edge in the silicon sample (dashed line) has clearly diffused deeper into the silicon layer than that in the sample with a buried SiGeC layer (solid line), despite the higher initial phosphorus concentration in the as-grown sample with the buried SiGeC layer (solid line). A four times

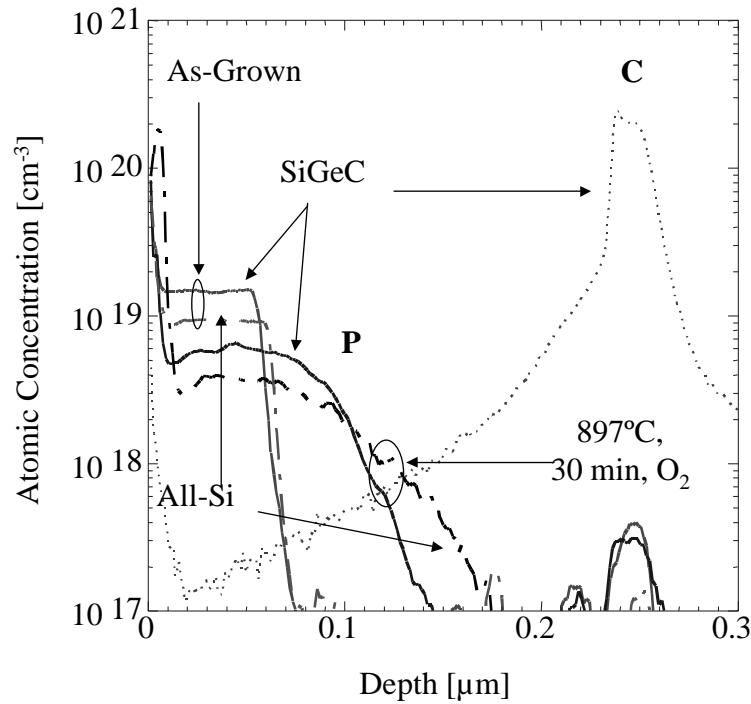


Figure 4.8 Phosphorus concentration profiles (measured using SIMS) before and after annealing the samples at 897°C for 30 minutes in oxygen ambient with (solid line) or without (dashed line) a buried SiGeC layer. The carbon concentration (dotted line) of the buried SiGeC layer after annealing is overlaid for reference.

reduction of phosphorus diffusivity is observed in the sample containing the buried SiGeC, even though the SiGeC layer is 1500-2000Å below the phosphorus moving edge. A summary of the measured diffusivities after oxidation relative to the mea-

sured diffusivities after the nitrogen anneal are shown in Fig. 4.9 for the silicon case and two carbon concentrations of 0.05% and 0.5%. The phosphorus OED above the SiGeC layer decreases with increasing carbon level as was observed for the boron marker layer below the SiGeC layer, Fig. 4.4 and 4.9. The interstitial concentration above and below the SiGeC layer clearly depends on the efficiency of the SiGeC layer to react with the injected interstitials and presumably the increased number of carbon react with an increased number of interstitials, which depletes the surface region of excess interstitials, explaining the reduced phosphorus OED above the SiGeC layer, Fig. 4.5. However, the exact interstitial profile can not be deduced from the phosphorus edge because for short times it samples only one point above the SiGeC layer and at longer times it is difficult to accurately model the diffusion with a single diffusivity since the interstitial concentration is presumably varying as a function of depth, as postulated in Fig. 4.5. The following chapter examines the interstitial concentration above the SiGeC layer in more detail.

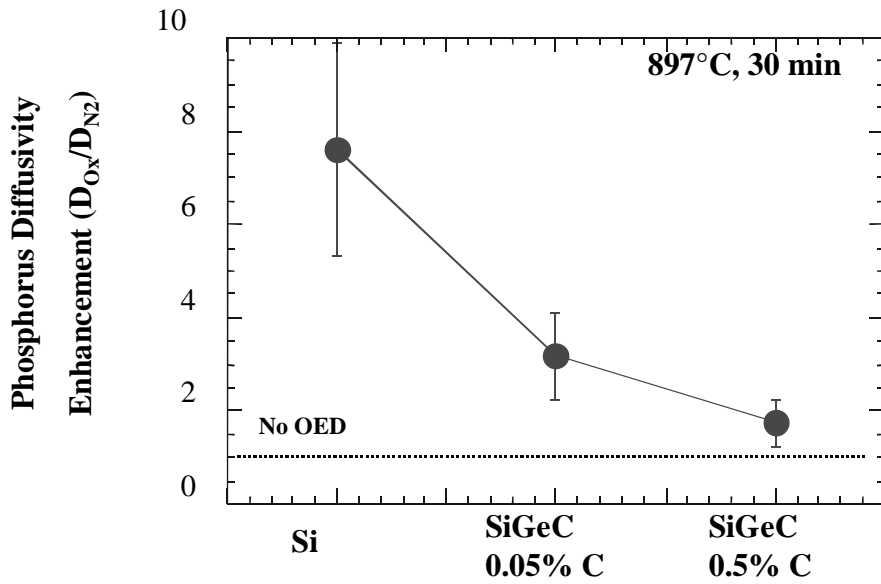
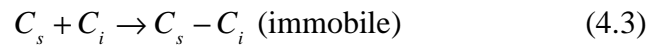
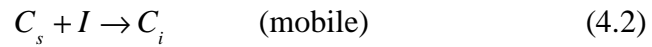


Figure 4.9 Relative phosphorus diffusivity dependence on carbon levels in buried Si(GeC) layers. Average diffusivities during annealing at 897°C for 30 minutes in oxygen ambient is compared to that after annealing in nitrogen.

4.4 Carbon profile after annealing

Because carbon in some defects states is electrically active, it is important to determine where the carbon is after processing. Furthermore, carbon is reported to diffuse quickly in silicon [9], making it difficult to contain in a confined region. The carbon diffusion after oxidation in samples with the highest initial carbon levels in the SiGeC layer (Fig. 4.10), have nearly the same concentrations as those after annealing in nitrogen for the same times. Diffusion of carbon at low concentrations in silicon, less than 10^{18} cm^{-3} , is usually described well by Fick's 2nd law [9]. However the

unusually non-gaussian out-diffusion of carbon showing long tails of low concentration carbon diffusing hundreds of nanometers surrounding by a nearly stationary high concentration carbon rich layer has led some researchers to invoke immobile clusters of C_s - C_i or silicon-carbide precipitation to explain both the interstitial sinking capacity of carbon as well as the unusual diffusion profiles [2, 20]. The formation of these two silicon-carbon species can remove silicon interstitials from the local population by trapping and immobilizing silicon interstitials as C_s - C_i clusters [9]



or annihilating interstitials through the formation of additional vacancies created by the silicon-carbide precipitation [21]. The entire carbon profile is described, therefore, as a large fraction of immobilized carbon clusters or precipitates surrounded by the out-diffusion of the much smaller concentration of unbound carbon that diffuse via the carbon's normal diffusion mechanism (e.g. eq'n. 4.2). It will be shown in the following chapters that a more simple reaction pathway sufficiently explains both the sink effect and the unusual carbon diffusion without invoking a cluster/precipitation reaction.

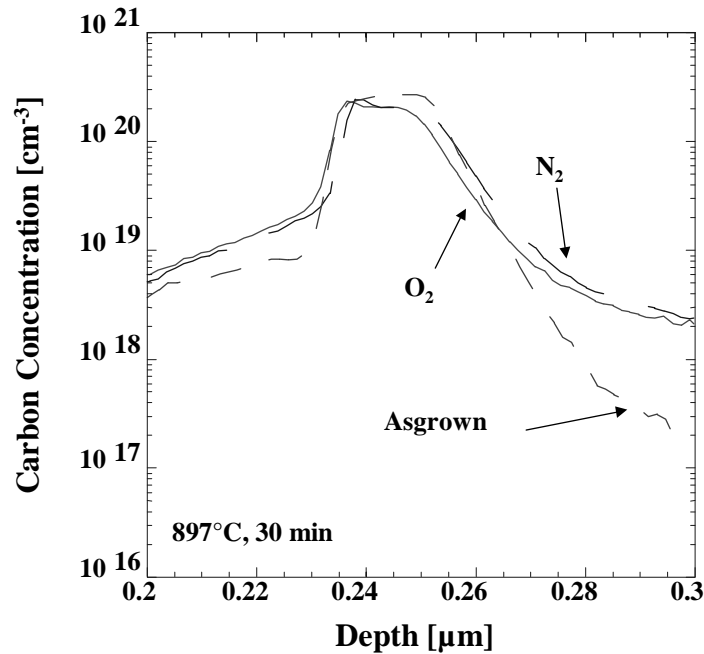


Figure 4.10 Carbon concentration profiles (measured using SIMS) of samples that were as-grown, or annealed at 897°C for 30 minutes in nitrogen ambient, or annealed at 897°C for 30 min in oxygen ambient.

4.5 Summary

In summary, boron OED and TED in silicon has been completely suppressed by trapping excess interstitials in an overlying $\text{Si}_{1-x-y}\text{Ge}_x\text{C}_y$ layer. The boron doped silicon region remains free of carbon under conditions when boron OED/TED is completely suppressed, ruling out $\text{B}_i\text{-C}_s$ as the mechanism responsible for the reduced boron OED/TED. Due to recombination of interstitials at the surface after implantation and an as of yet unquantified interstitial injection rate during oxidation the exact relation-

ship between substitutional carbon and silicon interstitials remains to be resolved in the following chapters.

4.6 References

- [1] L. D. Lanzerotti, J. C. Sturm, E. Stach, R. Hull, T. Buyuklimanli, and C. Magee, *IEDM Tech. Digest*, pp. 249, 1996.
- [2] P. A. Stolk, H.-J. Gossmann, D. J. Eaglesham, and J. M. Poate, *Mat. Sci. & Eng.*, vol. B36, pp. 275-281, 1996.
- [3] H. Ruecker, B. Heinemann, W. Roepke, R. Kurps, D. Krueger, G. Lippert, and H. J. Osten, "Suppressed diffusion of boron and carbon in carbon-rich silicon," *Appl. Phys. Lett.*, vol. 73, pp. 1682, 1998.
- [4] R. Scholz, U. Goesele, J. Y. Huh, and T. Y. Tan, *Appl. Phys. Lett.*, vol. 72, pp. 2, 1998.
- [5] A. Mocuta, R. Strong, and D. Greve, presented at Electronic Materials Conference (40th), Charlottesville, VA, 1998.
- [6] L. D. Lanzerotti, J. C. Sturm, E. Stach, R. Hull, T. Buyuklimanli, and C. Magee, *Appl. Phys. Lett.*, vol. 70, pp. 23, 1997.
- [7] P. A. Stolk, H.-J. Gossmann, D. J. Eaglesham, D. C. Jacobson, C. S. Rafferty, G. H. Gilmer, M. Jaraiz, J. M. Poate, H. S. Luftmann, and T. E. Haynes, "Physical mechanisms of transient enhanced dopant diffusion in ion-implanted silicon," *J. Appl. Phys.*, vol. 81, pp. 6031, 1997.
- [8] H. J. Osten, G. Lippert, P. Gaworzewski, and R. Sorge, *Appl. Phys. Lett.*, vol. 71, pp. 11, 1997.
- [9] G. Davies and R. C. Newman, "Carbon in monocrystalline Silicon," in *Handbook on Semiconductors*, T. S. Moss, Ed., 1994, pp. 1558.
- [10] M. Carroll, C.-L. Chang, J. C. Sturm, and T. Buyuklimanli, "Complete suppression of boron transient-enhanced diffusion and oxidation-enhanced diffusion in silicon using localized substitutional carbon incorporation," *Appl. Phys. Lett.*, vol. 73, pp. 3695, 1998.
- [11] M. S. Carroll, L. D. Lanzerotti, and J. C. Sturm, "Quantitative measurement of reduction of boron diffusion by substitutional carbon incorporation," presented at Diffusion Mechanisms in Crystalline Materials, San Francisco, 1998.
- [12] M. S. Carroll, J. C. Sturm, and C.-L. Chang, "Quantitative measurement of reduction of phosphorus diffusion by substitutional carbon incorporation," presented at Proceedings of the 1999 MRS Spring Meeting - Symposium on 'Si Front-End Processing - Physics and Technology of Dopant-Defect Interactions', San Francisco, CA, USA, 1999.
- [13] J. C. Sturm, P. V. Schwartz, E. J. Prinz, and H. Manoharan, *J. Vac. Sci. Tech. B*, vol. 9, pp. 2011, 1991.
- [14] Fahey, P. B. Griffin, and J. D. Plummer, *Rev. Mod. Phys.*, vol. 61, pp. 289, 1989.

- [15] M. R. Pinto, D. M. Boulin, C. S. Rafferty, R. K. Smith, W. M. Coughran, I. C. Kizilyalli, and M. J. Thoma, *Tech. Digest IEDM*, pp. 923, 1992.
- [16] N. Moriya, L. C. Feldman, S. W. Downey, C. A. King, and A. B. Emerson, "Interfacial Segregation in Strained Heterostructures: Boron in $\text{Si}_{0.8}\text{Ge}_{0.2}/\text{Si}$," *Phys. Rev. Lett.*, vol. 75, pp. 1981, 1995.
- [17] S. M. Hu, D. C. Ahlgren, P. A. Ronsheim, and J. O. Chu, *Phys. Rev. Lett.*, vol. 67, pp. 1450-53, 1991.
- [18] W. Fang, P. Griffin, and J. Plummer, presented at Materials Research Symposium, 1995.
- [19] A. Ural, P. B. Griffin, and J. D. Plummer, "Fractional contributions of microscopic diffusion mechanisms for common dopants and self-diffusion in silicon," *J. Appl. Phys.*, vol. 85, pp. 6440, 1999.
- [20] J. W. Strane, H. J. Stein, S. R. Lee, S. T. Picraux, J. K. Watanabe, and J. W. Mayer, *J. Appl. Phys.*, vol. 76, pp. 3656, 1994.
- [21] W. J. Taylor, W. Y. Tan, and U. Goesele, *Appl. Phys. Lett.*, vol. 62, pp. 2336, 1995.

Quantitative Measurement of the Surface Silicon Interstitial Boundary Condition and Silicon Interstitial Injection into Silicon during Oxidation

5.1 Introduction

In the previous chapter, it was found that if enough substitutional carbon was added to a SiGe layer, then the resulting SiGeC layer could act to completely prohibit interstitials from passing beyond the layer. The SiGeC layers, therefore, can insulate dopant layers below the SiGeC from TED and OED effects. Furthermore, even when the SiGeC layer was located 250 nm below the diffusing species it reduces the OED enhancement below the pure silicon case, demonstrating that the carbon acts as an effective sink for injected interstitials reducing the total number of interstitials in the surface region. However, to quantify the carbon-interstitial relationship it is necessary to measure both the number of injected interstitials and the number of substitutional carbon affected. Because the number of interstitials injected after typical processes like ion implantation or oxidation are not well characterized, it is necessary to first quantify the interstitial injection. We choose to examine oxidation. Although interstitial formation due to ion implantation is a well studied system due to its importance to transistor fabrication, the interstitial formation and injection processes are known to be complex and difficult to predict because of incomplete knowledge about most key pro-

cesses, including interstitial-vacancy (Frenkel pair) formation by the initial implant, interstitial self-cluster condensation and evaporation kinetics, surface recombination and generation rates, Frenkel pair post implant recombination and interstitial annihilation due to amorphization and subsequent recrystallization. In this chapter, using modified boron marker layer test structures, the interstitial profile above the SiGeC layer is mapped out. From this profile we are able to quantify the interstitial boundary condition during oxidation and thereby determine the number of injected interstitials from the surface. The following chapter will use this chapter's results to quantify the loss of substitutional carbon for a known interstitial injection rate.

5.2 Interstitial profile above buried SiGeC layers

5.2.1 Test structures

Test structures were grown to measure the local boron diffusivity throughout the surface region of samples containing zero (sample A), one (sample B), or two (sample C) buried $\text{Si}_{0.795}\text{Ge}_{0.2}\text{C}_{0.005}$ layers (Fig 5.1(a), (b), and (c) respectively). The test structures were epitaxial layers grown on silicon substrates using rapid thermal chemical vapor deposition (RTCVD) at temperatures between 625°C and 750°C using dichlorosilane, germane, and methylsilane as the silicon, germanium and carbon sources respectively [1]. Each test structure was grown on a p-type Czochralski (CZ) (100) silicon wafer and was grown on both the top and bottom surface of the silicon wafer because of the reactor geometry. The three different test structures were grown with

four 25 nm thick boron marker layers that had peak concentrations of $4\text{-}9 \times 10^{18} \text{ cm}^{-3}$ centered below the surface at 150, 450, 600, and 900 nm depths. Sample B was grown with one 20 nm thick $\text{Si}_{0.795}\text{Ge}_{0.2}\text{C}_{0.005}$ layer centered at 675 nm below the surface; sample C was grown with two 20 nm thick $\text{Si}_{0.795}\text{Ge}_{0.2}\text{C}_{0.005}$ layers centered at 300, and 675 nm below the surface. Because of non-uniformity across the wafer surface the depths of the boron layers differed from the nominal values, unintentionally, as much as 30% from sample to sample.

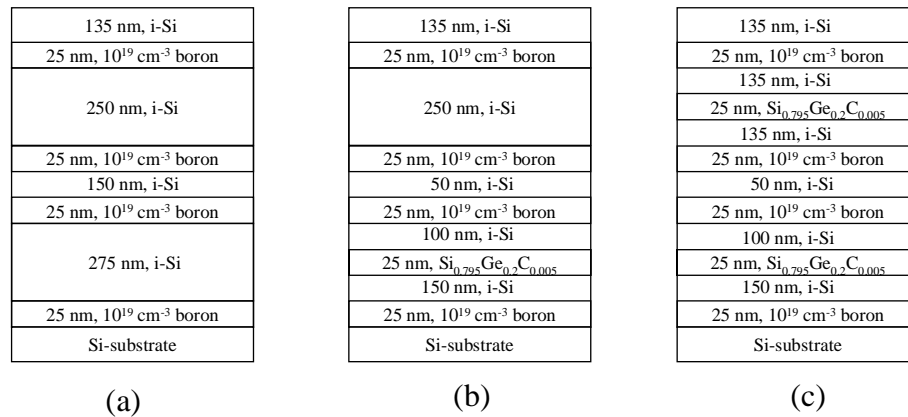


Figure 5.1. Schematic diagram of the test structures A, B, and C ((a), (b), and (c) respectively) used in this experiment.

All test structures were cleaved and annealed in an oxygen or nitrogen ambient for various times between 30 and 960 minutes at 750°C or 850°C , and the resulting boron, carbon, germanium and oxygen profiles were obtained using secondary ion mass spectrometry (SIMS) done at Evans East in East Windsor, NJ. Samples were

sputtered using 2 keV Cs⁺ ions, and depths were determined using standard profilometry of the sputtered craters leading to a 5% uncertainty in depths and a 20% uncertainty in boron concentrations. The oxide growth rates measured by ellipsometry were 0.33 Å/min and 0.91 Å/min at 750°C and 850°C respectively, in agreement with previous reports of thin silicon oxide films [2]. No systematic difference was observed between the oxidation rate of silicon surfaces containing buried SiGeC layers and those without buried SiGeC layers. The most silicon consumed was 130Å. This was ignored in subsequent analysis where the depths from the surface were required.

Boron profiles of the pure silicon structure (sample A) after annealing at 850°C for 30 minutes in oxygen or nitrogen ambient are noticeably broader than the as-grown case (Fig. 5.2(a)). Moreover, the boron profiles in sample A after annealing

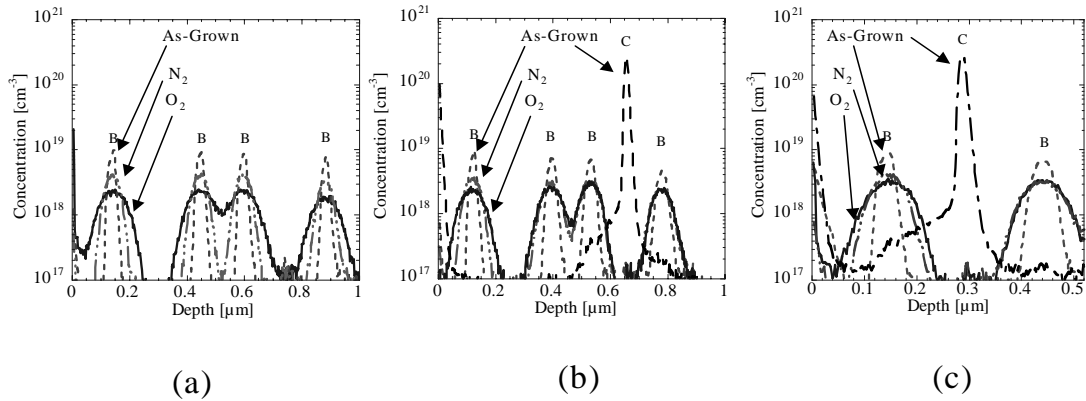


Figure 5.2. Boron and carbon concentration profiles from SIMS of as-grown (dashed line, labeled B and C above the respective profiles) and boron concentrations for samples annealed for 30 minutes at 850°C in either oxygen (solid line) or nitrogen (solid-dashed line) ambients for structures A, B, and C ((a), (b), and (c)) respectively.

in oxygen ambient are clearly broader, at all depths, than those after nitrogen anneal for the same time and temperature, indicative of the well-documented oxygen enhanced diffusion effect [3]. Boron profiles in the two samples containing $\text{Si}_{0.795}\text{Ge}_{0.2}\text{C}_{0.005}$ layers before and after annealing in the identical conditions as in sample A (Fig. 5.2(b) and (c)) show different behavior above and below the buried

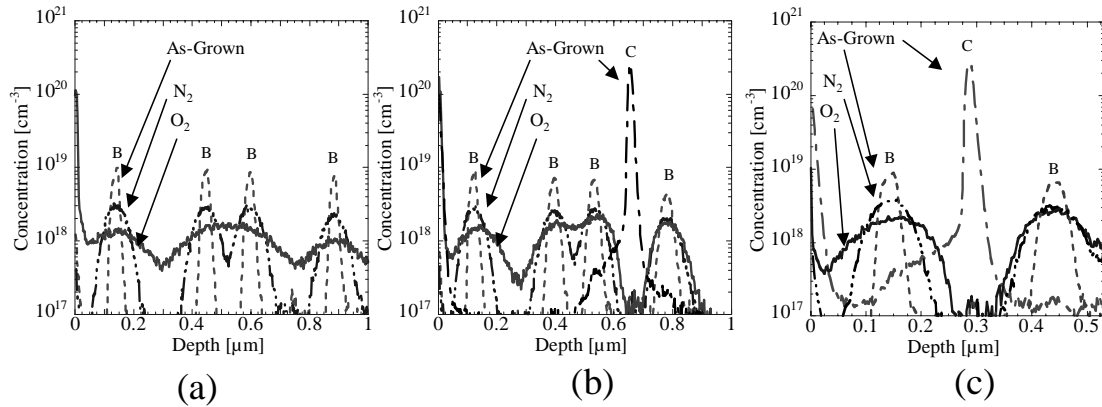


Figure 5.3. Boron and carbon concentration profiles from SIMS of as-grown (dashed line, labeled B and C above the respective profiles) and boron concentrations for samples annealed for 120 minutes at 850°C in either oxygen (solid line) or nitrogen (solid-dashed line) ambients for structures A, B, and C ((3a), (3b), and (3c)) respectively.

$\text{Si}_{0.795}\text{Ge}_{0.2}\text{C}_{0.005}$ layers. Boron profiles below the $\text{Si}_{0.795}\text{Ge}_{0.2}\text{C}_{0.005}$ layers after 30 minutes of oxidation are identical to those after nitrogen anneal. As discussed in the previous chapter, the carbon layer prohibits interaction between the injected interstitials from the surface region and the boron below the carbon layer for this oxidation condition [4]. Boron profiles after oxidation above the $\text{Si}_{0.795}\text{Ge}_{0.2}\text{C}_{0.005}$ layers are, however, broader than their respective counterparts annealed in nitrogen ambient. The

differences in boron profile widths after oxidation versus nitrogen anneals, from marker to marker, are not however uniform. The profiles are clearly broader the

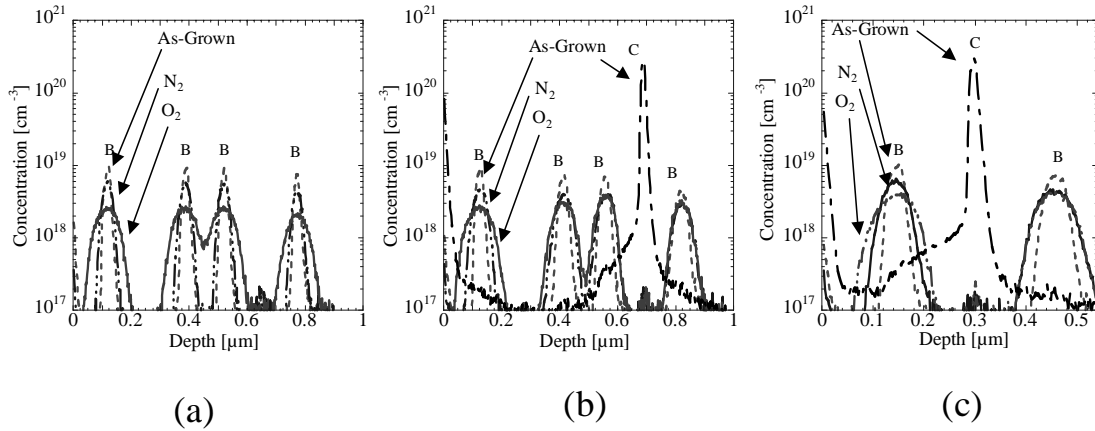


Figure 5.4. Boron and carbon concentration profiles, from SIMS of as-grown (dashed line, labeled B and C above the respective profiles) and boron concentrations for samples annealed for 240 minutes at 750°C in either oxygen (solid line) or nitrogen (solid-dashed line) ambients for structures A, B, and C ((4a), (4b), and (4c)) respectively.

nearer the boron marker is to the surface (Fig. 5.2(b)). The depth dependent diffusivity indicates a gradient in the interstitial concentration in the surface region. Boron concentration profiles after annealing in nitrogen or oxygen ambient were obtained for a number of different times and temperatures and are shown overlain on their respective as-grown profiles for 850°C after 120 minutes (Fig. 5.3), and for 750°C after 240, and 960 minutes (Fig. 5.4, and Fig. 5.5 respectively).

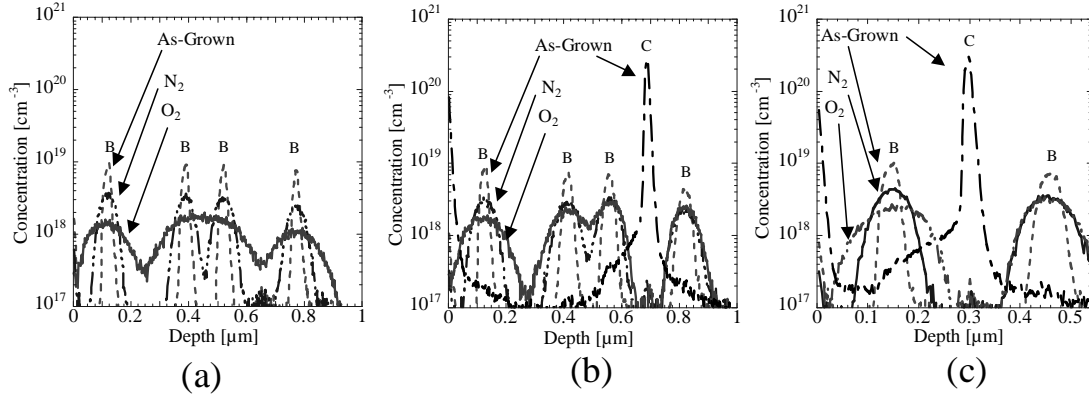


Figure 5.5. Boron and carbon concentration profiles from SIMS of as-grown and boron concentrations for samples annealed for 960 minutes at 750°C in either oxygen or nitrogen ambients for structures A, B, and C ((5a), (5b), and (5c)) respectively.

5.2.2 Extraction of Diffusivity Enhancement and Interstitial Profile

Average local boron diffusivities during annealing for each individual boron marker were extracted for each peak of each sample by using PROPHET [5] to numerically solve for the boron profiles after annealing using the as-grown boron concentrations obtained by SIMS as the initial conditions, as described in the previous chapter. Because the local boron diffusivity depends on the local interstitial concentration as:

$$\frac{D_B^{meas}}{D_B^*} \cong \frac{I}{I^*} \quad (5.1)$$

the interstitial supersaturation $\frac{I}{I^*}$ may be mapped throughout the surface region. In

this case, D_B^* is the literature value for the extrinsic diffusivity of boron in silicon,

eq'n. 3.9, and I^* is the intrinsic self-interstitial concentration in the silicon. The boron

diffusivity for the entire depth of the sample was adjusted for each marker layer by varying a single parameter to fit the annealed boron profile of each marker. The fitting parameter was the ratio of the interstitial concentration to the intrinsic interstitial concentration at the boron marker location, $\frac{I}{I^*}$. The interstitial enhancement for each marker during each oxidation for each time and temperature for all the samples obtained this way (see end of paragraph) are shown in figures 5.6 (750°C) and 5.7 (850°C). The relative boron diffusivity (i.e. the $\frac{I}{I^*}$ ratio) measured during nitrogen anneals after all times examined for sample A (pure silicon) were unity within the uncertainty of the measurement, and therefore agreed with those previously reported for the intrinsic boron diffusion in silicon (i.e. the boron diffusion observed during annealing in inert ambient) [6]. The boron diffusivities during nitrogen anneal in the samples containing SiGeC layers were, however, slightly higher than that in the pure silicon sample by a factor of 2-3. The reason for this will be discussed in chapter 6. All enhanced boron diffusivities reported in this chapter are compared to the literature value for the intrinsic boron diffusivity. Note that all boron diffusivities plotted at the SiGeC layer depths are shown in Fig. 5.6 and 5.7 as approximately zero. These values were taken from the results of chapter two, in which it was found that the boron diffusivity was much smaller than the intrinsic boron diffusivity in silicon (even in cases of relatively high interstitial injection). The diffusivities shown for the sample C anneals

of 60 or 120 min at 850°C and 960 min at 750°C were obtained by a second method explained in the following section, which was necessary to accommodate for the asymmetric boron profile.

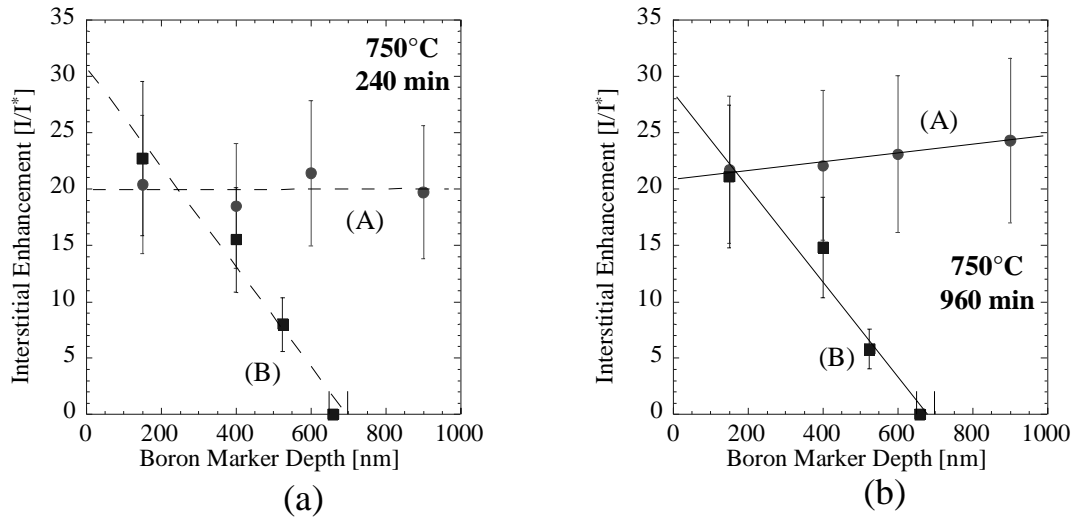


Figure 5.6. Fitted boron diffusivity enhancements for all the samples and their marker depths are shown for oxidations at 750°C for samples A and B after oxidation of (a) 240 minutes and (b) 960 minutes.

The diffusivity enhancement for all the pure silicon samples (A) is found to be fairly uniform throughout the depth of the samples for both temperatures and all times, e.g. Fig. 5.6(a). This is consistent with previous reports of oxidation-enhanced-diffusion that demonstrate that the interstitial point defects, which enhance the boron diffusivity, may diffuse relatively long distances from the surface in a short time [7]. The average diffusivity enhancement in silicon at 750°C and 850°C was found to be approximately 20.5 and 14.8 for the all silicon samples, consistent with previous reports of the oxidation enhanced diffusion of boron [8].

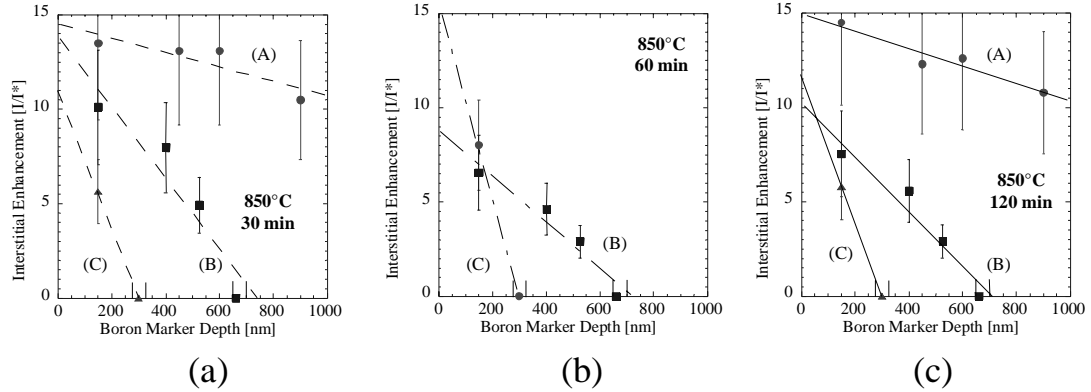


Figure 5.7. Fitted boron diffusivity enhancements for all the samples and their marker depths are shown for oxidations at 850°C for samples A, B and C after oxidation of (a) 30 minutes (b) 60 minutes (no values are available for sample A for this condition), and (c) 120 minutes.

Comparing the diffusivity enhancements from one oxidation time to another in a single sample shows that the enhancements remain relatively constant for all oxidation times. This indicates that the interstitial concentration is in a steady-state condition for these times. Furthermore, as shown in Fig.'s 5.6 and 5.7, in the samples with buried SiGeC layers, the $\frac{I}{I^*}$ ratio during oxidation decays from the surface enhancement to approximately zero at the SiGeC layer and is well approximated by a linear profile versus depth.

The linear fits of the relative interstitial concentration can also be extrapolated to the surface of the silicon/oxide interface from the interstitial profiles in figure 5.6 and 5.7. The extrapolated relative surface interstitial concentrations for each temperature and SiGeC depths, averaging the values for the different oxidation times, are dis-

played versus the depth of the SiGeC layers in figure 5.8. For comparison the surface concentrations obtained for sample A (no SiGeC layer) are shown on the same figure at a depth of 485 μm (the average depth of the back surface from the top surface). The uncertainty of the extrapolated interstitial surface concentrations, resulting from the uncertainty in the best linear fits, is indicated by the error bars in figure 5.8. The surface interstitial concentrations measured for each sample are within 20% of the average surface concentrations (averaged over all samples for each temperature), ~ 25 and ~ 12.7 for 750°C and 850°C, respectively. Possible effects of interstitials diffusing to the top region from the oxidizing back surface, that might affect the measured boron diffusivity enhancements, are neglected in cases B and C, because SiGeC layers were grown on both the top and bottom surfaces. Since the SiGeC layer on the back surface will react with injected interstitials from that surface first and the carbon content has been demonstrated to be enough to sink all injected interstitials, no additional interstitials are expected from the rear surface. This conclusion is supported by the lack of enhanced diffusion of the boron profiles below the SiGeC layer on the top surface. In case A (all-silicon sample) boron diffusivity enhancements have been previously found to be completely independent of the proximity of local interstitial sources and drains like a rear oxidizing surface as close as 20 μm [9, 10], which is consistent with this work's observation that the surface concentration is relatively independent of the

depth of the interstitial sink, even when the nearby interstitial concentration is significantly altered by the presence of the interstitial sink.

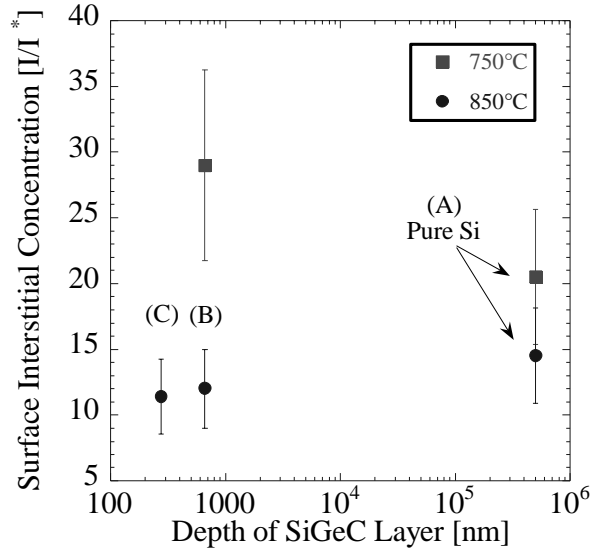


Figure 5.8. Relative interstitial super-saturation at the surface of the silicon during oxidation estimated from the boron diffusivity enhancement profiles versus the SiGeC layer depth. For comparison, the depth of the rear surface is used to represent the pure silicon case located approximately 500 μm from the top surface.

5.3 Boron Diffusion in a Linear Diffusivity Gradient

The above method for extraction of the boron diffusivity could be used as long as the

boron peaks remained narrow and the ratio of $\frac{I}{I^*}$ (or boron diffusivity enhancement)

is approximately constant over the region in which the boron is diffusing. However, in

sample C ($\text{Si}_{0.795}\text{Ge}_{0.2}\text{C}_{0.005}$ layer ~ 30 nm below the surface), the boron concentration

profile after 120 minutes of oxidation at 850°C and 960 minutes at 750°C are clearly

very asymmetric (Fig. 5.3(c) and 5.5(c)) due to the diffusion in a steep interstitial gra-

dient in the surface region. Near the surface the diffusion coefficient is substantially higher than near the SiGeC layer. It is no longer appropriate to extract a single diffusivity from the boron profiles in these cases. Therefore, for sample C it was necessary to simulate the boron diffusion in a diffusivity gradient to reproduce the asymmetric broadening and estimate the boron diffusivity enhancement. Boron profiles after annealing were simulated, using PROPHET, with a linearly decaying interstitial enhancement profile (i.e. boron diffusivity). The interstitial concentration was assumed pinned at zero at the SiGeC layer, and the interstitial enhancement at the surface ($n_{surf} \equiv \frac{I_{surf}}{I^*}$) was used as a single adjustable parameter to fit simulated profiles with the data. Fig. 5.9 shows the excellent fit of the modeling with the data, supporting the assumption of a linearly decaying interstitial enhancement profile. (For reference the carbon profiles before and after oxidation are also shown in figure 5.9 and also show that the carbon profile has not changed appreciably in the surface region.)

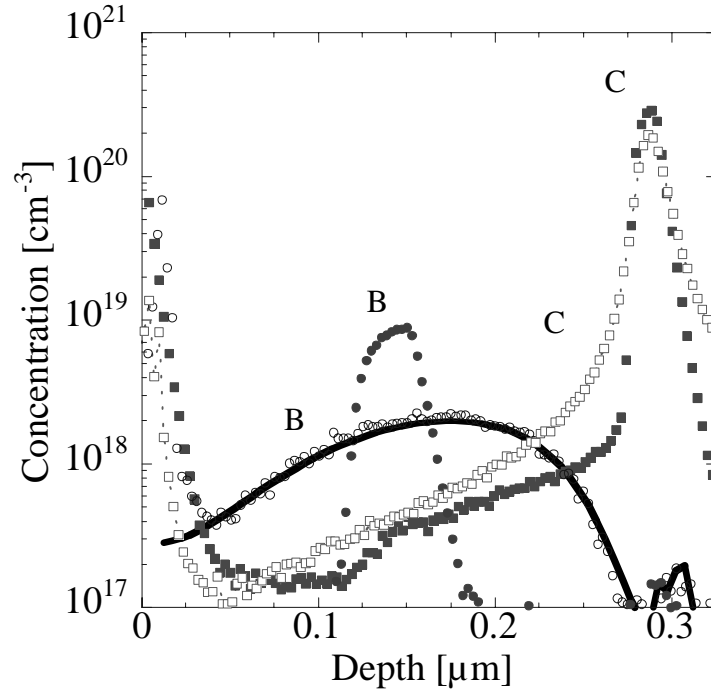


Figure 5.9. (a) As-grown boron and carbon concentration profiles overlain on boron and carbon profiles after 120 minutes oxidation at 850°C and simulated profile (solid line) of the interstitial enhancement after oxidation for 120 minutes at 850°C for sample C (SiGeC layer located 300 nm below the surface).

5.4 Interstitial Injection Rate

5.4.1 Calculation of Interstitial Injection Rate

If the interstitial concentration at the surface, I_{surf} , and the interstitial diffusivity, D_i^* ,

were known one could easily calculate the diffusion flux of interstitials from the surface for a given SiGeC layer depth, assuming a linear decay of the concentration profile.

However, we have measured the relative interstitial enhancement, $\frac{I}{I^*}$, and the

actual intrinsic concentration and diffusivity of silicon self-interstitials is unknown. Nevertheless we can still calculate the flux because the interstitial transport product $D_i^* I^*$ ($68 \text{ cm}^{-1}\text{s}^{-1}$ and $1 \times 10^4 \text{ cm}^{-1}\text{s}^{-1}$ for 750°C and 850°C , respectively) has been measured reliably using metal tracer diffusion [11]. For samples B and C the silicon interstitial flux, J_i , injected into the silicon may be calculated by,

$$J_i = -D_i^* \frac{dI}{dx} = \frac{I}{I^*} \times \frac{D_i^* I^*}{\Delta x} = n_{surf} \frac{D_i^* I^*}{\Delta x} \quad (5.2)$$

where, Δx is the depth of the $\text{Si}_{0.795}\text{Ge}_{0.2}\text{C}_{0.005}$ layer, and n_{surf} is the experimentally obtained relative interstitial super-saturation at the surface (Fig 5.8). It is assumed that the interstitial concentration at the SiGeC layer is near zero [4, 12]. Evaluating eq'n. 5.2 for 750°C and 850°C gives:

$$J_i(T = 750^\circ\text{C}) = \frac{2.09 \times 10^3}{\Delta x} \text{ atoms} \cdot \text{cm}^{-1}\text{s}^{-1} \quad (5.3)$$

and

$$J_i(T = 850^\circ\text{C}) = \frac{1.51 \times 10^5}{\Delta x} \text{ atoms} \cdot \text{cm}^{-1}\text{s}^{-1} \quad (5.4)$$

where there is a total 25% uncertainty in the values. Empirically estimating the surface self-interstitial enhancement ratio from Fig. 3.2 as:

$$n_{surf} = 9.33 \times 10^{-3} e^{\frac{0.7 \text{ eV}}{k_B T}} \quad (5.5)$$

the temperature dependence of the self-interstitial injection may also be expressed as:

$$J_I(T, \Delta x) = \frac{1.38 \times 10^{24}}{\Delta x} e^{\frac{-4.25 \text{ eV}}{k_B T}} \text{ atoms} \cdot \text{cm}^{-1} \text{ s}^{-1} \quad (5.6)$$

The total number of injected interstitials for samples B and C can be calculated by integrating the interstitial flux injected during oxidation (eq'n. 5.3 and 5.4) over the oxidation time (960 or 120 minutes at 750°C or 850°C, respectively), Fig. 5.10. In the case of pure silicon, the interstitial diffusion length, assuming the self-interstitial diffusivities from Bracht's work, are of the order of the wafer dimension for the longest oxidation times, i.e. 792 μm or 685 μm for 960 or 120 minutes at 750°C or 850°C, respectively [11]. An order of magnitude estimate of the number of injected interstitials into sample A (pure silicon) can be made, therefore, by assuming that the interstitial concentration has reached a uniform interstitial concentration across the wafer depth equal to the surface concentration by these oxidation times [9]. The total number of injected interstitials, therefore, is half the total increase of interstitials in the entire wafer, i.e. each surface contributes an equal number of interstitials:

$$Q_I = \frac{(n_{surf} - 1) \cdot I^* \cdot w}{2} \quad (5.7)$$

where w is the width of the wafer ($\sim 485 \mu\text{m}$), Q_I is the total number of injected interstitials, and I^* is the literature value for the less well established silicon intrinsic concentration ($6.2 \times 10^8 \text{ cm}^{-3}$ or $1.54 \times 10^{10} \text{ cm}^{-3}$ for 750°C and 850°C, respectively [11]).

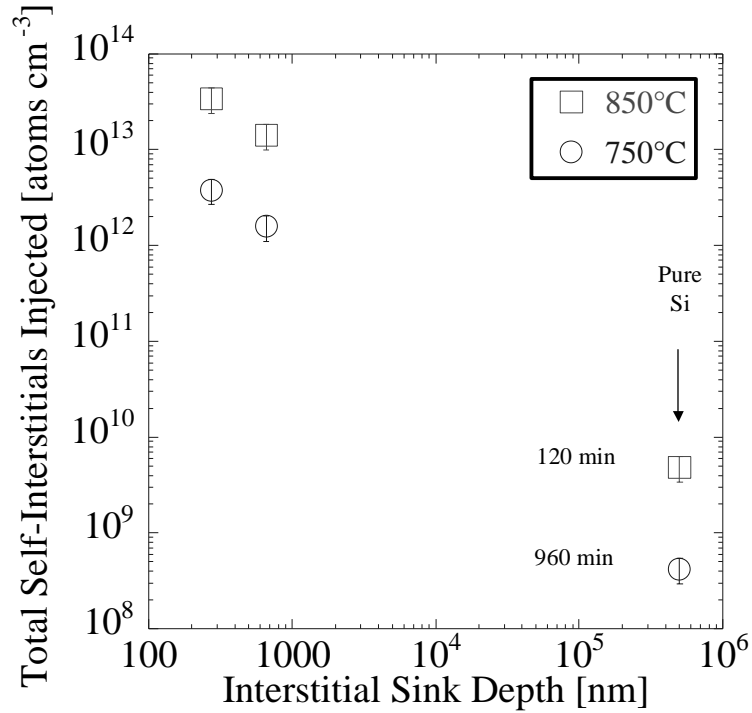


Figure 5.10. The total interstitial atoms integrated over time injected into the silicon after 960 minutes at 750°C or 120 minutes at 850°C of oxidation versus the depth of the interstitial sink, i.e. the SiGeC layer or the bottom surface. The total interstitial areal densities were calculated using equation 2 or 3 and the measured surface supersaturation and SiGeC layer depths.

Samples B and C (those with a buried SiGeC layer) show a significant increase in interstitial flux into the silicon bulk compared to sample A (pure silicon) in figure 5.10. The interstitial flux into the silicon bulk is governed by simple diffusion and is therefore determined entirely by the interstitial gradient. The calculated increase of interstitial injection due to the proximity of the SiGeC layer is, therefore, because the SiGeC layer acts as a local sink for injected interstitials reducing the interstitial concentration in the region directly below the surface, which in turn draws more intersti-

tials from the surface into the bulk. When there is no SiGeC layer present the interstitial concentration rapidly increases and approaches the surface concentration, which reduces the interstitial gradient at the surface and therefore reduces the interstitial flux into the silicon from the surface (sample A, pure silicon).

5.4.2 Discussion and Comparison to Other Work

The observation that the surface super-saturation of interstitials remains unchanged (no more than 20% variation from the average) despite an increase of the total number of injected silicon interstitials qualitatively agrees with the proposed oxidation model by Dunham [13-15]. This model predicts that the interstitial concentration at the silicon surface is pinned by a large reservoir of silicon interstitials that form and reside at the oxide/silicon interface above the silicon surface. Briefly, Dunham et al. propose that in the linear oxidation regime a constant interstitial concentration at the oxide/silicon interface results from the detailed balance between the generation of interstitial silicon atoms from the oxidation reaction and primarily the loss of interstitial silicon atoms to diffusion from the interface towards the oxide surface. Presumably this diffusive flux is independent of the oxide thickness, because all the interstitial silicon in the oxide (a relatively small number compared to the number of oxygen forming the oxide) react completely with the oxygen species diffusing in towards the silicon surface in a distance much smaller than the oxide thickness. Naturally, there is a transient time expected for the steady-state condition and the initial oxide formation.

The interstitial concentration measured on the silicon side is predicted, then to be a small fraction of that on the oxide side, due to a segregation effect driven by the energetically favorable difference in strain. These combined processes, therefore, create an effective reservoir of interstitials on the oxide side, which pin the interstitial concentration at the silicon surface.

This is the first report, of which the author is aware, that shows the boundary condition remains constant, at 850°C, for interstitial injection rates ranging over 4 orders of magnitude. This demonstrates the stiffness of the surface boundary condition during oxidation and suggests that the surface concentration of interstitials in the silicon is determined by an interstitial reservoir at the silicon/oxide interface created by the oxidation.

Recently, the integrated interstitial flux over time due to oxidation was also measured by monitoring the increase in size of type II loop defects located 110 nm below the surface of an oxidized sample [16]. Because loops grow by collecting interstitials, from the number of loops and their growth rate (observed by TEM) one can directly calculate the number of interstitials consumed. The density of the loops has been determined to be high enough to capture most of the injected interstitials, therefore, their growth is a measure of the total number of injected interstitials. No knowledge of diffusion coefficients or interstitial enhancement values is required. From Eq'n (5.2), assuming that the interstitial profile decays linearly to zero at the interstitial sink (i.e. the loop defects), we may expect that the flux of interstitials into the sam-

ple with buried loop defects, during oxidation, is constant through out the oxidation time and depends inversely on the depth of the loop defects. To compare our work with reference [16] for different oxidation times and sink depth, the total number of interstitials reported by the growth of loop defects is divided by the reported oxidation time (60 and 120 minutes) to obtain the constant flux during oxidation. The calculated flux for the loop defect experiment is compared to those calculated for the two samples B and C after 60 and 120 minutes of oxidation for their respective inverse depths. As can be seen in figure 5.11, the interstitial fluxes are proportional to the inverse depths of the interstitial sinks and therefore are well fit by a line for both times. The loop measurement of the total integrated interstitial injection agrees well with the boron marker measurements of interstitial injection during oxidation. Furthermore, the observation that the interstitial injection depends inversely on the depth of the buried interstitial sink is also in agreement with the observed dependence of loop defect growth for loops located at varying depths from the surface after oxidation [17].

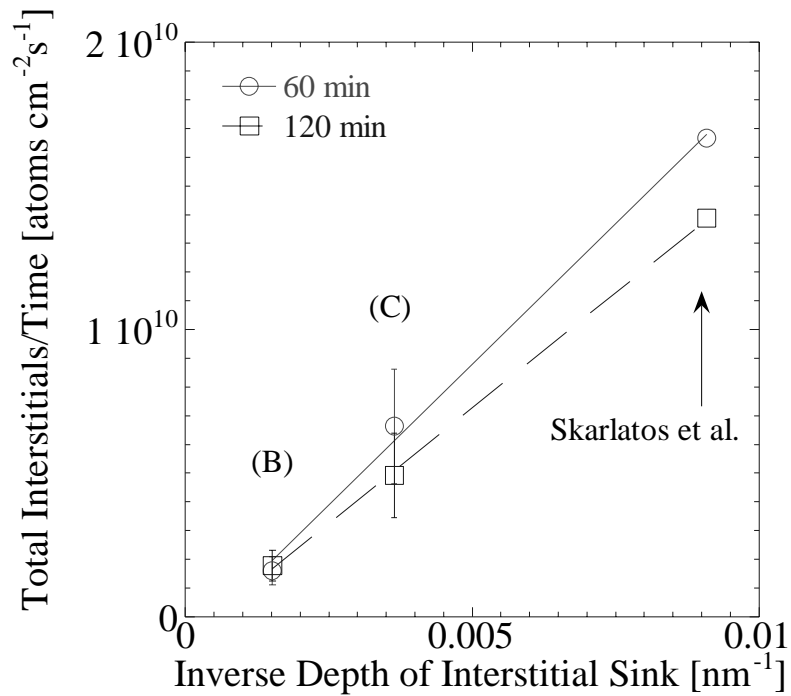


Figure 5.11. The total number of injected silicon interstitials after oxidation measured using type II loop defects [16] divided by the oxidation time (i.e. constant interstitial flux during oxidation) compared to the interstitial flux measured by the boron marker method (this work) is compared for their respective inverse depths. The linear fits for the two oxidation times show the flux is proportional to the inverse depth.

Although both phosphorus and boron are believed to diffuse almost entirely by an interstitial(cy) mechanism [18, 19] the boron diffusion enhancements during oxidation are often slightly lower (~30% at 850°C) than that of the phosphorus, [15, 20]. A possible reason for this is boron cluster effects [21], which could temporarily trap mobile boron and reduce the effective diffusivity causing an underestimate of the true interstitial injection by the method presented in this work. However, the good agreement between the measurements in this work and that from the growth of loop defects,

which is independent of boron clustering effects, indicates that there are no significant reductions in boron diffusivity in our work leading to an appreciable underestimate of interstitial injection. Presumably, the interstitial concentration is still too small to observe the boron clustering that is observed after implantation. No comparison was available for 750°C, which may be because the number of injected interstitials calculated from our data is far below the currently reported resolution of the loop defect method of $2\text{-}3 \times 10^{13}$ atoms/cm². This demonstrates the sensitivity of our approach for measuring the total number of injected interstitials at very low injection rates limited primarily by the ability to measure small diffusion lengths (~ 1-2 nm by SIMS) necessary to establish the interstitial profile.

5.5 Summary

The average boron diffusivity during oxidation above Si_{0.795}Ge_{0.2}C_{0.005} layers has been used to map the profile of interstitials injected into silicon during oxidation, and also to quantify the total number of interstitials injected into the silicon substrate. The interstitial super-saturation concentration at the surface for 750°C and 850°C has been determined and the average interstitial super-saturation concentration is found to depend weakly, if at all, on the rate of interstitial injection into the bulk silicon, despite increasing the total number of injected interstitials by 4 orders of magnitude. In the following chapter we will quantify the loss of substitutional carbon in similar conditions as these for which we know the interstitial injection rate.

5.6 References

- [1] J. C. Sturm, P. V. Schwartz, E. J. Prinz, and H. Manoharan, *J. Vac. Sci. Tech. B* , vol. 9, pp. 2011, 1991.
- [2] E. A. Irene, *J. Electrochem. Soc.* , vol. 125, pp. 1708, 1978.
- [3] D. A. Antoniadis and I. Moskowitz, *J. Appl. Phys.* , vol. 53, pp. 6788, 1982.
- [4] M. Carroll, C.-L. Chang, J. C. Sturm, and T. Buyuklimanli, "Complete suppression of boron transient-enhanced diffusion and oxidation-enhanced diffusion in silicon using localized substitutional carbon incorporation," *Appl. Phys. Lett.* , vol. 73, pp. 3695, 1998.
- [5] M. R. Pinto, D. M. Boulin, C. S. Rafferty, R. K. Smith, W. M. Coughran, I. C. Kizilyalli, and M. J. Thoma, *Tech. Digest IEDM* , pp. 923, 1992.
- [6] R. B. Fair, "Processing Technologies" , vol. Supplement 2B. New York: Academic, 1981.
- [7] H.-J. Gossmann, C. S. Rafferty, H. S. Luftmann, F. C. Unterwald, T. Boone, and J. M. Poate, "Oxidation enhanced diffusion in Si B-doping superlattices and Si self-interstitial diffusivities," *Appl. Phys. Lett.* , vol. 63, pp. 639, 1993.
- [8] P. Kuo, J. L. Hoyt, J. F. Gibbons, J. E. Turner, and D. Lefforge, "Effects of Si thermal oxidation on B diffusion in Si and strained SiGe layers," *Appl. Phys. Lett.* , vol. 67, pp. 706, 1995.
- [9] S. T. Ahn, J. D. Shott, and W. A. Tiller, presented at Extended Abstracts of the Electrochemical Society Meeting, 1986.
- [10] Fahey, P. B. Griffin, and J. D. Plummer, *Rev. Mod. Phys.* , vol. 61, pp. 289, 1989.
- [11] H. Bracht, N. A. Stolwijk, and H. Mehrer, *Phys. Rev. B.* , vol. 52, pp. 16542, 1995.
- [12] R. F. Scholz, P. Werner, U. Goesele, and T. Y. Tan, *Appl. Phys. Lett.* , vol. 74, pp. 392, 1999.
- [13] S. T. Dunham and J. D. Plummer, "Point-Defect Generation during Oxidation of Silicon in Dry Oxygen Part 2: Comparison to Experiment," *J. Appl. Phys.* , vol. 59, pp. 2551, 1986.
- [14] S. T. Dunham and J. D. Plummer, "Point-Defect Generation during Oxidation of Silicon in Dry Oxygen Part 1: Theory," *J. Appl. Phys.* , vol. 59, pp. 2541, 1986.
- [15] S. T. Dunham and J. D. Plummer, "Interactions of silicon point defects with SiO₂ films," *J. Appl. Phys.* , vol. 71, pp. 685, 1992.
- [16] D. Skarlatos, M. Omri, A. Claverie, and D. Tsoukalas, *J. Electrochem. Soc.* , vol. 146, pp. 2276, 1999.
- [17] D. Tsoukalas, D. Skarlatos, and J. Stoemenos, *J. Appl. Phys.* , vol. 87, pp. 8380, 2000.

- [18] A. Ural, P. B. Griffin, and J. D. Plummer, "Fractional contributions of microscopic diffusion mechanisms for common dopants and self-diffusion in silicon," *J. Appl. Phys.* , vol. 85, pp. 6440, 1999.
- [19] H.-J. Gossmann, T. E. Haynes, P. A. Stolk, D. C. Jacobson, G. H. Gilmer, J. M. Poate, H. S. Luftman, T. K. Mogi, and M. O. Thompson, *Appl. Phys. Lett.* , vol. 71, pp. 3862, 1997.
- [20] Roth and Plummer, *J. Electrochem. Soc.* , vol. 141, pp. 1074, 1994.
- [21] P. A. Stolk, H.-J. Gossmann, D. J. Eaglesham, D. C. Jacobson, C. S. Rafferty, G. H. Gilmer, M. Jaraiz, J. M. Poate, H. S. Luftmann, and T. E. Haynes, "Physical mechanisms of transient enhanced dopant diffusion in ion-implanted silicon," *J. Appl. Phys.* , vol. 81, pp. 6031, 1997.

Diffusion Enhanced Carbon Loss from SiGeC Layers due to Oxidation

6.1 Introduction

The work in the previous chapters established that substitutional carbon reacts with silicon interstitials. However, the potential that the interstitial-carbon product is a defect (i.e. β -SiC precipitation or carbon clusters [1, 2]) may limit the usefulness of carbon for controlling boron diffusion in technological applications, which highlights the importance of quantifying the reaction and identifying its product. In this chapter, carbon out-diffusion from thin SiGeC layers is examined and is shown to be the dominant mechanism of substitutional carbon loss from SiGeC layers close to the surface. That is, precipitation is suppressed by the rapid loss of all carbon to the surface and the surrounding unsaturated silicon. Using the results from chapter 5, i.e. the quantification of the interstitial injection rate during oxidation, the number of substitutional carbon removed from the SiGeC layer due to one injected interstitial is quantified in this chapter. This is one of the main contributions of this thesis. Furthermore, a complete quantitative model of the carbon motion is presented that supports the main conclusions of this thesis.

6.2 Substitutional carbon loss after oxidation

Two test structures with 25 nm thick $\text{Si}_{0.7865}\text{Ge}_{0.21}\text{C}_{0.0035}$ layers capped by 300 nm (structure A) or 40 nm (structure B) of silicon were grown by rapid thermal chemical vapor deposition (RTCVD) at temperatures between 625°C and 750°C using dichlorosilane, germane, and methylsilane as the silicon, germanium, and carbon sources respectively [3], Fig. 6.1. Each test structure was grown on a p-type Czochralski (CZ) $\langle 100 \rangle$ silicon wafer. Samples of the as-grown and annealed structures were examined using secondary ion mass spectrometry (SIMS), which were sputtered using 1-2 keV Cs^+ ions, Fig. 6.2, or O^+ ions, Fig 6.3. Depths were determined using standard profilometry of the sputtered craters leading to a 5% uncertainty in depths. A 20%, Fig. 6.2, or 10%, Fig.6.3, relative uncertainty in carbon concentrations and approximately a 2% absolute uncertainty in germanium concentrations were obtained.

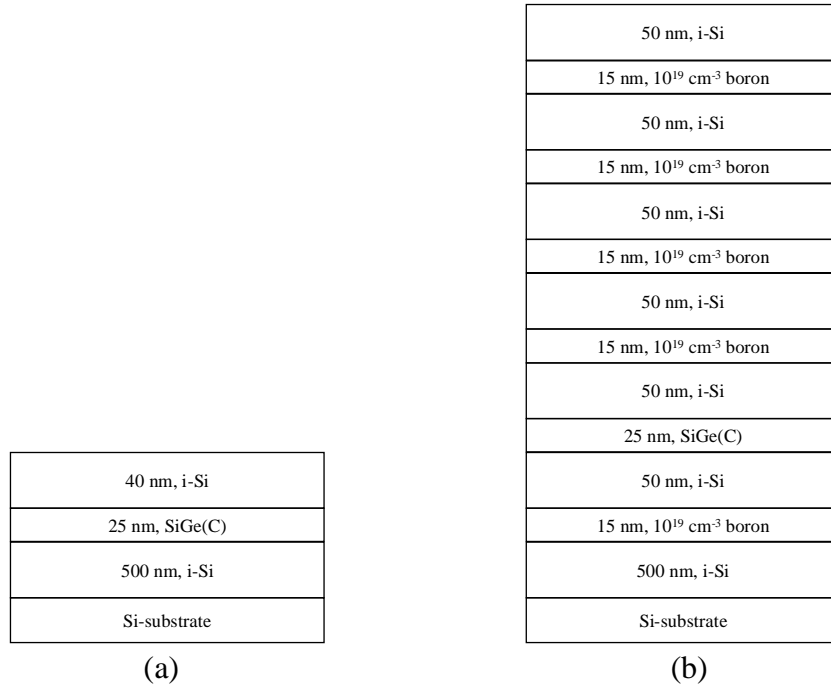


Figure 6.1 Schematic cross section of structures A and B, (a) and (b) respectively.

The as-grown and oxidized samples of structure B were examined by x-ray diffraction (XRD) using a double-crystal rocking curve geometry around the (004) Bragg reflection. Simulation of the rocking curves of the as-grown and oxidized samples were fit to experiment using the substitutional carbon concentration in the SiGe layer as the fitting parameter. The layer thickness and germanium concentration used in the simulation were taken from the SIMS measurements. The carbon concentration extracted from the rocking curve fits agreed well with carbon concentrations obtained by SIMS indicating that the carbon in the SiGeC layer compensated the strain as if it was all substitutional, within the uncertainty of the measurement, Fig. 6.4 and 6.5.

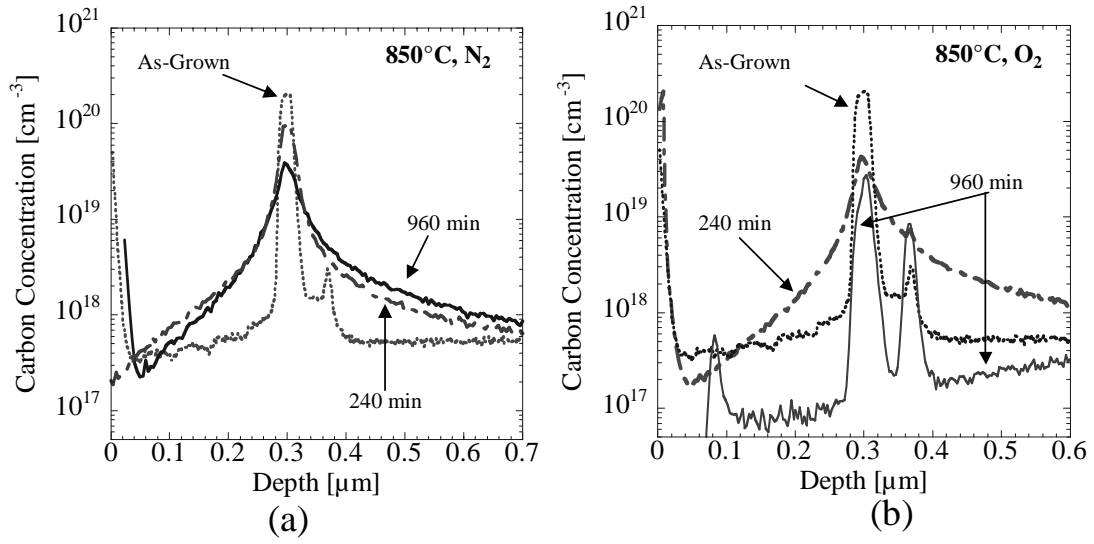


Figure 6.2 Carbon concentration profiles from samples of structure A with buried SiGeC layers before and after annealing at 850°C in nitrogen or oxygen ambient for 240-960 minutes overlaid on the as-grown carbon profile, (a) and (b) respectively.

The strain compensation relationship between germanium and carbon used was 12:1 [4]. As-grown and 960 minute nitrogen or oxygen annealed samples of structure A were also examined for relaxation in the plane parallel to the growth surface by scanning around the (224) Bragg reflection. No relaxation by misfit dislocations was observed. Note: The X-ray rocking curves and fits of sample A and B were done by Dr. D. Tweet at Sharp Labs, WA and Dr. J. Stangl at the University of Linz, Austria respectively.

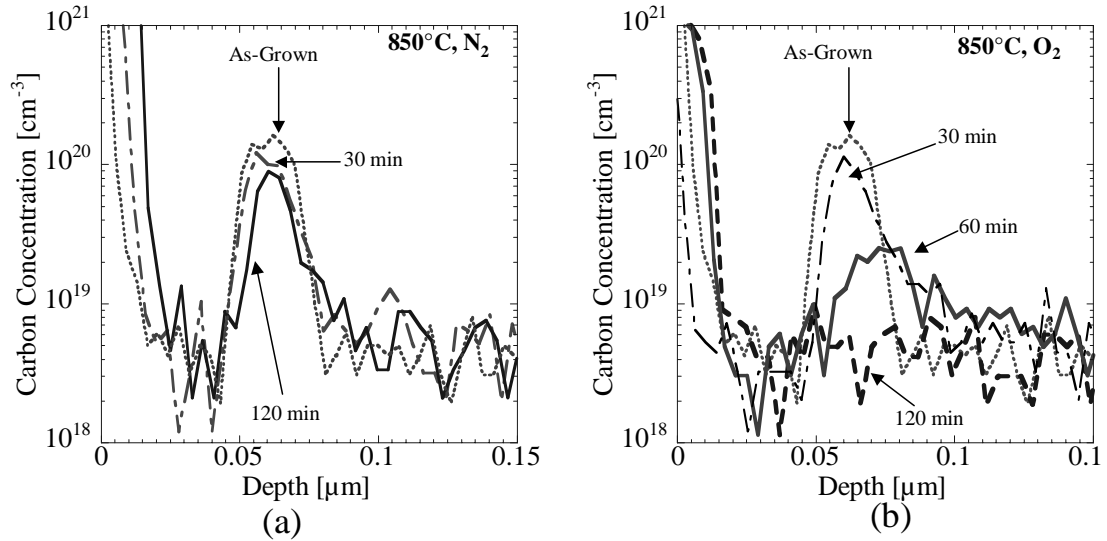


Figure 6.3 Carbon concentration profiles from samples of structure B with buried SiGeC layers before and after annealing at 850°C in nitrogen or oxygen ambient for 30-120 minutes overlaid on the as-grown carbon profile, (a) and (b) respectively.

Carbon profiles from samples of structure A, 300 nm silicon cap, annealed in nitrogen ambient for 240 or 960 minutes are overlaid on the as-grown carbon profile, Fig. 6.2 (a). The appearance of carbon tails, indicative of carbon out-diffusion, is observed after annealing. Carbon is believed to diffuse via an interstitial(cy) mechanism when the carbon concentration is below solid solubility [5, 6],



where C_s is a carbon atom in a substitutional site, I is the silicon interstitial, and C_i is the mobile interstitial carbon defect. Whether the carbon in the tails is actually C_i or whether it has temporarily been driven substitutional by the reverse reaction releasing a silicon self-interstitial will be discussed in the section 6.3. The non-Gaussian carbon

profiles after nitrogen annealing in this case indicate a suppressed carbon diffusivity in the carbon supersaturated silicon region. The asymmetry of the carbon profiles after annealing, i.e. lower carbon concentrations on the surface side of the SiGeC layer, indicates that there is carbon loss from the sample due to carbon diffusion towards and out of the top surface. Previous studies have also reported loss of carbon from slightly carbon enriched ($8 \times 10^{17} \text{ cm}^{-3}$) crystalline silicon out the surface after annealing in either an oxygen or nitrogen ambient [5].

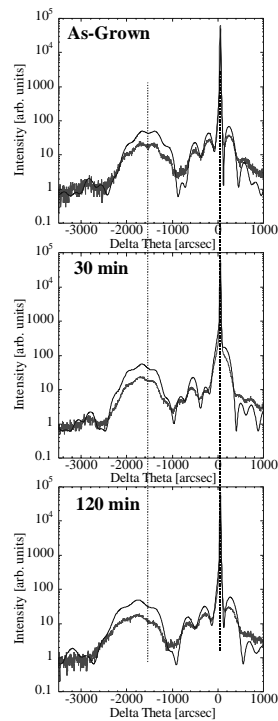


Figure 6.4 X-ray diffraction rocking curves of samples of structure B before and after annealing at 850°C in oxygen for 0-120 minutes. Rocking curves measured by J. Stangl at the University of Linz.

The rate of carbon loss from the SiGeC layer is enhanced by oxidation, Fig. 6.2 (b), and the carbon is reduced well below the as-grown background concentration ($3 \times 10^{17} \text{ cm}^{-3}$), except two spikes of immobile carbon after 960 minutes of oxidation located at 300 and 370 nm. The oxide-silicon interface is indicated by the carbon spike located at a depth of 100 nm in this sample. There is a carbon spike which is initially small and then grows during oxidation outside the SiGeC layer at 370 nm depth in the as-grown sample Fig. 6.2 (a) and (b). This was unintentional and it is centered at the same location as a buried 15 nm wide boron layer (grown to examine D_B at that location). Carbon may be preferentially incorporated on boron doped silicon surfaces during RTCVD or there may be a contamination issue with the gas source switching. It is unclear whether the enhanced carbon incorporation is substitutional carbon, therefore it is difficult to conclude whether the formation of the immobile carbon at 370 nm depth after oxidation is catalyzed by the surface incorporation during growth or due to the presence of boron after growth during oxidation, although no immobile carbon formation was initiated in the surface region where four identical boron markers were spaced evenly between the surface and the SiGeC layer at depths of 50, 125, 200 and 275 nm. Because the amount of carbon in these immobile layers is small, their effect on the quantification of carbon loss from the sample and SiGeC layer is ignored for the rest of the chapter.

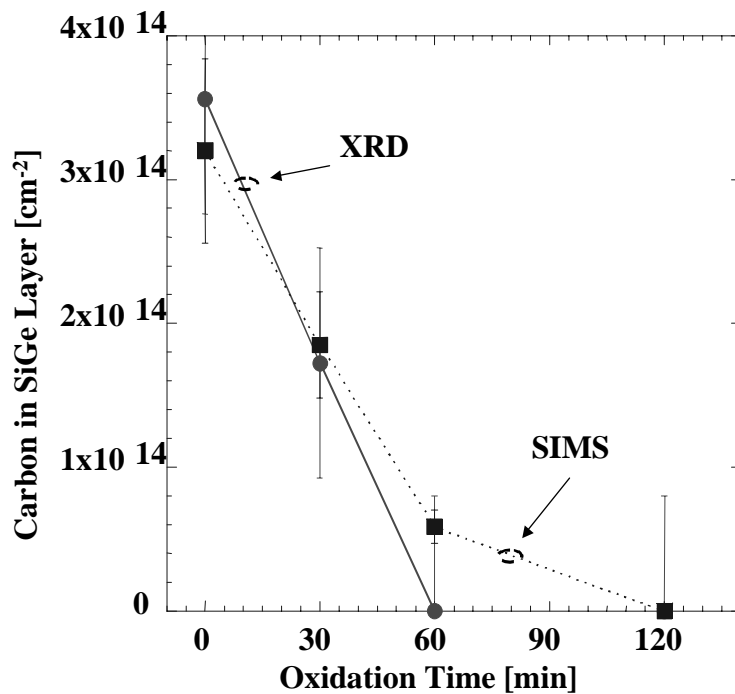


Figure 6.5 Total carbon found in the SiGeC layer of structure B by SIMS compared to the total substitutional carbon extracted from fits of the rocking curves obtained by varying the substitutional carbon content and using the germanium concentrations obtained from SIMS.

In Fig 6.3 (a) the carbon concentration profiles of structure B (40 nm Si cap) of the as-grown and annealed for 30 or 120 minutes in nitrogen ambient are shown. The peak carbon concentration is approximately half the as-grown concentration after 120 minutes of annealing without significant broadening of the carbon profile implying that when carbon diffuses at all, it leaves the SiGeC layer and the sample entirely. Presumably the primary mechanism of loss is diffusion to the surface and the carbon tails, if any, are obscured by the higher carbon detection limits ($3 \times 10^{18} \text{ cm}^{-3}$). The carbon

concentration profiles after oxidation of 30 to 120 minutes, Fig. 3 (b), shows a more rapid decrease of the carbon concentration resulting in no detectable carbon in this sample after 120 minutes of oxidation. Once at the surface the carbon could react with the oxygen to form CO_2 and leave as a volatile product during oxidation, however, this fails to explain the carbon loss from the surface during annealing in nitrogen. As discussed earlier, there is a significant barrier to formation of silicon-carbide precipitation in bulk silicon because of the unusually high surface energies required to form the precipitate (section 2.3.2). Another possibility, is that the silicon-carbide preferentially precipitates at the surface and this reaction consumes the carbon. Quantification of the carbon concentration at the surface is notoriously difficult due to interference with adventitious carbon contamination on the top surface that interferes with the SIMS carbon signal in the top 20 nm. It is not possible, therefore, to determine whether silicon-carbide is forming at the surface during the nitrogen anneal from the SIMS measurements. More work is still required to identify the mechanism responsible for the what the carbon consumption at the sample surface.

Immobile carbon within the SiGeC layer (spike located at 300 nm) is observed in structure A but not in structure B although the initial germanium and carbon concentrations are nearly identical and neither layer was grown with appreciable boron in them (below SIMS detection limits $< 4 \times 10^{16} \text{ cm}^{-3}$). The formation of immobile carbon in the SiGeC layer of structure B is prevented by the rapid carbon out-diffusion to the surface and surrounding silicon compared to structure A. Previous reports of car-

boron precipitation or immobile carbon are typically from much thicker carbon layers (~100 nm thick) in silicon or SiGeC [1, 2, 7]. In these cases the carbon concentration in the middle of the layer remains near the as-grown value longer because the carbon out-diffusion is predominantly at the edges of the layers. Indeed, TEM measurements of thin SiC layers annealed in nitrogen for similar times as in this study showed no signs of precipitates [8]. The formation of immobile carbon in the SiGeC layer due to the presence of boron is not likely. The boron concentration throughout all annealing times was less than $5 \times 10^{17} \text{ cm}^{-3}$ within the SiGeC layer, 100 times less than the final immobilized carbon level, and no immobile carbon or boron was observed in the surface region where the carbon diffused through 4 other identically grown boron layers.

Several key conclusions about the carbon loss from the SiGeC layer of structure B should be emphasized at this point. The rate of carbon loss depends strongly on the carbon layer's proximity to the surface. This can play a critical role in the final chemical composition of a device structure and therefore should be considered in the design of any fabrication process using substitutional carbon. Furthermore, the rapid and complete loss of carbon from the SiGeC layer of sample B after oxidation clearly indicates that the end-product of the reaction between the injected silicon self-interstitial and the substitutional carbon is mobile carbon. No evidence of carbon clusters or precipitation is seen in this important case.

6.3 Quantification of carbon loss

To quantify the loss of carbon from the SiGeC layer and from the sample, the total carbon detected by SIMS in the SiGeC layers (circle) or in all of the sample (square) after annealing in either nitrogen (solid) or oxygen (hollow) is subtracted from the carbon measured in the as-grown samples for both structures A and B, Fig 6.6 (a) and (b), respectively. The rate of carbon loss from both structures after annealing in nitrogen ambient is initially much more rapid than at later times. Presumably this is due to the decreasing concentration gradient of mobile carbon at longer times after the carbon profile has broadened significantly. The rate of carbon loss from the two SiGeC layers is faster after oxidation. After 120 minutes there is no more remaining carbon in structure B while for structure A it takes more than 240 minutes to remove a similar amount of carbon. The amount of carbon lost from structure B is faster than from structure A after the same oxidation condition. The two different rates of extra carbon lost is shown in Fig. 6.7 for structure A (squares) or B (circles). More specifically this represents the carbon lost from the SiGeC layer after oxidation subtracted from that lost after annealing in nitrogen. Clearly, oxidation removes significantly more carbon in structure B than in structure A for the same oxidation time. This is consistent with the result of the previous chapter, in which it was shown that interstitial injection rate depends inversely on the silicon cap thickness.

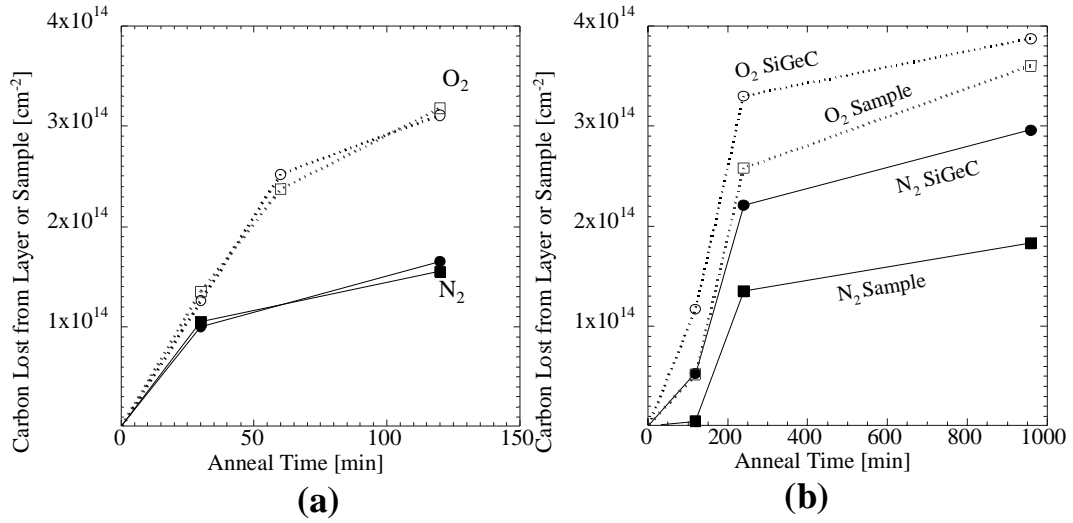


Figure 6.6 Summary of total carbon lost from the SiGeC layer (circles) or the entire sample (squares) of structures A and B, (a) and (b) respectively, after annealing in either oxygen (hollow symbols) or nitrogen (solid symbols) ambient at 850°C. Total carbon in the as-grown SiGeC layers of structure A and B were $\sim 3.5 \times 10^{14} \text{ cm}^{-2}$ and $4.5 \times 10^{14} \text{ cm}^{-2}$, respectively.

Using the model for interstitial injection of the previous chapter, the interstitial flux into the sample is calculated as:

$$J_I = -D_I \frac{dI}{dx} = n_{surf} \times \frac{D_I I^*}{\Delta x} \quad (6.2)$$

where, n_{surf} is the ratio of the interstitial surface concentration to the bulk interstitial concentration (I/I^*), $D_I I^*$ is the interstitial transport product measured by metal tracer diffusion [9, 10], and Δx is the depth of the SiGeC layer. The total number of injected interstitials after oxidation is calculated as the time integrated flux and is compared to

the extra carbon that leaves the SiGeC layer due to oxidation for structures A (dotted line) and B (dashed), (Fig. 6.7).

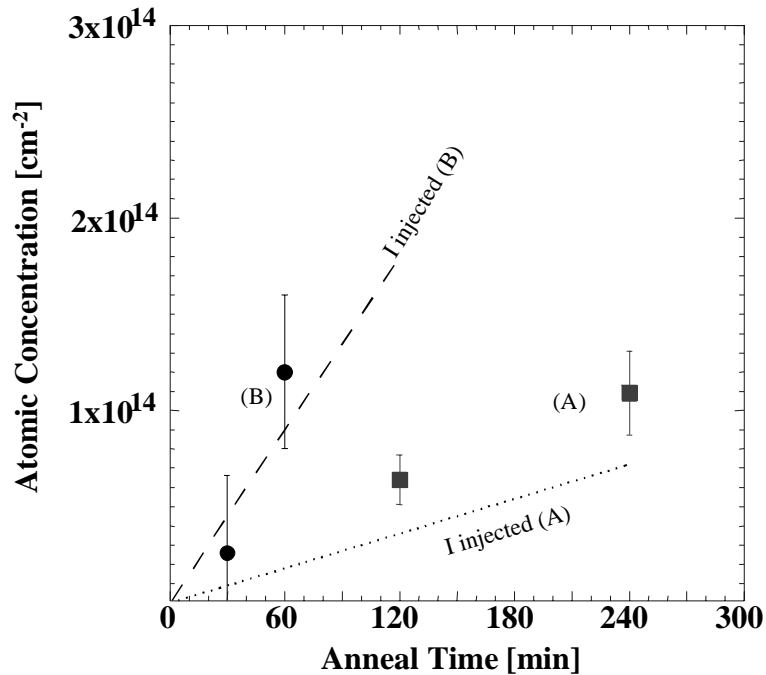


Figure 6.7 Summary of oxidation enhanced carbon loss from the SiGeC layer, i.e. the difference of carbon lost between oxidation and nitrogen anneals, for structures A (squares) and B (circles). The number of injected interstitial silicon atoms after oxidation is also calculated for structures A (dotted line) and B (dashed line) for comparison.

The calculated number of interstitials injected into structure B is nearly identical to the extra carbon that diffuse out of the SiGeC layer due to oxidation, Fig. 6.7, after 30 and 60 minutes annealing (the value for 60 minutes was interpolated from the nitrogen data in Fig. 6.5 (a)). Note: the calculated number of interstitials injected relied solely on the validity of eq'n. 2, the $D_T I^*$ product from the literature, and the

depth of the layer. There were no adjustable variables available in this calculation. After 120 minutes the measured oxidation enhancement saturates and diverges from the calculated interstitial injection because the carbon, by this time, is entirely removed from the SiGeC layer. To summarize the results for structure B after oxidation, a silicon self-interstitial injected at the surface during oxidation reacts with the substitutional carbon in the SiGeC layer (previous chapter). The reaction removes substitutional carbon from the SiGeC layer and the carbon removed from the layer agrees quantitatively one-to-one with the number of injected interstitials. The end-product of the reaction leaves no detectable carbon behind in the form of carbon precipitation or carbon clusters. We conclude therefore that the carbon reaction with the excess injected self-interstitials is a “kick-out” like diffusion reaction (eq’n. 6.1) and the “sink” effect is not due to an immobile carbon trap.

Because the interstitial injection rate depends inversely on the depth of the SiGeC layer (eq’n. 2), the number of interstitials injected into structure A is less than B. Therefore the oxidation-enhanced carbon diffusion out of the SiGeC is slower (Fig. 6.7) in A (thick case) than in B (thin case). However, the number of extra carbon atoms removed from the SiGeC layer in structure B due to oxidation is greater than the number of interstitials injected into structure A. Assuming carbon diffusion is described by the reactions in eq’n. 1, one interstitial migrating into the SiGeC layer can be responsible for the production of only a single mobile carbon. However, one additional interstitial injected at the surface may be responsible for the removal of

multiple carbon atoms from the SiGeC layer, if the mobile carbon that leaves the SiGeC layer, and then goes back to again occupy a substitutional site, this “kicking” out a silicon self-interstitial atom, in the surrounding silicon near the SiGeC. The interstitial is then free to migrate back to the SiGeC layer and remove a second carbon from the SiGeC layer effectively recycling the interstitial (Fig. 6.7 & 6.8). This increases the ratio of extra carbon removed to injected interstitials above unity. The amount of recycling will depend on the carbon layer proximity to the surface, because some mobile carbon will escape the sample via the surface, thus removing the interstitial completely from the sample. As is indeed observed, the ratio of removed carbon to injected interstitials is 1:1 for the SiGeC layer closest to the surface and only is greater than one for the deeper SiGeC layer. The observed 1:1 ratio in structure B also indicates that the carbon does not immediately form immobile clusters with the injected interstitials in the SiGeC (i.e. C_i-C_s , C_i-I or C_i-I_X), which have been observed in silicon, for example, after electron radiation [6]. They may eventually result, but only if the C_i is not rapidly drawn out of the layer or sample first. A second experiment using boron marker layers to monitor the local interstitial concentration was done to further examine the recycling effect.

supplied from the surface or bulk regions, therefore, the interior silicon region will begin to be depleted of self-interstitials. The steady-state concentration will depend on a detailed balance between the self-interstitial generation rate and the rate at which the self-interstitials are lost to the surrounding carbon. This novel structure offers a method to probe the generation rate of silicon self-interstitials. It will be shown that the generation of self-interstitials due to recycling is much faster than the bulk generation rate of silicon self-interstitials.

A structure with four boron marker layers separated by two SiGeC layers was grown to examine the effect on the boron diffusivity in a silicon region isolated from the bulk and surface supplies of silicon self-interstitials by two surrounding SiGeC interstitial sinks (Fig. 6.9). The layers were grown as described section 6.2 and annealed in nitrogen or oxygen ambient at 850°C for 30-240 minutes. As-grown and

135 nm, i-Si
25 nm, 10^{19} cm ⁻³ boron
135 nm, i-Si
25 nm, Si _{0.795} Ge _{0.2} C _{0.005}
135 nm, i-Si
25 nm, 10^{19} cm ⁻³ boron
50 nm, i-Si
25 nm, 10^{19} cm ⁻³ boron
100 nm, i-Si
25 nm, Si _{0.795} Ge _{0.2} C _{0.005}
150 nm, i-Si
25 nm, 10^{19} cm ⁻³ boron
Si-substrate

Figure 6.9 Schematic cross section of the double SiGeC layer with boron marker layers to examine the interstitial concentration in silicon between two interstitial sinks.

120 minute nitrogen annealed boron and carbon profiles, Fig. 6.10 (a), show broadening of both the carbon and boron layers between the two SiGeC layers. A single fit describing the boron diffusivity in both markers in between the SiGeC layers for each time after annealing in oxygen or nitrogen ambient are compared to those found in the pure silicon sample grown on the same day and annealed in identical conditions, Fig. 6.10 (b). The boron diffusivity between the SiGeC layers is enhanced in both the oxygen- and nitrogen- annealed cases after 30 minutes nearly identical amounts.

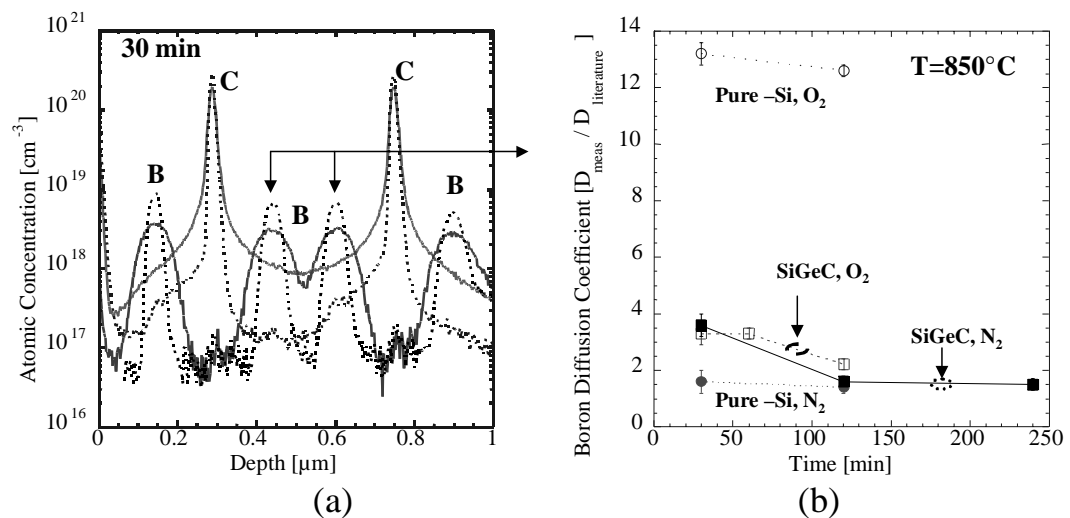


Figure 6.10 (a) boron and carbon concentration profiles from the double buried SiGeC layer sample before and after annealing at 850°C in nitrogen ambient for 120 minutes and (b) the measured diffusivity of the boron between the SiGeC layers compared to that found in pure silicon after annealing in oxygen or nitrogen ambient.

The boron diffusivity becomes and remains indistinguishable from the nitrogen annealed boron diffusivity in the pure silicon samples after 120 minutes. We con-

clude, therefore, that the interstitial concentration between the SiGeC layers is relatively uniform and not depleted by the nearby SiGeC interstitial sinks despite that most of the interstitials have had time to diffuse to and react with the carbon (a conservative estimate of the diffusion length of the self-interstitial is ~ 800 nm for the case of $[C] \sim 10^{18} \text{ cm}^{-3}$ [11]). Because additional interstitials are prohibited from coming from either the surface or bulk through the SiGeC layer, the silicon interstitials that diffuse and react with the carbon in the SiGeC layer must somehow be generated in the region between the SiGeC layers. There remains the question as to why the diffusion and thus the interstitial concentration is enhanced in the SiGeC sample for short times during annealing in either nitrogen or oxygen ambient. It will be shown in section 6.5 that the generation mechanism for additional interstitials can be explained by the recycling mechanism.

Frenkel pair recombination is believed to play a significant role in the removal of point-defects immediately after ion-implantation [12], therefore a possible source of interstitial generation might be the reverse reaction in the case of interstitial under-saturation:



Assuming a constant generation rate of interstitials, a fixed vacancy concentration, and a vacancy-interstitial recombination rate proportional to the product of the interstitial and vacancy concentrations, a recombination/generation rate of the interstitials can be defined by a single effective lifetime of the interstitial, τ_{eff} :

$$U = \frac{I - I^*}{\tau_{eff}} \quad (6.4)$$

where U is the recombination/generation rate. A characteristic diffusion length of the interstitial,

$$L_I = \sqrt{D_I \cdot \tau_{eff}} \quad (6.5)$$

describes the exponential decay of an interstitial profile during steady-state diffusion. A minimum bound on the interstitial diffusion length before recombination with a vacancy for 850°C is 700 nm, inferred from the lack of exponential decay in the interstitial profiles between the surface and the SiGeC layer during oxidation in the previous chapter, Fig. 5.7 (c). However, the uniform intrinsic boron diffusivity observed between the two SiGeC layers indicates that the interstitial concentration returns to the intrinsic interstitial concentration in a distance smaller than 100 nm, a much shorter depth than the minimum recombination decay length. This rules out a simple interstitial generation mechanism like that described by eq'n. 4.

As discussed in section 6.3 another possible source of interstitials is from the reverse reaction of the kick-out reaction. The mobile carbon interstitial diffuses out of the substitutional carbon layer and decays after an average diffusion lifetime to a substitutional site, which in turn releases an interstitial. In the following section the carbon diffusion was modeled, based on the kick-out mechanism, to illustrate

quantitatively how the kick-out and reverse reaction fit together to reasonably reproduce the experimental observations.

6.5 Simulations

As discussed earlier interstitial diffusing dopants, self-interstitials, and carbon are all reported to diffuse slower in the presence of supersaturated carbon concentrations. An initial proposal to explain this effect was the local undersaturation of the interstitial concentration due to carbon complexing, i.e. trapping, the silicon interstitials. However, this proposal does not explain the diffusion between the SiGeC layers nor does it explain how a single interstitial may be responsible for the removal of more than a single substitutional carbon atom as was discussed in section 6.3. Alternatively, the undersaturation of interstitials in the carbon rich regions has also been successfully explained by the rapid reaction of the substitutional carbon with the local silicon interstitials ultimately depleting the region of interstitials faster than can be supplied from the surrounding region [13, 14]. To test this hypothesis the proposed model for carbon in silicon was simulated and compared to the experiment in the previous section.

6.5.1 Model of carbon diffusion

Carbon diffusion is proposed to be a result of the parallel “kick-out” (KO) and Frank-Turnbull (FT) mechanism that both lead to the formation of the mobile interstitial-carbon defect when substitutional carbon reacts with silicon point-defects:



where V is a silicon vacancy. Although the FT mechanism is energetically unfavorable, the amount of carbon diffusion observed in previous experiments could not be explained only by the KO mechanism [14]. Reports of enhanced antimony and germanium diffusion in the presence of carbon supersaturated silicon [15], which diffuse via a vacancy-assisted mechanism, have led to the suggestion of this second vacancy producing mechanism (FT) to explain the source of the extra carbon diffusion. These two reactions lead to the following linked partial differential equations that describe the carbon and point defect reactions and subsequent diffusion:

$$\frac{\partial C_s}{\partial t} = -R_{C_{SI}} + R_{C_{IV}} \quad (6.8)$$

$$\frac{\partial C_i}{\partial t} = D_{C_i} \nabla C_i + R_{C_{SI}} - R_{C_{IV}} \quad (6.9)$$

$$\frac{\partial I}{\partial t} = D_I \nabla I - R_{C_{SI}} \quad (6.10)$$

$$\frac{\partial V}{\partial t} = D_V \nabla V - R_{C_{IV}} \quad (6.11)$$

where $R_{C_{SI}}$ is the reaction rate of the substitutional carbon with the silicon self-interstitial to form the interstitial-carbon and $R_{C_{IV}}$ is the reaction rate of the interstitial-carbon with the silicon vacancy to form a substitutional carbon. It is assumed that only the

interstitial form of carbon is mobile and that the dominant mobile species is neutral. The subsequent effect of local electric fields and extrinsic carrier concentrations on the carbon diffusion is, therefore, neglected. This formulation was first proposed by Scholz et al for carbon diffusion in silicon [14]. Ruecker et al applied the same model, neglecting the contribution of germanium point defects to the carbon diffusion, and relatively successfully fit carbon diffusion out of SiGe layers [16]. The reaction rates are the sum of the forward and reverse reactions:

$$R_{Cst} = K_{fl} C_s I - K_{rl} C_i \quad (6.12)$$

$$R_{Civ} = K_{fv} C_i V - K_{rv} C_s \quad (6.13)$$

where K_{fl} and K_{rl} are the forward and reverse rate constants for the interstitial kick-out mechanism and K_{fv} and K_{rv} are the forward and reverse rate constants for the vacancy Frank-Turnbull mechanism. These rate constants may be estimated by assuming a diffusion limited reaction, i.e. from the kinetic theory of non-interacting particles:

$$K_{fl} = 4 \cdot \pi \cdot a_r \cdot (D_I + D_{Cs}) \quad (6.14)$$

$$K_{fv} = 4 \cdot \pi \cdot a_r \cdot (D_V + D_{Ci}) \quad (6.15)$$

where a_r is the radius of the reaction cross section. Assuming no long-range interaction, the cross section radius is on the order of an atomic radii. The reverse reactions

are obtained assuming detailed balance in equilibrium and using measured equilibrium quantities:

$$K_{rI} = K_{fI} \cdot I \cdot \left(\frac{C_s}{C_i} \right)^{eq} \cong 4 \cdot \pi \cdot a_r \cdot (D_I I) \cdot \left(\frac{C_s}{C_i} \right)^{eq} \quad (6.16)$$

$$K_{rV} = K_{fV} \cdot V \cdot \left(\frac{C_i}{C_s} \right)^{eq} = 4 \cdot \pi \cdot a_r \cdot (D_V + D_{C_i}) \cdot V \cdot \left(\frac{C_i}{C_s} \right)^{eq} \quad (6.17)$$

The ratio of $\left(\frac{C_s}{C_i} \right)^{eq}$ is estimated from the ratio of measured diffusivities at equilibrium:

$$\left(\frac{C_s}{C_i} \right)^{eq} = \frac{D_{C_i}}{D_{C_s}} = \frac{0.44 \cdot \exp(-0.87/kT)[cm^2 s^{-1}]}{1.9 \cdot \exp(-3.1/kT)[cm^2 s^{-1}]} \gg 1 \quad (6.18)$$

It can be shown that the total carbon out-diffusion from the SiGeC layer due to the KO mechanism alone is dependent only on the $D_I I$ transport product [13, 17, 18], i.e. it is independent of K_{fI} for a set value of $D_I I$, but does depend on K_{rV} , which determines the FT contribution to the carbon flux. K_{rV} is not well known because neither the intrinsic vacancy concentration or diffusivity are well established, therefore, it is used as the single adjustable parameter to fit the experiment. The critical parameters necessary for this model are given below.

Table 6.1. Model's variables and their references

Variable	Value	Reference
I^*	$2.9 \times 10^{24} \exp(-3.18 \text{ eV/kT}) [\text{cm}^{-3}]$	[10]
D_I	$51 \exp(-1.77 \text{ eV/kT}) [\text{cm}^2 \text{ s}^{-1}]$	[10]
V^*	$1.71 \times 10^{24} \exp(-2.0 \text{ eV/kT}) [\text{cm}^{-3}]$	[18]
D_V	$0.03 \exp(-1.8 \text{ eV/kT}) [\text{cm}^2 \text{ s}^{-1}]$	[18]
C_s	$4 \times 10^{24} \exp(-2.3 \text{ eV/kT}) [\text{cm}^{-3}]$	[6]
D_{C_s}	$0.95 \exp(-3.04 \text{ eV/kT}) [\text{cm}^2 \text{ s}^{-1}]$	[6]
D_{C_i}	$0.44 \exp(-0.87 \text{ eV/kT}) [\text{cm}^2 \text{ s}^{-1}]$	[6]

6.5.2 Modelling of carbon diffusion profiles

Because the structure from the previous section displays most of the critical observations, i.e. an interstitial sink in the carbon rich region while not depleting the interstitial population between the SiGeC layers, it is used to illustrate the predictions of this diffusion model. The time evolution of the diffused carbon profiles due to the combined KO and FT mechanisms were simulated using as-grown carbon profiles obtained from SIMS as the initial condition for the carbon concentration. The as-grown carbon profiles was assumed entirely substitutional. The interstitial and vacancy concentrations at the surfaces were set equal to the intrinsic concentration, while the surface acted as a perfect sink for carbon, i.e. carbon diffusing to the surface is removed from the sample (see section 6.2) for the nitrogen anneal case. For the oxi-

dation case, the same boundary conditions were used except that the surface interstitial concentration was set to the enhanced value determined in the previous chapter, i.e. 12.7 times the intrinsic concentration I^* . All other critical parameters are listed in table 6.1. The simultaneous one-dimensional partial differential equations were numerically solved by PROPHET [19]. The carbon profiles after annealing at 850°C for 30 minutes in nitrogen are shown compared to the simulation both overlaid on the as-grown carbon profile (initial condition). In this case, when $K_{rV} \sim 10^{-5}$ sec., enough additional carbon outdiffusion is created to agree well with the experimentally obtained carbon profiles, Fig 6.11.

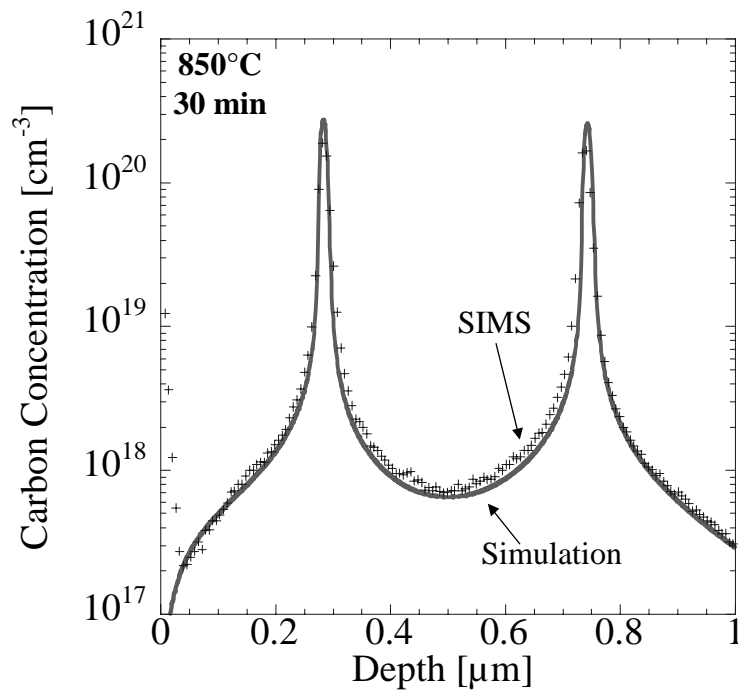


Figure 6.11 Carbon concentration profiles from the double buried SiGeC layer sample after annealing at 850°C in nitrogen ambient for 30 minutes overlaid on the profile calculated using the combined kick-out and Frank-Turnbull mechanism.

The calculated interstitial carbon and silicon interstitial concentrations are displayed with the substitutional carbon profile for the annealing in nitrogen or oxygen ambient for 30 minutes, (Fig 6.12 (a) and (b)) respectively. The interstitial concentration is depressed to less than a tenth of the intrinsic interstitial concentration ($1.5 \times 10^{10} \text{ cm}^{-3}$) in the carbon rich region (Fig. 6.12 (a)) during nitrogen anneal. (Note: the self-interstitial concentration is not well known. Estimates range over 4 orders of magnitude. The intrinsic self-interstitial concentration used in these simulations were those

suggested by Bracht et al.) The silicon self-interstitial concentration remains near its intrinsic concentration (when carbon is present) only as long as self-interstitials diffuse in from the bulk and surface rapidly enough to supply the substitutional carbon reaction with the silicon-self-interstitial. This is true when the substitutional carbon concentration is below the solid solubility concentration. In this case, however, the substitutional carbon concentration is orders of magnitude greater than the typical solid-solubility concentration. The high substitutional carbon concentration produces an unusually high rate of self-interstitial consumption (eq'n. 6.12) that can not be sustained by the transport capacity of the surrounding self-interstitials, which results in an undersaturation of silicon self-interstitials in the high substitutional carbon region.

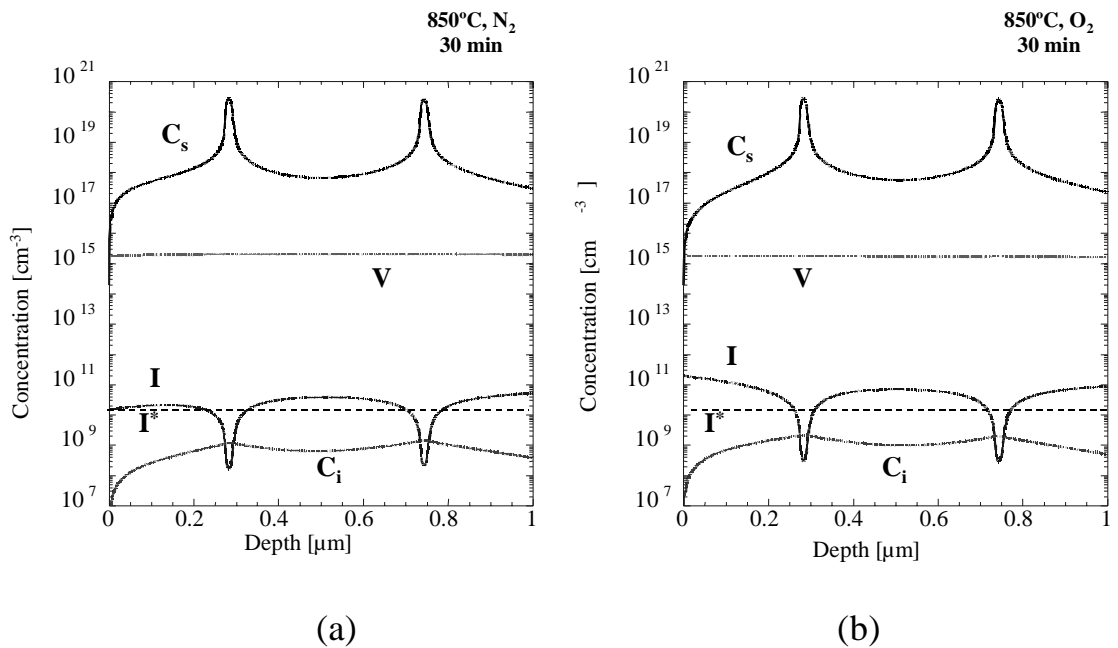


Figure 6.12 Simulated substitutional, interstitial carbon and interstitial silicon profiles after 30 minutes of annealing at 850°C in (a) nitrogen or (b) oxygen ambient.

In the previous chapter it was found that oxidation increases the surface concentration of silicon self-interstitials. Interstitials are injected into the bulk from the surface due to the resulting self-interstitial gradient. The increased flow of self-interstitials into the SiGeC layer does not, however, substantially increase the self-interstitial concentration (above the self-interstitial concentration calculated for the nitrogen anneal case) in the SiGeC layer 300 nm below the surface. The model predicts, therefore, that all injected interstitials react with the substitutional carbon at the SiGeC layer agreeing with experiment. Furthermore, since the self-interstitials diffuse quickly from the surface to the buried SiGeC layer (compared to the substitutional carbon) the self-interstitial concentration above the SiGeC layer reaches an approximately steady-state condition. The simulated interstitial profile, therefore, rapidly becomes linear, which is consistent with experiment (chap. 5). The simulated “kick-out” reaction, therefore, is sufficient to explain the experimentally observed “sink” effect observed in chapter 5.

The interstitial concentration between the two SiGeC layers in both annealing conditions rapidly increases to 3-4 times the intrinsic interstitial concentration ($1.5 \times 10^{10} \text{ cm}^{-3}$). The carbon diffusion simulation does not predict that the self-interstitial concentration between the two SiGeC layers is depleted although all self-interstitials between the carbon layers are well within the calculated intrinsic (no carbon) self-interstitial diffusion length for this annealing condition ($340 \mu\text{m}$) [10]. The self-

interstitials have had time to diffuse to and react with the carbon in the surrounding SiGeC layers. The simulation, therefore, shows that the self-interstitials consumed at the carbon layer, from between the SiGeC layers, are somehow resupplied. Only one reaction in the simulation produces self-interstitials, the reverse kick-out mechanism (eq'n. 6.6). The simulation, therefore, shows that every self-interstitial that migrates to and is consumed at the SiGeC layer is resupplied by the decay of an interstitial carbon.

Not only is the calculated self-interstitial concentration not depleted by the surrounding SiGeC layers, but the simulation predicts an increase above the intrinsic concentration. More self-interstitials are released through the reverse KO reaction of interstitial-carbon in the silicon region than self-interstitials are consumed by the SiGeC layer. The increase in self-interstitial concentration above the intrinsic concentration requires an additional source of self-interstitial generation. Since the model produces self-interstitials only through the reverse KO reaction, the additional self-interstitials are produced by another source of interstitial-carbon. The second source of interstitial-carbon and increase of self-interstitial concentration above the intrinsic concentration, in the calculation, is from the contribution of the Frank-Turnbull mechanism (eq'n. 6.7). As discussed in the previous sections (the experiment), the boron diffusivity was depressed in the carbon rich regions but was found to be enhanced by 3-4 times between the SiGeC layers during annealing in nitrogen ambient. The enhanced boron diffusivity between the SiGeC layers, which is an experimental mea-

sure of the enhanced self-interstitial concentration, agrees relatively well with the calculation self-interstitial enhancement.

During oxidation the self-interstitial concentration between the two SiGeC layers is increased above that calculated during nitrogen anneal. Some of the extra interstitial-carbon created by the extra injected self-interstitials migrate into the region between the two SiGeC layers instead of leaving the sample. Most of these extra interstitial-carbon become substitutional carbon releasing self-interstitials, which increases the self-interstitial concentration above that in the nitrogen anneal case between the two SiGeC layers. The calculation reproduces qualitatively the recycling effect proposed in section 6.3, i.e. injected self-interstitials during oxidation are recycled in the silicon bulk. However, little difference is observed between the measured (experiment) boron diffusivities between the SiGeC layers during annealing in nitrogen or oxygen ambient (Fig. 6.10). The calculation, therefore, overestimates the number of self-interstitials that are recycled during oxidation for this structure.

In section 6.3 the recycling effect was suppressed in the oxidized sample with the SiGeC layer buried only 60 nm below the silicon surface. To better understand what determines the fraction of injected self-interstitials that are recycled a second simulation of the carbon diffusion in this structure was performed. Using the same model parameters as in the previous calculation, the self-interstitial, vacancy, substitutional- and interstitial carbon concentration profiles after 30 minutes of oxidation at 850°C were simulated (6.13 (a)). From these profiles, the interstitial-carbon (solid

line), vacancy (dashed line) and silicon self-interstitial (dotted line) currents were calculated from their respective diffusivities and simulated concentration gradients (Fig. 6.13 (b)).

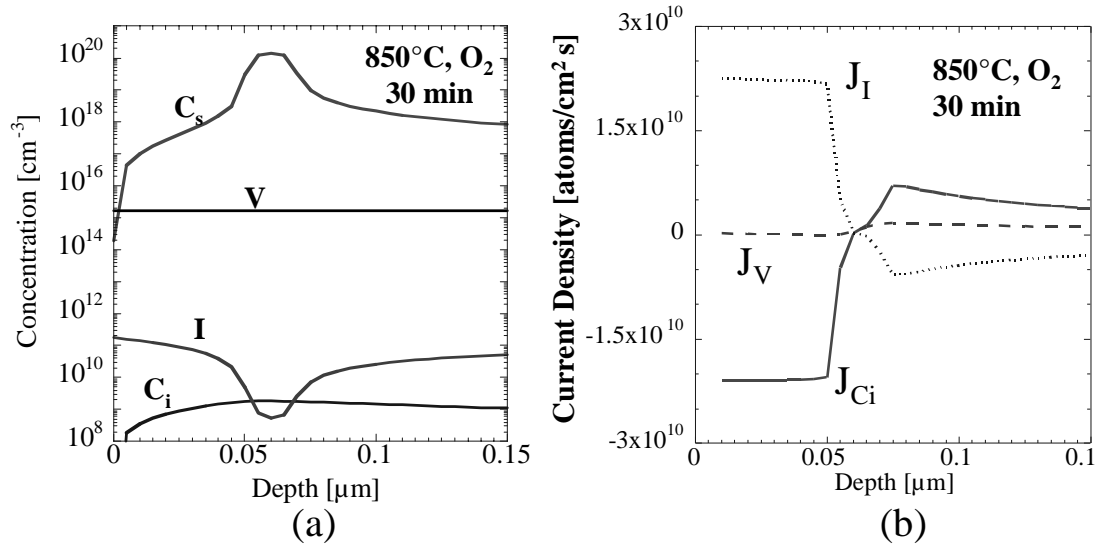


Figure 6.13 (a) Simulated substitutional-, interstitial-carbon, self-interstitial and vacancy concentration profiles after 30 minutes oxidation at 850°C for structure B (SiGeC layer buried 60 nm below the surface, Fig 6.1 (b)) and (b) diffusion currents calculated from simulated interstitial-carbon, silicon interstitial, and vacancy profiles.

First consider the interstitial-carbon and self-interstitial currents that decrease from the SiGeC layer into the silicon bulk (Fig. 6.13 (b)). The decay of interstitial-carbon current with increasing depth into the bulk is a consequence of the interstitial-carbon decaying to substitutional carbon and self-interstitials. This decay feeds the current of silicon interstitials back towards the carbon layer. The currents are almost exactly balanced. The self-interstitial defect effectively runs a circuit flowing towards the carbon layer as a free self-interstitial and then returning to the silicon bulk, trans-

ported as an out-going interstitial-carbon, until it decays and releases the self-interstitial.

Now consider the currents in and out of the surface. The self-interstitial and carbon-interstitial currents are nearly constant (indicating linear concentration gradients) and are considerably higher on the surface side of the SiGeC layer than on the bulk side. The higher currents are created by the extra self-interstitials injected into the silicon due to oxidation. After 30 minutes of oxidation, carbon has had time to diffuse out the surface. As discussed earlier the surface is treated as a perfect sink for carbon. The surface, therefore, creates an asymmetry in the interstitial-carbon profile, which is steeper on the surface side (Fig. 6.12 (a)). The concentration gradient of interstitial-carbon determines the interstitial-carbon current and the steeper concentration gradient on the surface side produces a greater current towards the surface than into the bulk. The unequal currents lead to a disproportionate number of interstitial-carbon that leave both the SiGeC layer and the sample compared to the interstitial-carbon that migrates into the bulk.

The calculation shows a nearly equal current of self-interstitials into the SiGeC layer as the interstitial-carbon current out the surface at this oxidation time. This indicates that most self-interstitials injected by oxidation are carried out of the sample as interstitial-carbon. The difference in currents is $\sim 1 \times 10^9 \text{ cm}^{-2} \text{ s}^{-1}$ (self-interstitial current is slightly greater than the interstitial-carbon current) indicating that less than 5% of the injected interstitials are recycled in the bulk after reacting with the SiGeC layer

rather than are removed from the sample as interstitial-carbon flowing out the surface. The model illustrates how a simple KO mechanism can lead to the disproportionate loss of carbon from the SiGeC layer out the surface compared to the carbon that diffuses into the bulk (i.e. almost every carbon “kicked-out” also leaves the sample as observed in section 6.3 (Fig. 6.6 and 6.7)).

To summarize, the surface is considered a “sink” for interstitial-carbon. As the SiGeC layer approaches the surface the interstitial-carbon gradient becomes much steeper towards the surface than into the bulk. This causes a disproportionate amount of interstitial-carbon to leave the SiGeC layer towards the surface compared to that into the bulk. The recycling of self-interstitials depends on migration of interstitial-carbon into the bulk followed by the reverse KO reaction to release a self-interstitial in the bulk. As the carbon layer approaches the surface, the recycling effect is suppressed because a greater fraction of the interstitial-carbon is driven out the sample than goes into the bulk. The overestimated recycling calculated in the double SiGeC layer structure, therefore, is due to an incorrect estimate of the interstitial-carbon gradient into the bulk over the 30 minute oxidation time compared to that towards the surface. The disagreement may simply be due to error in the choice of parameters within this model like an underestimate of the interstitial-carbon diffusivity, which has only been measured at low temperatures (below room temperature) [6].

To conclude, the diffusion model proposed, based on a simple kinetic theory and using literature values for all critical parameters except one, illustrates how the

combined KO and FT mechanisms lead to very similar quantitative behavior as that observed in experiment. The self-interstitial concentration is suppressed when the carbon concentration is raised above the solid-solubility, which would explain the reduced boron diffusivity observed in SiGeC (chapter 3). The carbon oversaturated silicon acts as a self-interstitial sink for injected self-interstitials (chapter 4 and 5) but does not deplete the surrounding regions of self-interstitials because of the recycling effect (chapter 6). Further work is required to test the validity of this model for different annealing conditions and structures.

6.6 Summary

In conclusion, carbon out-diffusion from $\text{Si}_{0.7865}\text{Ge}_{0.21}\text{C}_{0.0035}$ layers has been examined after annealing in nitrogen or oxygen ambient at 850°C. Carbon is found to diffuse out the surface and the carbon diffusion from the SiGeC layer is enhanced by oxidation. The extra number of substitutional carbon removed from the SiGeC layer is explained by a “kick-out”-like reaction with the injected interstitials during oxidation. The carbon out-diffusion from 25 nm thick SiGeC layer is found to be the dominant mechanism of loss of substitutional carbon (as opposed to carbon clusters or precipitation) in all annealing conditions examined for layers with silicon caps less than or equal to 300 nm. Finally, carbon diffusion for concentrations above solid-solubility has been modeled to illustrate how the combined KO and FT mechanisms can lead to the same behavior as that observed experimentally. The simulations

support the conclusion that the self-interstitial reaction with the substitutional carbon is “kick-out”-like and that the reaction mediates the substitutional carbon diffusion.

6.7 References

- [1] J. W. Strane, H. J. Stein, S. R. Lee, S. T. Picraux, J. K. Watanabe, and J. W. Mayer, *J. Appl. Phys.*, vol. 76, pp. 3656, 1994.
- [2] P. Warren, J. Mi, F. Overney, and M. Dutoit, *J. of Crystal Growth*, vol. 157, pp. 414-419, 1995.
- [3] J. C. Sturm, P. V. Schwartz, E. J. Prinz, and H. Manoharan, *J. Vac. Sci. Tech. B*, vol. 9, pp. 2011, 1991.
- [4] D. De Salvador, M. Petrovich, M. Berti, F. Romanato, E. Napolitani, A. Drigo, J. Stangl, S. Zerlauth, M. Muehlberger, F. Schaeffler, G. Bauer, and P. C. Kelires, *Phys. Rev. B*, vol. 61, pp. 13005, 2000.
- [5] L. A. Ladd and J. P. Kalejs, presented at Oxygen, Carbon, Hydrogen, and Nitrogen in Crystalline Silicon, 1986.
- [6] G. Davies and R. C. Newman, "Carbon in monocrystalline Silicon," in *Handbook on Semiconductors*, T. S. Moss, Ed., 1994, pp. 1558.
- [7] L. V. Kulik, D. A. Hits, M. W. Dashiell, and J. Kolodzey, *Appl. Phys. Lett.*, vol. 72, pp. 1972, 1998.
- [8] P. Werner, H.-J. Gossmann, D. C. Jacobson, and U. Goesele, *Appl. Phys. Lett.*, vol. 73, pp. 2465, 1998.
- [9] M. S. Carroll and J. C. Sturm, "Quantitative measurement of the interstitial flux and surface super-saturation during oxidation of silicon," presented at Silicon Front-End Processing-Physics and Technology of Dopant-Defect Interactions II, San Francisco, 2000.
- [10] H. Bracht, N. A. Stolwijk, and H. Mehrer, *Phys. Rev. B.*, vol. 52, pp. 16542, 1995.
- [11] H.-J. Gossmann, C. S. Rafferty, H. S. Luftmann, F. C. Unterwald, T. Boone, and J. M. Poate, "Oxidation enhanced diffusion in Si B-doping superlattices and Si self-interstitial diffusivities," *Appl. Phys. Lett.*, vol. 63, pp. 639, 1993.
- [12] P. A. Stolk, H.-J. Gossmann, D. J. Eaglesham, D. C. Jacobson, C. S. Rafferty, G. H. Gilmer, M. Jaraiz, J. M. Poate, H. S. Luftmann, and T. E. Haynes, "Physical mechanisms of transient enhanced dopant diffusion in ion-implanted silicon," *J. Appl. Phys.*, vol. 81, pp. 6031, 1997.
- [13] R. Scholz, U. Goesele, J. Y. Huh, and T. Y. Tan, *Appl. Phys. Lett.*, vol. 72, pp. 2, 1998.
- [14] R. F. Scholz, P. Werner, U. Goesele, and T. Y. Tan, *Appl. Phys. Lett.*, vol. 74, pp. 392, 1999.
- [15] H. Ruecker, B. Heinemann, D. Bolze, D. Knoll, D. Krueger, R. Kurps, H. J. Osten, P. Schley, B. Tillack, and P. Zaumseil, presented at Technical Digest : International Electron Device Meeting, San Francisco, 1999.

- [16] H. Ruecker and B. Heinemann, "Tailoring dopant diffusion for advanced SiGe:C heterojunction bipolar transistors," *Solid-State Elec.*, vol. 44, pp. 783, 2000.
- [17] A. Ural, P. B. Griffin, and J. D. Plummer, "Self-Diffusion in Silicon: Similarity between the Properties of Native Point Defects," *Phys. Rev. Lett.*, vol. 83, pp. 3454, 1999.
- [18] H. Bracht, E. E. Haller, and R. Clark-Phelps, "Silicon Self-Diffusion in Isotop Heterostructures," *Phys. Rev. Lett.*, vol. 81, pp. 393, 1998.
- [19] M. R. Pinto, D. M. Boulin, C. S. Rafferty, R. K. Smith, W. M. Coughran, I. C. Kizilyalli, and M. J. Thoma, *Tech. Digest IEDM*, pp. 923, 1992.
- [20] Fahey, P. B. Griffin, and J. D. Plummer, *Rev. Mod. Phys.*, vol. 61, pp. 289, 1989.
- [21] H. Ruecker, B. Heinemann, W. Roepke, R. Kurps, D. Krueger, G. Lippert, and H. J. Osten, "Suppressed diffusion of boron and carbon in carbon-rich silicon," *Appl. Phys. Lett.*, vol. 73, pp. 1682, 1998.

Low-Temperature Preparation of Oxygen- and Carbon-Free Silicon and Silicon-Germanium Surfaces for Silicon and Silicon-Germanium Epitaxial Growth by Rapid Thermal Chemical Vapor Deposition

7.1 Introduction

Small thermal budgets for silicon processing are increasingly demanded by ultra-large scale integration (ULSI) technologies for various reasons such as the control of dopant diffusion. The desire to integrate SiGe based heterojunction bipolar transistor (HBT) technologies with silicon complementary metal-oxide-semiconductor (CMOS) technology has introduced a new demand for low thermal budget Si/SiGe epitaxy [1]. It is now established that high quality silicon epitaxy can be grown by chemical vapor deposition (CVD) at relatively low temperatures ranging between 500-800°C, despite these temperatures being too low to desorb contaminants rapidly enough, such as oxygen, from the surface of the silicon during the silicon epitaxy [2,3]. The low-temperature CVD growth of silicon is achieved by relying on either low partial pressures of contamination such as water vapor or hydrogen passivation to reduce the sticking coefficient of the contamination. However, an initial clean substrate surface is necessary for high-quality structures. Traditionally, CVD methods have relied on high temperature in-situ cleaning steps such as hydrogen pre-bakes at 1000°C. Such

temperatures often are unacceptable if there are already dopant device profiles in the substrate.

Several groups have reported oxygen- and carbon-free surfaces for subsequent epitaxy prepared by in situ hydrogen pre-bakes between 760-850°C after an ex-situ wet clean. However, there is special emphasis in these reports on ultra high vacuum requirements and dry-pumped loading systems, and all of the reported cleaning procedures depend on wet chemical preparation that are not compatible with the exposed SiGe surfaces. In UHVCVD, no cleaning step at all beyond a wet ex-situ clean (e.g. an HF dip) is required for high quality epitaxy at 760°C, but often residual carbon and oxygen contamination still are found at the interface [4]. In this chapter we study the dependence of surface quality on ex-situ wet cleaning and in-situ hydrogen baking steps compatible with SiGe surfaces, without the need for UHV in the deposition chamber. Secondary ion mass spectroscopy (SIMS) of buried interfaces and photoluminescence (PL) from thin buried SiGe layers are used to measure contamination. We present a low pressure cleaning technique compatible with SiGe surfaces that reduces oxygen and carbon contamination below the detection limits of SIMS for a rapid thermal chemical vapor deposition system (RTCVD) using only conventional rotary vane pumps.

This chapter is divided into four parts. First the standard procedure for epitaxial growth and interface characterization are described. Second, ex-situ wet cleaning steps were examined. The third section focuses on contamination introduced by the

reactor and load lock. Finally the effect of in-situ bakes before growth is examined in Section 4.

7.2. Standard Growth and Characterization Procedures

7.2.1 Cleaning and Growth Procedures

Standard growth procedures are now described. First the wafers are chemically cleaned, beginning with the removal of the native oxide from p-type wafers (5-50 ohm-cm) using a ~5 min dilute HF dip (1:100 HF(49%):DI). The surface was then chemically oxidized by immersing the wafer in $\text{H}_2\text{SO}_4:\text{H}_2\text{O}_2(30\%)1:1$ at 70°C for 20 min. The oxide was then removed using an HF- based etch which leaves the surface hydrogen terminated [5,6]. Unless otherwise noted, the HF(49%) to DI ratio for this last step was 1:1000. After the last HF step, the wafer was not rinsed in DI water, except when noted. The DI water resistivity was ~18 Megaohm-cm, the total organic content (TOC) was <50 ppb, and the laboratory temperature was between $21\text{-}24^\circ\text{C}$ with a relative humidity below 50%. All chemicals were obtained from J. T. Baker and were “CMOS electronic” grade. No precaution was taken to avoid dissolved oxygen in the DI water [7].

Following the wet clean the wafer is placed on a quartz stand in the load-lock of the growth reactor, which is evacuated to ~50 mtorr by a standard rotary-vane mechanical pump. Three or four pump-purge cycles on the load-lock are performed before the wafer is introduced to the growth chamber. The pump-purge cycle consists of filling

the load-lock to ~ 1 torr with dry nitrogen before evacuation, and one cycle takes an average of approximately 5 minutes. The wafer is then transferred to the growth chamber, which is kept between 1-10 torr of hydrogen.

The growth chamber is a cold wall system, using a bank of tungsten-halogen lamps to radiatively heat the wafer through a quartz tube. Immediately following the wafer transfer from the load-lock to the reactor, a flow of 1 slpm of hydrogen is passed through the reactor while the reactor pressure was maintained at 1 torr. The hydrogen is purified through a “Nanochem” [8] purifier, which is specified to reduce the impurity concentrations in the hydrogen to less than 10 parts per billion (ppb). The growth of silicon and silicon-germanium layers is done by rapid thermal chemical vapor deposition (RTCVD) [3] using dichlorosilane and germane as source gases and hydrogen as the carrier gas.

For our standard growth, a high temperature clean (to desorb oxygen) in hydrogen at 250 torr at 1000°C is then performed, followed by the growth of a high temperature Si buffer layer at 1000°C. Low-temperature (e.g. 625°C for SiGe or 700°C for Si) layers are then grown following the buffer. The 1000°C cleaning step and buffer layer were frequently omitted or modified in the work described in this chapter, since our goal was to develop cleaning steps which would not cause the diffusion of any existing dopant profiles. Silicon and SiGe layers are typically grown at 6 torr in a 3 lpm hydrogen carrier with 26 sccm dichlorosilane and varying germane levels.

7.3 Characterization of Interfaces

All Si/SiGe interfaces were characterized using photoluminescence (PL) from the pseudomorphically strained SiGe layers, which were immersed in a bath of liquid nitrogen after growth. An argon ion laser tuned to 514 nm was used as the excitation source, and a liquid-nitrogen-cooled Ge detector combined with a lock-in amplifier was used to measure the emitted light. The pump power density was approximately $\sim 50 \text{ W/cm}^2$. Most of the minority carriers are generated in the substrate, and then diffuse to the SiGe quantum well [9]. Therefore, the technique is best suited for structures without any barriers for carrier flow from the absorption region, a few microns into the substrate, to the SiGe layer. A typical spectrum is shown in fig 7.1. Luminescence intensity from the strained SiGe layer is extremely sensitive to the carrier lifetime in the SiGe layer [3,10]. Therefore any defects or contamination at the Si/SiGe interfaces which lead to increased non-radiative recombination of excited carriers reduce the overall luminescence intensity emitted from the $\text{Si}_{1-x}\text{Ge}_x$ layer. The total integrated SiGe luminescence was normalized to the total integrated luminescence from the bulk silicon to account for any lifetime variation in the silicon substrates that would affect the PL intensity from the SiGe layer.

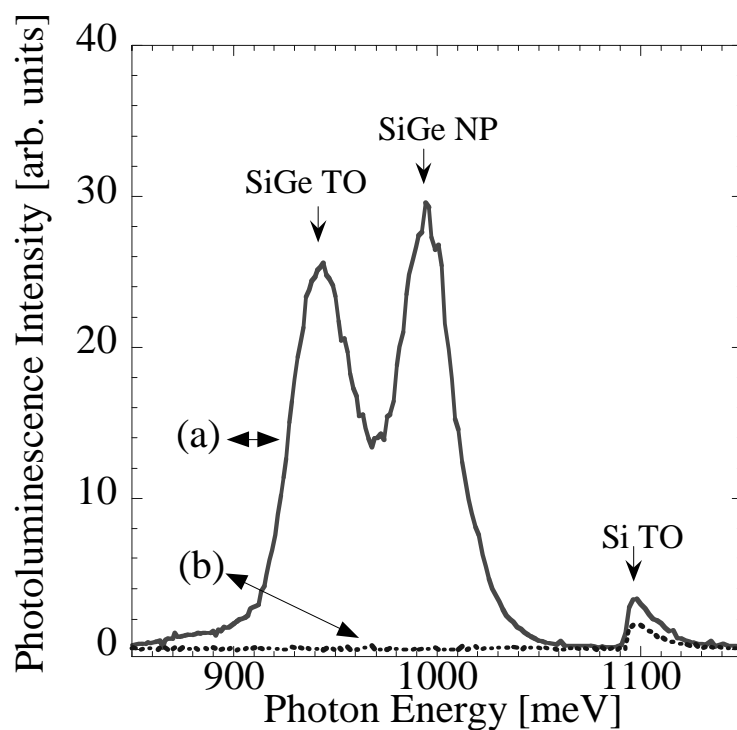


Figure 7.1. Typical photoluminescent spectrum at 77 K of a “clean” $\text{Si}_{0.8}\text{Ge}_{0.2}$ 200 nm silicon layer capped with silicon. Sample (a) has an integrated contamination of carbon and oxygen below SIMS detection limits; while (b) has an integrated contamination of $2 \times 10^{12} \text{ cm}^{-2}$ and $1 \times 10^{14} \text{ cm}^{-2}$ of carbon and oxygen respectively.

Some buried interfaces were also characterized using SIMS done at Evans East, in East Windsor, NJ using a 3 keV Cs^+ primary ion beam. Sputter rates were between 5-15 Ångstroms/second, producing oxygen and carbon detection limits of approximately 10^{18} cm^{-3} and 10^{17} cm^{-3} respectively for most samples. Sputter rates were determined using profilometry leading to ~5% uncertainty in depth profiles and chemical species concentrations were measured to within 15% error.

Different cleaning procedures resulted in some interfaces that were contaminated with carbon or oxygen. In these samples with higher oxygen or carbon levels at the Si/SiGe interfaces, the PL intensity from the SiGe decreased, presumably due to recombination sites caused by the contamination (fig. 7.1). Therefore, in this work the PL intensity is often used as a probe of interfacial cleanliness since data can be obtained more quickly than with SIMS. It also directly measures the electrical quality of the SiGe.

7.4. Ex-situ wet cleaning

7.4.1 Introduction

In this section, the chemical wet treatment performed on the wafer before loading into the reactor was studied and optimized. The treatment serves to remove the majority of surface contaminants and to passivate the surface against further contamination. P-type silicon (100) surfaces were prepared with a series of different wet cleaning methods. They were then loaded into the reactor, followed by growth of a thin $\sim 200\text{\AA}$ $\text{Si}_{0.8}\text{Ge}_{0.2}$ layer without any in-situ cleaning step or buffer layers directly above the wet-cleaned surface. A 450\AA silicon layer was subsequently grown above the $\text{Si}_{0.8}\text{Ge}_{0.2}$ layer. Thus carriers in the $\text{Si}_{0.8}\text{Ge}_{0.2}$ layer are subject to effects of contamination on the original Si surface. In this set of experiments no in-situ high-temperature cleaning process or high-temperature silicon buffer was grown, since our goal was to study the effect of only the wet clean.

After transferring the wafer from the load lock to the growth chamber, the hydrogen flow rate is increased to 3 slpm and the pressure is raised to 6 torr, followed by heating the wafer to the growth temperature of 625°C over a period of 2 minutes. When the growth temperature is reached, dichlorosilane is injected into the reactor chamber (in addition to the already flowing hydrogen) followed by germane injection approximately 5 seconds later, to grow the SiGe layer, at a growth rate of ~100 Å/min. Following the growth of the SiGe layer, the Ge source was turned off and a Si capping layer was grown after raising the temperature to 700°C for 15 minutes.

Germane is known to react with silicon dioxide to form the volatile species GeO_x . Oxide removal using germane at temperatures of 650-700°C has been reported [11]. These reports found, however, that for sub-monolayer oxides, germanium adsorbs preferentially to the bare silicon surface rather than forming the volatile germanium-oxide [11]. The sequence of dichlorosilane followed by germane was chosen to allow the SiGe layer to grow as soon as the germane is injected. Because the SiGe layer grows quickly on the silicon surface with no observable long incubation time, and the germane molecule prefers the open silicon surface site over that of the oxide site, it is concluded that the germane-induced oxide desorption has a negligible effect on the total oxygen concentrations buried at the interface between the silicon surface and the SiGe layer.

Following the initial HF dip and chemical oxidation as described earlier, the concentration (and thus pH) for the final HF step before loading was varied. The

wafer was dipped in a final oxide etch with a pH of 1-7.8 for a minimum of 20 minutes. The HF to DI ratio for this final oxide stripping step was varied from 1 to a 1000 parts DI to one part HF (49%) (pH between 1 and 3) to determine the effect of the HF concentration. Less acidic solutions were also examined, using HF buffered with NH_4F (pH ~4) or slightly basic 40% NH_4F (pH~7.8) instead of HF and water.

Although the wafer surface becomes hydrophobic at shorter times (~10 minutes in 1:1000 HF(49%) in DI), the minimum 20 minute etch time was chosen to insure sufficient time for the oxide removal reaction to go to completion. PL from $\text{Si}_{1-x}\text{Ge}_x$ layers grown above surfaces that were rinsed in DI after an HF dip (1:1000 HF(49%) in DI) were completely quenched. Presumably, dissociated OH^- ions oxidize the silicon surface [12,13] resulting in a poor Si/SiGe interface, which quenches the PL from the $\text{Si}_{1-x}\text{Ge}_x$ layer. Therefore, after the dilute HF dip step any residual droplets on the mostly dry surface were blown off with nitrogen, but not rinsed. However, no SIMS or further work was done to confirm this hypothesis. The hydrogen passivated surface was then exposed to laboratory atmosphere for 1-20 minutes before loading into the load-lock. High quality interfaces were achieved even after 15-20 minutes of exposure to air, indicated by intense PL from $\text{Si}_{1-x}\text{Ge}_x$ layers grown above the exposed surface.

A monotonic increase in the relative PL intensity from the $\text{Si}_{0.8}\text{Ge}_{0.2}$ layer was found as the HF concentration was decreased (fig. 7.2), indicating less contamination. However solutions more basic than the most dilute HF dip led to a decrease in lumi-

nescence intensity from the $\text{Si}_{0.8}\text{Ge}_{0.2}$ layer ($\text{pH}>3$). This optimum treatment of $\text{H}_2\text{SO}_4/\text{H}_2\text{O}_2$ (70°C , 20 min.) followed by a 1:1000 HF/DI dip (after removing the native oxide using a 1:100 HF/DI dip) was also applied directly to a $\text{Si}_{0.8}\text{Ge}_{0.2}$ surface. The $\text{Si}_{0.8}\text{Ge}_{0.2}$ surface was grown at 625°C on top of a 1000°C Si buffer followed by removing the exposed $\text{Si}_{0.8}\text{Ge}_{0.2}$ surface from the reactor and leaving it in the laboratory atmosphere for 3 days. The $\text{Si}_{0.8}\text{Ge}_{0.2}$ surface was then treated with the same wet clean as that used for the pure silicon surfaces followed by reinserting the $\text{Si}_{0.8}\text{Ge}_{0.2}$ surface into the reactor for the 700°C growth of a Si cap without any hydrogen baking. The PL intensity from the resulting structure was more intense, 7.4, than the case where the pure silicon surface was cleaned followed by a silicon capped $\text{Si}_{0.8}\text{Ge}_{0.2}$ layer, 3.8 (fig. 7.2). Thus we conclude the combination of $\text{H}_2\text{SO}_4/\text{H}_2\text{O}_2$ and 1:1000 HF:DI dip is also effective in preparing clean SiGe surfaces.

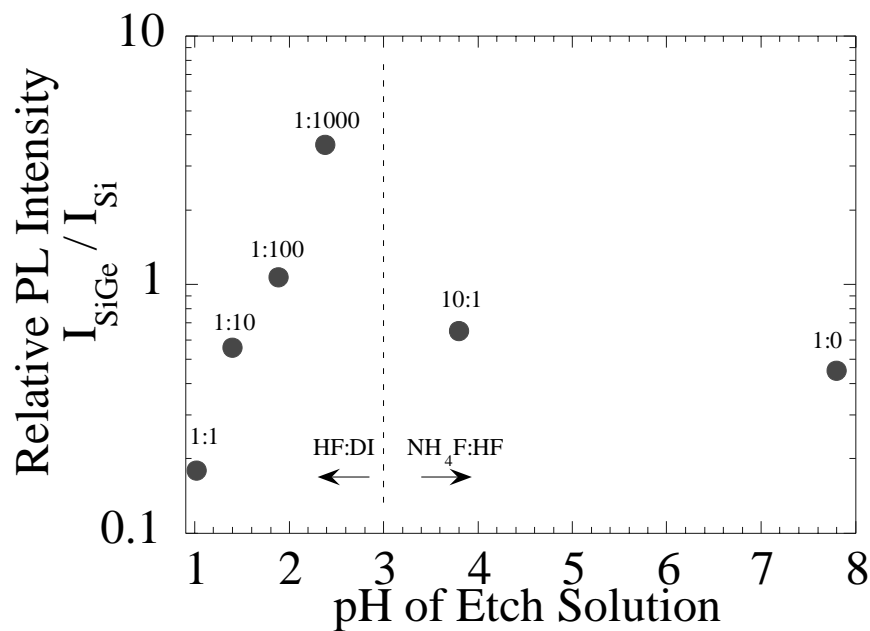


Figure 7.2. Relative photoluminescence SiGe/Si (PL) intensity at 77K from commensurately strained $Si_{0.8}Ge_{0.2}$ alloys followed by silicon caps grown directly above wet-chemically-treated silicon surfaces vs. the pH of the solution used to etch the wet chemical oxide on silicon. The ratios of either HF (49%) to DI water, or NH_4F (40%) to HF (49%) are indicated above their respective points. In one case the HF dip was also done instead on top of SiGe, followed by a 700°C Si cap.

SIMS was available for silicon surfaces, which were not subjected to the standard wet chemical clean, but rather were prepared by silicon growth in the RTCVD reactor. The wafers were then removed from the reactor and immersed for various times in either 1:10 or 1:100 HF(49%):DI (pH's = 1.4 or 1.9, respectively). The samples were then returned to the reactor through the standard loading procedure. The surfaces were then buried under an epitaxial SiGe layer and Si cap as described earlier

in this section. The integrated carbon and oxygen levels are ~5 times higher for a pH of 1.4 than 1.9, and fluorine is only found for pH of 1.9 (fig. 7.3).

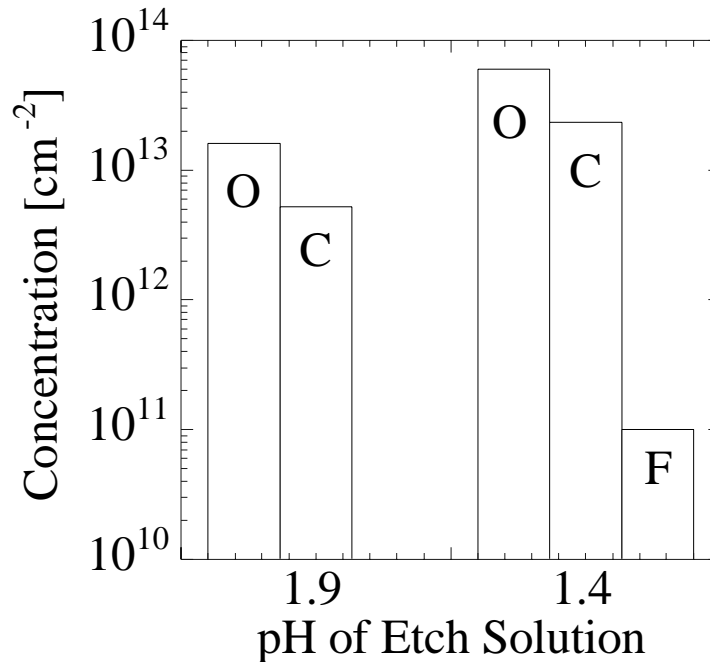


Figure 7.3. The carbon, oxygen, and fluorine concentrations detected by SIMS at Si/SiGe interfaces from SiGe layers grown directly at 625°C on Si surfaces treated with HF:DI solution of pH 1.4 and 1.9 to remove the wet chemical oxide, without a hydrogen pre-bake.

This decrease in contamination as pH is raised (to at least to pH of 3) may be related to the fact that (111) micro-faceting of the (100) silicon surface is known to increase with increasing pH [14], due to anisotropic etching by OH⁻ ions [15,16]. The resulting monohydride-terminated (111) surface has an oxygen sticking coefficient ~100 times lower than the dihydride terminated (100) hydrogen-passivated surface

[17,18,19]. Therefore less contamination and an increase in SiGe PL would be expected with increasing pH and increased microfacetting.

The increased fluorine contamination with increasing HF concentration has previously been observed [20,21,22]. The observed increase in carbon contamination at low pH could also be due to organic content in the process chemicals, which would increase with increased process chemical concentrations [20,21]. The reason for the decrease in SiGe PL at pH greater than 3 is not known. Silicon substrates cleaned with NH_4F have been reported to have an increased density of crystallographic defects in the epitaxial silicon grown above the prepared surface [23], which could be responsible for the reduced PL. However, the epitaxial films were not examined for crystallographic defects, therefore, different surface termination or impurities from the NH_4F solution can not be ruled out as causes for the PL quenching.

7.5. Contamination from Reactor, Load-Lock, and Laboratory Environment

7.5.1 Experiment

In our system, wafers are introduced to the growth chamber through a load lock, which is pumped by a rotary vane pump using hydrocarbon-based oil. The load-lock was therefore examined as a source of carbon contamination. Clean pseudomorphically strained $\text{Si}_{0.8}\text{Ge}_{0.2}$ surfaces were prepared by growing a silicon epitaxial buffer layer followed by a thin 200\AA $\text{Si}_{0.8}\text{Ge}_{0.2}$ layer. Immediately after growth, the chamber was purged with a continuous flow of 3 slpm of hydrogen at 6 torr. The wafer is allowed to

cool for 15 minutes before being moved to the load-lock where parts or all of the loading procedure were simulated. After transferring back to the growth chamber, the wafer was then heated to 700°C (ramp rate 50°C/sec) in 3 lpm H₂, and after ~15 sec at 700°C dichlorosilane was switched on to grow an epitaxial silicon cap (45 nm). No high-temperature cleaning steps in excess of 700°C were used. The upper SiGe/Si interface was then examined by SIMS and PL to look for contamination introduced by the load-lock.

Four experiments on SiGe surfaces were done before returning the wafer to the deposition chamber for a capping silicon layer:

Trial A: leave wafer in reactor;

Trial B: transfer wafer to load-lock + simulate load-lock pump-down;

Trial C: trial B + vent load-lock to atmosphere + load-lock pump-down;

Trial D: trial C, except the wafer is moved to the fume hood;

To first determine whether the growth chamber itself contributes any contamination to the surface (apart from the load-lock), the SiGe layer wafer A was simply left in the growth chamber without transfer to the load lock. The wafer was allowed to cool in 3 slpm of H₂ at 6 torr for 15 minutes. This time exceeds the time required to transfer the wafer to the load-lock and therefore simulates a maximum contribution of the growth chamber's contamination to the wafer surface. The wafer was then reheated to 700°C and a silicon cap was grown as described above. No oxygen or car-

bon is detected by SIMS at the interrupted SiGe/Si interface (figs. 7.4, 7.6). This layer exhibited intense photoluminescence also indicating negligible contamination at the interface due to the 15 minutes spent in the reactor chamber between layers.

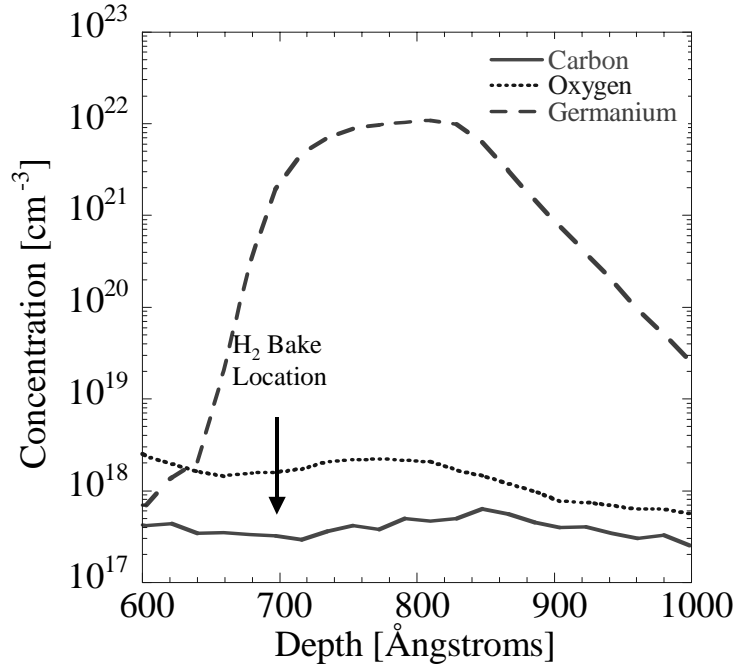


Figure 7.4. Oxygen, carbon and germanium SIMS profiles of a sample in which a commensurately strained Si_{0.8}Ge_{0.2} surface prepared in-situ by rapid thermal chemical vapor deposition, then allowed to cool for 15 minutes with 3 slpm of hydrogen flowing at 6 torr before burying the test surface with silicon epitaxy using dichlorosilane at 700°C (Wafer “A”). The hydrogen bake was done at the silicon depth of ~700Å.

Wafer B was transferred to the load-lock after the SiGe growth. A purge cycle, consisting of pressurizing the load-lock to 1-10 torr with dry nitrogen followed by evacuation with a rotary vane pump, was repeated 6 times to simulate the load-lock transfer without exposure to atmosphere. SIMS of the buried interface detected barely

observable C and O peaks (fig. 7.5 at depth of 0.13 μm) with integrated densities in both cases $<10^{12} \text{ cm}^{-2}$. To simulate the entire loading process from removal of the substrate from the ex-situ dilute HF dip to loading and purging of the load-lock, two more cases were examined: (Wafer C) a strained SiGe layer was transferred to the load-lock, given a nitrogen purge cycle, left in the load-lock for 5 minutes with the door of the load-lock left slightly open to the laboratory atmosphere, and then sent through a second purge before being returned to the growth chambers. After SiGe growth, Wafer D was taken out of the load-lock and moved to a chemical hood for 10 minutes, after which the wafer was returned to the reactor through the standard loading and purge cycles without any HF dip or wet processing.

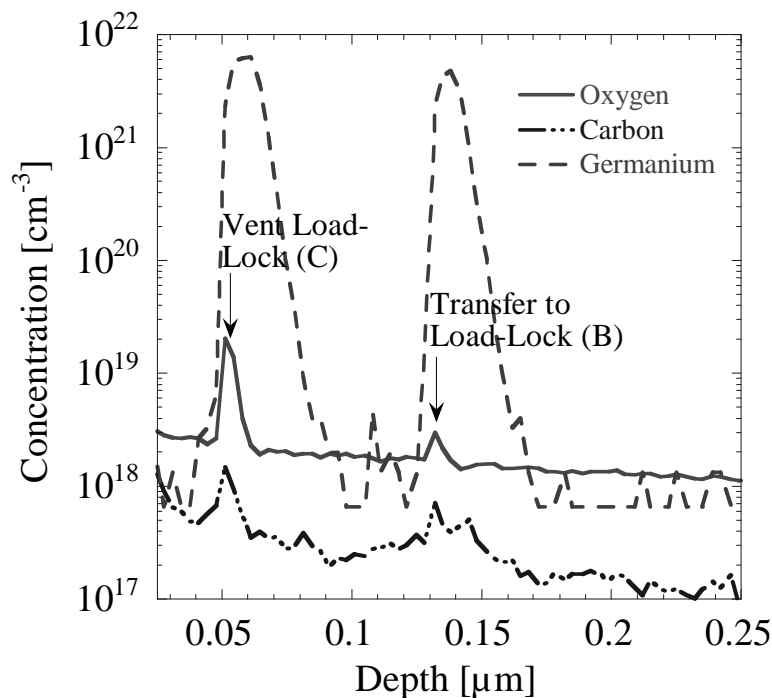


Figure 7.5. Oxygen, carbon and germanium profiles at SiGe/Si interfaces when the sample was transferred to the load lock (B) without venting to air, and (C) with venting to air, before silicon cap regrowth at 700°C.

SIMS of Wafer B to (nitrogen only atmosphere in the load lock) and of Wafer C (door of load lock slightly opened) showed only a small increase in contamination (figures 7.5, 7.6). However when the wafer was removed from the load-lock and exposed to atmospheric conditions of the laboratory (Wafer D), the carbon and especially the oxygen contamination increased significantly (fig. 7.6). Finally, to compare the susceptibility of SiGe surfaces to Si surfaces for contamination, in one case (Wafer E) a virgin Si wafer was left in the fume hood for 10 minutes after a 100:1 DI:HF dip before loading and the growth of a silicon cap at 700°C. Oxygen and carbon concen-

trations for this wafer are 5-10 times less than those of Wafer D (fig. 7.6), in which a presumably clean and H-terminated SiGe surface from the reactor was exposed similarly to air for ten minutes.

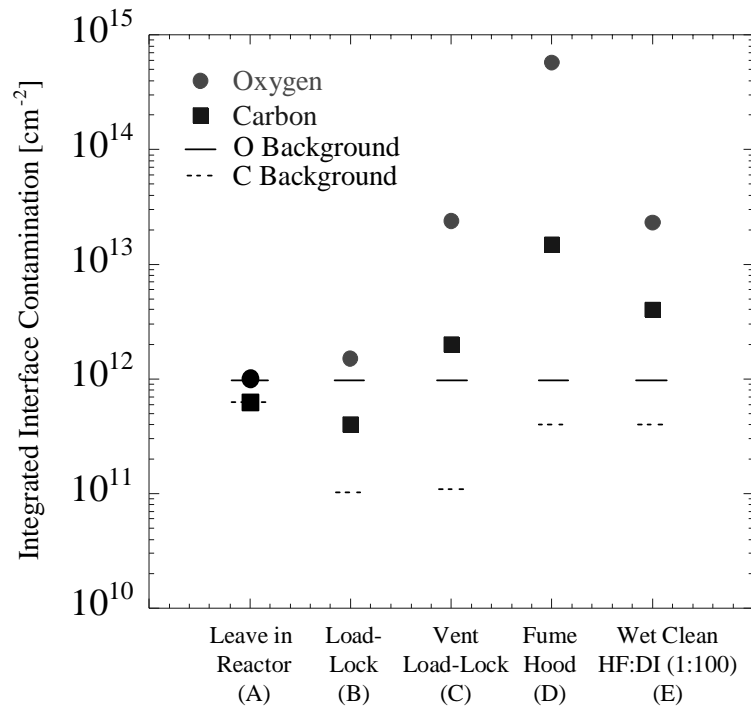


Figure 7.6. Integrated oxygen and carbon levels observed at SiGe/Si interfaces by SIMS for wafers (A-D) subjected to different conditions after SiGe growth before Si cap growth at 700°C without high temperature cleaning. In case E, the test surface is not prepared in-situ as in cases A-D, a silicon substrate surface after 1:100 HF:DI dip is transferred to the load-lock (total time in fume-hood ~10-15 minutes) before silicon growth at 700°C. Note: solid and dashed lines indicates SIMS detection limits for oxygen and carbon respectively (SIMS background multiplied by typical contamination peak widths).

7.5.2 Discussion

Several conclusions can be drawn from this series of experiments. First, the reactor itself is a relatively clean environment for short times for cold hydrogen passivated surfaces. Most significantly, the load-lock itself introduces only minimal contamination. Most contamination is caused by the exposure of the wafer surface to the laboratory environment. Finally, the hydrogen-terminated surface of the in-situ prepared SiGe surface is much more susceptible to oxygen and carbon absorption than a hydrogen-terminated Si surface. The difference in reactivity of the in-situ prepared SiGe surface compared to the surface prepared in a 1:100 dilute HF dip may be due to differences in the stability of the hydride termination of the two cases, which can result from different reconstructions of the surface [24], or because the H-Ge bond is weaker than the H-Si bond [25].

7.6. In-situ Wafer Cleaning

7.6.1 200-400°C pre-bakes

The purpose of a very low-temperature (e.g. 200-400°C) bake is to desorb physisorbed chemical contamination from the surface before the chemical contamination can dissociate and chemisorb to the wafer surface, which occurs first at higher temperatures [26]. Any chemisorbed carbon that is consequently annealed at high temperature can form stable SiC precipitates on the surface [27] or diffuse into the bulk [27], leading to undesirable defect formation.

To test the effectiveness of low-temperature pre-bakes on the interface quality, (100) wafers were subjected to the standard wet clean and loading procedure, followed by a low-temperature pre-bake before epitaxy. No high-temperature bake was used. The wafers were baked at $\sim 300^\circ\text{C}$ at 6 torr under a hydrogen flow of 3 lpm. A 200\AA $\text{Si}_{0.8}\text{Ge}_{0.2}$ layer was grown at 625°C immediately after the hydrogen bake, followed by a 450\AA silicon capping layer to reduce surface recombination effects on photoluminescence intensity [28]. The time dependence of the interface quality on the hydrogen pre-bake was examined using photoluminescence intensity (fig. 7.7). Because the PL intensity decreased with extended low temperature pre-baking it was concluded that the surface quality is degraded, not enhanced by a low-temperature pre-bake in our system.

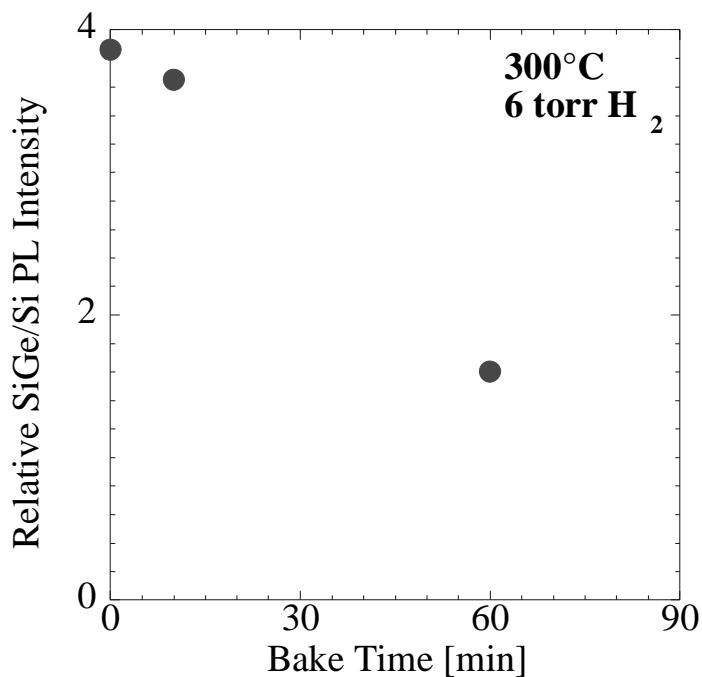


Figure 7.7. Relative SiGe/Si photoluminescence intensities from SiGe/Si layers grown directly on silicon (100) substrates prepared using 1:1000 HF(49%):DI and then baked in 6 torr of H₂ at 300°C for different times before SiGe growth.

7.6.2 700-800°C Bakes in Hydrogen

The complete removal of oxygen and carbon from silicon surfaces before epitaxy by baking in hydrogen atmospheres at higher temperatures (750-850°C) has been previously reported for UHV-CVD [4,29]. Their success has been attributed to low oxygen and water-vapor partial pressures, below the critical levels required for clean silicon surfaces in a vacuum at a given temperature [30,31]. Ref's. [4] and [29] stressed the importance of both the UHV system and the hydrocarbon-free “dry” load-lock system. Later, Wolansky et. al. demonstrated that oxygen and carbon removal could be

obtained at higher hydrogen pressures for nearly equivalent thermal budgets [1], showing that UHV is not a necessary condition for the cleaning of the silicon surface in hydrogen at or under 800°C, and that the cleaning temperature could be reduced to as low as 760°C. However, some carbon contamination was seen at the cleaned interface by SIMS in that report. In our work, hydrogen bakes were examined for different pressures and temperatures ranging from 0.5-250 torr and 700 to 800°C.

7.6.2.1 700°C Bakes in Hydrogen

The growth of silicon epitaxial layers at 700°C was interrupted, after which the substrates were then allowed to cool to less than 200°C in 3 slpm hydrogen at 6 torr in the reactor. In Sec. 4.1, we showed this introduced no contamination to a SiGe surface. A silicon surface would presumably also remain clean due to the higher stability of hydrogen on its surface (Sec. 4.1). After cooling, for approximately 15 minutes, the reactor pressure was set between 0.25-250 torr, with a hydrogen flow of 3-4 lpm, immediately followed by reheating the wafer to 700°C. The temperature, flow, and pressure were maintained constant for between 2-15 minutes, with the exception of the hydrogen bake at 0.25 torr in which the hydrogen pressure was held constant by turning off the hydrogen flow and sealing the chamber. After the hydrogen bake the pressure was then brought to 6 torr with a flow of 3 slpm of hydrogen. Dichlorosilane was then added to the hydrogen stream to grow epitaxial silicon and bury the test interface. The oxygen and carbon absorption rates during the bake were determined by dividing

the integrated carbon and oxygen concentrations found at the interface (determined by SIMS), by their respective annealing times. At lower pressure, for example 0.6 torr, the absorption rates for oxygen and carbon were $1.6 \times 10^{14} \text{ cm}^{-2} \text{ min}^{-1}$ and $1.4 \times 10^{12} \text{ cm}^{-2} \text{ min}^{-1}$ respectively (Table 1). However, for pressures of 6 and 250 torr of hydrogen both oxygen and carbon concentrations were below SIMS detection limits. For the 6 torr case the adsorption rates were less than $7 \times 10^{10} \text{ cm}^{-2} \text{ min}^{-1}$ and $7 \times 10^9 \text{ cm}^{-2} \text{ min}^{-1}$, and for 250 torr the detection limits were anomalously high leading to a higher maximum bound on the adsorption rates, which were $5 \times 10^{12} \text{ cm}^{-2} \text{ min}^{-1}$ and $5 \times 10^{11} \text{ cm}^{-2} \text{ min}^{-1}$ for oxygen and carbon respectively

Table 1: Integrated oxygen and carbon interface levels measured by SIMS and inferred adsorption rates for Si surfaces baked in hydrogen at pressures from 0.25 to 250 torr for various times. All hydrogen pressures were maintained with a steady flow rate of 3-4 lpm of hydrogen and baked at 700°C except for 0.25 torr, which was baked with no hydrogen flowing. Less than or equals indicates no O or C detected within the resolution of SIMS and the given rate is calculated from the limit of SIMS background for the sample.

Pressure [torr]	Time [min]	Oxygen [cm ⁻²]	Carbon [cm ⁻²]	Oxygen Adsorption Rate [cm ⁻² min ⁻¹]	Carbon Adsorption Rate [cm ⁻² min ⁻¹]
0.25	2	8.7 x 10 ¹⁴	2.8 x 10 ¹²	4.4 x 10 ¹⁴	1.4x10 ¹²
0.6	15	1.6 x 10 ¹⁵	4.9 x 10 ¹²	1.0 x 10 ¹⁴	3.2x10 ¹¹
6	15	≤ 1x10 ¹²	≤ 1x10 ¹¹	≤ 7x10 ⁹	≤ 7x10 ⁹
250	2	≤ 1x10 ¹³	≤ 1x10 ¹²	≤ 7x10 ⁹	≤ 5x10 ¹¹

While the bakes at pressures at or over 6 torr did not contaminate the surface, in our lab they have also not been effective at removing previously existing contamination, presumably because the temperature is too low for rapid enough desorption. A previously prepared SiGe surface exposed to atmosphere for over three days was prepared by wet cleaning, using the optimal 1:1000 HF(49%):DI ratio. The wafers were loaded into the RTCVD for the growth of a silicon cap at 700°C. The quality of the

SiGe layer and its interfaces were probed by PL. Performing a 10 min bake at 700°C at 6 torr in 3 lpm H₂ before the Si epitaxy showed no improvement in the SiGe/Si PL intensity compared to that of a wafer grown without such a step. Also, there was no observed PL dependence on when the dichlorosilane was introduced (i.e. either before or after the wafer was heated to 700°C). Further work is needed to evaluate longer 700°C hydrogen bake times and pressures for any potential cleaning benefits.

7.6.2.2 800°C Bake in Hydrogen

Since 700°C bakes were not effective, 800°C hydrogen bakes were tested to remove oxygen and carbon from the silicon surface after wet cleaning. Silicon surfaces were cleaned ex-situ before introduction to the reactor, as described before using the optimal 1000:1 DI/HF final dip (Sec. 3). After loading, the hydrogen flow is set to 3-4 lpm and the hydrogen pressure in the reactor is brought to between 0.5 and 250 torr. The wafer was then heated and held at 800°C for 1 minute, after which the temperature is reduced to 625°C while stabilizing the pressure to 6 torr (at 3 lpm H₂). After both pressure and temperature are stable (requiring ~ 1 minute for all pressures except 250 torr which required ~ 5 minutes), DCS followed shortly after by germane were injected into the reactor to grow a Si_{0.8}Ge_{0.2} (20nm) layer, followed by a Si capping layer at 700°C. PL results, and integrated oxygen and carbon concentrations (by

SIMS) at the lower Si/SiGe interface for different pressures and for different times at 800°C are shown in figures 7.8, 7.9, and 7.10, respectively.

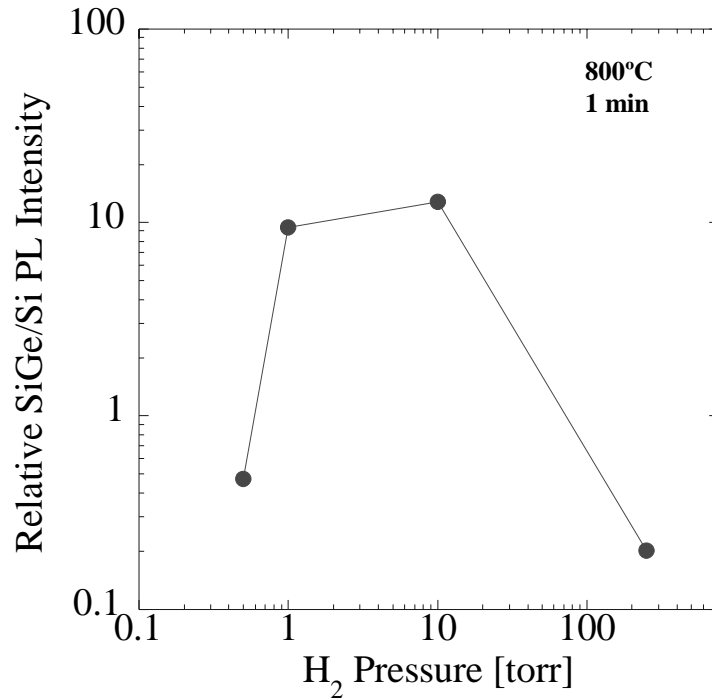


Figure 7.8. Relative SiGe/Si photoluminescence intensities from SiGe/Si layers (20nm/45nm) grown on silicon (100) substrates prepared using 1:1000 HF(49%):DI and then baked for 1 minute at 800°C at different hydrogen pressures.

If the hydrogen bake is omitted (wafer E, fig. 7.6), the integrated O and C levels are $2.3 \times 10^{13} \text{ cm}^{-2}$ and $4 \times 10^{12} \text{ cm}^{-2}$. Performing a hydrogen bake for 1 min at 0.5 torr slightly reduces the integrated oxygen level to $6.4 \times 10^{12} \text{ cm}^{-2}$ and increased the carbon level to $6.6 \times 10^{13} \text{ cm}^{-2}$. The 1 minute 250 torr bake dramatically increases the oxygen level to $9 \times 10^{13} \text{ cm}^{-2}$ and drops the carbon level to $2 \times 10^{12} \text{ cm}^{-2}$. The 1- and

10-torr bakes both reduced the oxygen to $\sim 10^{12} \text{ cm}^{-2}$, and the carbon levels were little changed from the no-bake levels ($\sim 10^{13} \text{ cm}^{-2}$). The SiGe/Si relative PL intensity dropped 10-100 times for 0.5 or 250-torr cleans, corresponding to the 10-100x increase in oxygen or carbon levels, therefore, the SiGe/Si PL ratio was consistent with SIMS in showing that the 1-10 torr cleans, which also had the lowest oxygen and carbon contamination, had the highest SiGe/Si PL ratios. The 1-10 torr bakes increased the SiGe/Si PL ratios from 1-4 without a bake to 9-12; this is in comparison to a ratio of 10-20, which is commonly observed for Si/SiGe/Si structures grown under our best conditions (grown without interruption, to minimize contamination, after a 1000°C hydrogen clean and silicon 1000° buffer layer on the substrates).

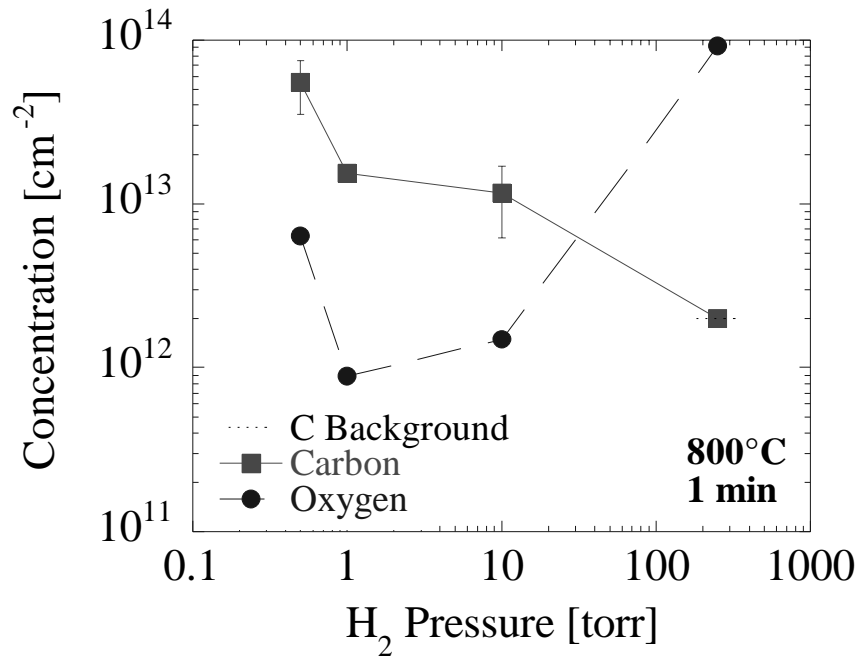


Figure 7.9. Integrated carbon and oxygen levels at SiGe/Si interfaces formed by growing SiGe on silicon (100) substrates prepared using HF dip and then baked for 1 minute at 800°C at different hydrogen pressures.

A longer hydrogen bake of 2 minutes at 800°C and 10 torr results in no detectable oxygen or carbon contamination above the SIMS background (fig.7.10), although the SIMS oxygen background was considerably higher in this case. The interrupted and uninterrupted growth are, therefore, indistinguishable with respect to PL and SIMS measurements. This cleaning technique (800°C, 2 min, 10 torr H₂) was also used in a Si/Si interface after ex-situ wet cleaning, followed by 700°C Si growth where a phosphorus layer marked the location of the interrupted interface. Again, absolutely

no carbon or oxygen was detected by SIMS at this interface, even with the integrated concentration detection limit due to SIMS background as low as 10^{12} cm⁻² for oxygen and 4×10^{11} cm⁻² for carbon (fig. 7.11).

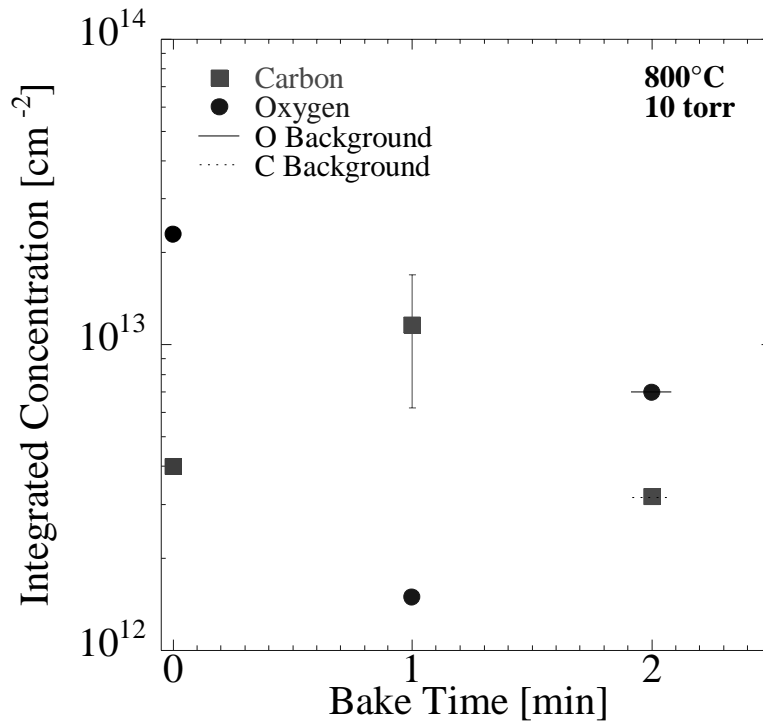


Figure 7.10. Integrated carbon and oxygen levels at Si/SiGe interfaces formed SiGe growth on silicon (100) substrates prepared using an HF dip to remove the wet chemical oxide and baked at 800°C in 10 torr hydrogen for various times. For a two minute bake, the oxygen level was below that resolvable by SIMS.

7.6.3. Discussion

The net oxygen or carbon adsorption or desorption to or from the silicon surface at different temperatures and hydrogen pressures depends on the flux to the surface, the sticking fraction of the flux that sticks to the surface, and the desorption rate. Hydrogen passivation of the surface, which increases at increasing hydrogen pressure, can

greatly reduce the sticking coefficient of oxygen [32]. However, a simple hydrogen passivation model fails to explain why during an 800°C bake, the adsorbed oxygen increases as the hydrogen pressure is increased from 6 torr to 250 torr (fig. 7.9). The increase in oxygen contamination at higher hydrogen pressure could be the result of oxygen or water vapor impurities in the hydrogen gas. The two sources of oxygen/water contamination are then the background in the reactor and the carrier gas itself. Because the hydrogen entering the reactor is purified to a level 10 ppb, the hydrogen gas can only become the dominant source of oxygen at high hydrogen pressures.

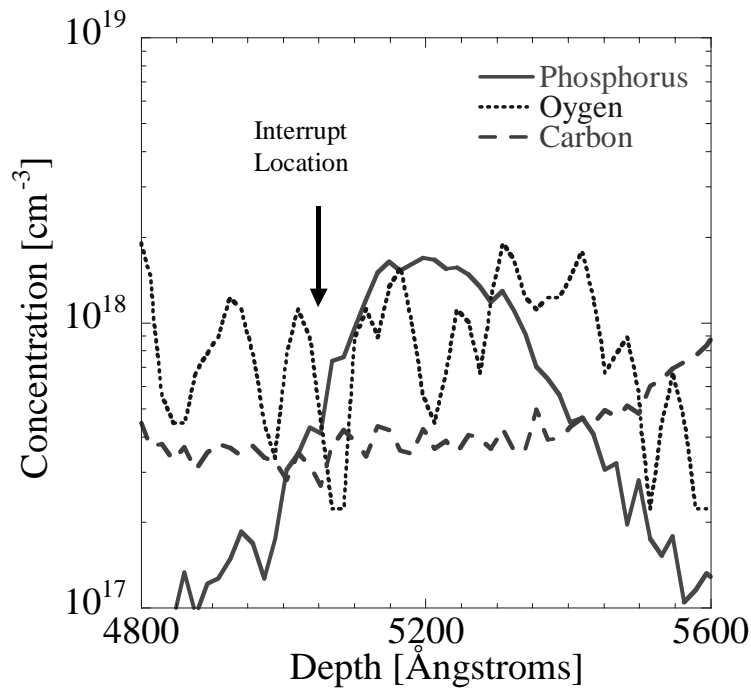


Figure 7.11. Oxygen, carbon and phosphorus SIMS profiles of a sample in which the phosphorus doped silicon marks the interrupt location, where the silicon surface is cleaned using the experimentally determined optimal ex-situ and in-situ conditions (i.e. using a 1:1000 HF(49%):DI to strip the final chemical oxide followed by a 800°C, 10 torr hydrogen bake for 2 minutes). The silicon cleaned interface is located at a depth of approximately 5050 Å.

Figure 7.12 schematically shows the two contributions to oxygen adsorption of hydrogen surface coverage and oxygen partial pressure, and their dependence on hydrogen pressure. The author stresses that this description is only a qualitative description, as details of the hydrogen surface coverage, and total oxygen background, are not exactly known. As the hydrogen pressure increases, the hydrogen coverage of the surface increases, which greatly reduces the number of open sites for O absorption

and thus the sticking coefficient [32]. This explains the relatively high contamination levels resulting from bakes at pressures below 6 torr at both 700 and 800°C. When the hydrogen pressure is too high, however, then the oxygen partial pressure, due to impurities in the hydrogen, may become so great that it produces an oxygen flux that can not be compensated for by the additional hydrogen coverage. At 700°C the hydrogen coverage at high pressure is still sufficient to keep the increased oxygen contamination in the gas below detection limits (SIMS detection limits were high in this case, Table 1). However, because silicon epitaxy in this reactor at higher hydrogen pressure (220 torr, 700°C) has shown indications of unusually high oxygen concentrations [10] and the oxygen SIMS detection limits were high (because of interference with surface contamination), it is still likely that the surface may be adsorbing oxygen at higher hydrogen pressures at 700°C. At 800°C the higher open site density vs. that at 700°C allows the increased gas contamination level to cause significant surface contamination, so that high pressure bakes contaminate the surface (fig. 7.9).

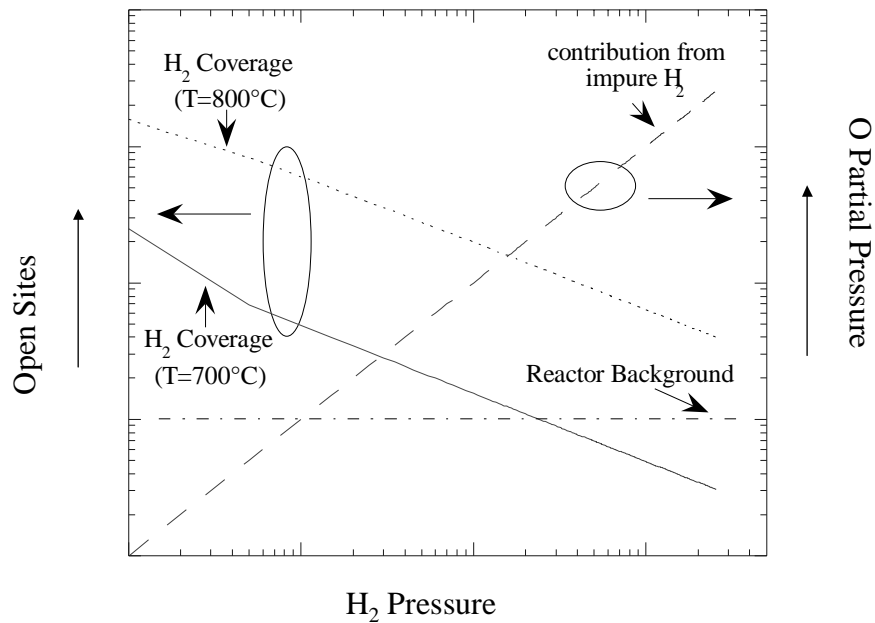


Figure 7.12. Schematic diagram of important mechanisms that determine the amount of oxygen sticking to the silicon surface during hydrogen baking. The decreasing fraction of open sites that are available for oxygen to stick (corresponding to increased hydrogen coverage) with increasing hydrogen pressure at 700°C and 800°C are referenced to the left axis. Oxygen partial pressures due to the oxygen background in the reactor and from impurities in the hydrogen gas are referenced to the right axis.

At 800°C, the cleanest surface is achieved between those two extremes, in the 1-10 torr range. The inability to further clean surfaces at 700°C, while still maintaining low contamination at high pressures (oxygen and carbon below SIMS detection limits), can be attributed to an oxygen desorption rate near the rate of oxygen adsorption. If the accumulative rate is indeed desorptive at this temperature it is still too slow to make an observable effect for the bake times considered in this study.

The surface concentration of carbon is also observed to have a dependence on hydrogen pressure. At the lowest hydrogen pressure of 0.5 torr, the detected carbon signal rises significantly, $6.6 \times 10^{13} \text{ cm}^{-2}$, but at higher hydrogen pressures, 250 torr, the carbon signal drops to below the SIMS detection limits, $2 \times 10^{12} \text{ cm}^{-2}$ after 1 minute at 800°C (fig. 7.9). The source of carbon depositing on the surface during baking at low hydrogen pressure, 0.5 torr, is likely from reactor background contamination. Presumably increasing the hydrogen coverage of the surface, by increasing the hydrogen pressure, will reduce the overall adsorption of carbon from the chamber atmosphere. Indeed, less carbon is observed for higher hydrogen pressure bakes, however, it is also observed that carbon is removed from the silicon surface for high hydrogen pressures, 10 torr and 250 torr, at 800°C . Two proposed mechanisms of carbon removal from the silicon surface during hydrogen baking at temperatures around 800°C are either desorption of carbon as hydrocarbons or methylsilanes [4, 29], or diffusion of carbon from the surface into the silicon bulk [27]. However, further analysis of these two possible mechanisms goes beyond the scope of this work due to limits of SIMS resolution (i.e. SIMS broadening and detection limits) and an incomplete knowledge of how much carbon is desorbed into the hydrogen atmosphere.

7.7. Summary

Photoluminescence (PL) from commensurately strained SiGe layers grown directly on silicon substrates and secondary ion mass spectroscopy (SIMS) of buried Si/SiGe interfaces are used to evaluate different low-temperature cleaning methods of substrate surfaces for silicon and SiGe epitaxy in a non-ultra-high vacuum system. Both the sources of contamination as well as effective cleaning methods were investigated. The dominant source of contamination came from the wafer being outside the reactor, not in the load lock or deposition chamber itself. The optimum surface preparation depends on the ratios of HF, NH_4F and de-ionized water of solutions that were used to remove the wet chemical oxide on the substrate surface. In-situ bakes between 300°C and 800°C in 0.25-250 torr of hydrogen were examined after the ex-situ clean using PL and SIMS measurements. 700°C bakes do not add contamination at sufficiently high hydrogen pressure, but are also ineffective at removing existing oxygen and carbon contamination. 800°C bakes between 1-10 torr can effectively remove contamination and give interfaces which are indistinguishable by SIMS or photoluminescence from those grown without interruption.

The pressure dependence of the interface cleaning at 700°C and 800°C may be understood by considering the effect of the hydrogen pressure on the reactivity of the surface. Because negligible dopant diffusion occurs for short times at 800°C , this demonstrated ability to grow pristine interfaces without exceeding 800°C after remov-

ing the wafer from the reactor will enable new strategies for device integration and fabrication, which in one case has already been successfully demonstrated in a vertical MOSFETs structure [34].

7.8 References

- [1] D. Wolansky, B. Tillack, K. Blum, K. D. Bolze, K. D. Glowatzki, K. Köpke, D. Krüger, R. Kurps, G. Ritter, P. Schley, in *Proceedings of the 8th International Symposium on Silicon Material Science and Technology*. *Silicon Material Science and Technology*, H. R. Huff, H. Tsuya, U. Gosele, Editors, p. 812-821. The Electrochemical Society Proceedings. Pennington. NJ (1998)
- [2] D. W. Greve, *Mat Sci. & Eng.*, **B18**, 22-51 (1993)
- [3] J. C. Sturm, P. V. Schwartz, E. J. Prinz, H. Manoharan, *J. Vac. Sci. Tech.*, **B9**, 2011 (1991)
- [4] M. K. Sanganeria, M. C. Öztürk, K. Violette, G. Harris, C. A. Lee and D. Maher, *Appl. Phys. Lett.* **66**, 1255-57 (1995)
- [5] C. W. Trucks, K. Raghavachari, G. S. Higashi, Y. J. Chabal, *Phys. Rev. Lett.*, **65**, 504-507 (1990)
- [6] B. Meyerson, F. Himpsel, K. J. Uran, *Appl. Phys. Lett.* **57**, 1034 (1990)
- [7] M. Nakamori and N. Aoto, *Jpn. J. Appl. Phys. pt 1*, **37**, 426-465 (1989)
- [8] "Nanochem 3000" purchased from Semi-Gas Systems, Inc. 625 Wool Creek Drive, San Jose CA 95112, 408-971-6500
- [9] A. St. Amour, J. C. Sturm, *J. of Material Science: Materials in Electronics*, **6**, 350-355 (1995)
- [10] Z. Matutinovic-Krstelj, E. Chanson, J. C. Sturm, *J. of Electronic Materials*, **24**, 725-730 (1995)
- [11] C.-L. Wang, S. Unnikrishnan, B.-Y. Kim, D.-L. Kwong, A. F. Tasch, *J. of Electrochemistry*, **143**, 2387 (1996)
- [12] M. Morita, T. Ohmi, E. Hasegawa, M. Kawakami, K. Suma, *Appl. Phys. Lett.*, **55** 562 (1989)
- [13] M. Weldon, B. Stefanov, K. Raghavachari, Y. J. Chabal, *Phys. Rev. Lett.*, **79**, 2851-54 (1997)
- [14] V. Thanh, D. Bouchier, D. Debarre, *Phys. Rev. B*, **56**, 10505 (1997)
- [15] Dumas, Y. J. Chabal, P. Jakob, *Surf. Sci.*, **269/270**, 867-78 (1992)
- [16] Y. Morita, H. Tokumoto, *Appl. Phys. Lett.*, **67**, 2654-56, (1995)
- [17] D. Gräf, M. Grundner, R. Schulz, L. Mülhoff, *J. Appl. Phys.*, **68**, 5155-61 (1990)
- [18] J. Westermann, H. Nienhaus, W. Mönch, *Surf. Sci.*, **311**, 101-106 (1994)
- [19] A. Stockhausen, T. U. Kampen, W. Mönch, *Appl. Surf. Sci.*, **56-58**, 795-801 (1992)
- [20] T. Takahagi, A. Ishitani, H. Kuroda, Y. Nagasawa, *J. Appl. Phys.*, **69**, 803-7 (1991)
- [20] A. Miyauchi, Y. Inoue, T. Suzuki, M. Akiyama, *Appl. Phys. Lett.*, **57**, 676-677 (1990)

- [22] K. Kinoshita, I. Nishiyama, *J. Vac. Sci. Tech A*, **13**, 2709, (1995)
- [23] S. L. Cohen, J. Blum, C. D'Emic, M. Gilbert, F. Cardone, C. Stanis, M. Liehr in *Chemical Surface Preparation, Passivation, and Cleaning for Semiconductor Growth and Processing*, R. J. Nemanich, C. R. Helms, M. Hirose, G. W. Rubloff. Editor. p. 499-504. Material Research Symposium Proceedings. Pittsburgh PA (1992)
- [24] J. E. Northrup, *Phys. Rev. B*, **44**, 1419-1422 (1991)
- [25] P. M. Garone, J. C. Sturm, P. V. Schwartz, S. A. Schwartz, B. J. Wikens, *Appl. Phys. Lett.*, **56**, 1275 (1990)
- [26] C. C. Cheng, S. R. Lucas, H. Gutleben, W. J. Choyoke, J. T. Yates, Jr., *Surf. Sci. Lett.*, **273**, L441-L448 (1992)
- [27] C. C. Cheng, P. A. Taylor, R. M. Wallace, H. Gutleben, L. Clemen, M. L. Colaiani, P. J. Chen, W. H. Weinberg, W. J. Choyoke, J. T. Yates, Jr., *Thin Solid Films*, **225**, 196-202 (1993)
- [28] A. St. Amour, J. C. Sturm, Y. Lacroix, M. L. W. Thewalt, *Appl. Phys. Lett.*, **65**, 3344-46 (1994)
- [29] K. Oda and Y. Kiyota, *J. Electrochemical Society*, **143**, 2361 (1996)
- [30] J. J. Lander and J. Morrison, *J. Appl. Phys.*, **33**, 1300 (1982)
- [31] F. W. Smith and G. Ghidini, *J. Electrochem. Soc.*, **128**, 1300, (1982)
- [32] P. V. Schwartz, J. C. Sturm, *J. Electrochem. Soc.*, **141**, 1284-1290 (1994).
- [33] M. Yang, M. Carroll, J. C. Sturm and T. Buyuklimanli, *J. Electrochem. Soc.*, **147** 3541 (2000)
- [34] M. Yang, C.-L. Chang, M. Carroll, J. C. Sturm, *IEEE Elec. Dev. Lett.*, **20**, 301 (1999)

Conclusion

8.1 Summary

This work was motivated by the need for ultra-sharp dopant profiles for high performance devices. Ultra-sharp dopant profile can be obtained by techniques like ion-implantation or epitaxy, making the primary challenge to controlling a dopant's position in a device its solid-state thermal diffusion during high temperature steps of the device fabrication. Diffusion lengths as small as 1-2 nm are shown to reduce the electrical performance of the SiGe HBT in chapter 3, demonstrating the sensitivity of modern devices to very small amounts of diffusion. Two approaches to control dopant diffusion are examined in this work: (1) reduce the dopant diffusivity through incorporation of substitutional carbon; and (2) reduce the thermal budget of critical processing steps. To study the effect of substitutional carbon on dopant diffusivity for part of this thesis work, it became necessary to develop a new gas chemistry (disilane) so that high substitutional carbon concentrations (up to ~ 0.5% carbon) could be incorporated into pure Si and low germanium concentration SiGe (7%), which is discussed in chapter 2. Most of this work was dedicated to understanding the mechanism by which substitutional carbon reduces the diffusivity of boron and phosphorus. The primary findings were that: 0.5% substitutional carbon incorporation in SiGeC reduces the boron diffusivity as much as 8 times below the intrinsic boron diffusivity; substitutional carbon “sinks” excess interstitials introduced by ion-implantation or oxidation through a

direct reaction between the interstitial and the substitutional carbon; the carbon-interstitial reaction may be used to non-locally suppress the enhanced diffusion effects of device processing steps; the carbon-interstitial reaction is “kick-out” like meaning that the reaction is one-to-one and produces mobile carbon. To quantify the carbon-interstitial reaction it was furthermore necessary to quantify the interstitial injection rate during oxidation, which included finding that the excess interstitial concentration is fixed at the surface of the silicon-oxide interface during oxidation. Finally, a low temperature cleaning technique for Si and SiGe epitaxy was developed as an alternative method to reduce dopant diffusion for device structures that require a second growth step.

8.2 Future Work

A primary motivation of this work was the control of dopant diffusion for sharp dopant profiles, which can be facilitated by the local or non-local effect of carbon on the interstitial concentration. However, reliable implementation of substitutional carbon in silicon based devices will demand a better understanding of how to avoid conditions that initiate the formation of incoherent silicon-carbide precipitation or carbon clusters that are potentially electrically active.

Another technological concern is the development of a fully predictive understanding of carbon and germanium’s effect on boron diffusion to reduce the costs of experimental trial and error methods of optimization of a transistor structure like the SiGe(C)

HBT. The effect of Ge incorporation on the boron diffusivity is still not entirely understood. Preliminary studies of the boron diffusivity in SiGe show that boron diffuses more slowly with increasing germanium concentration below 40% [1], Fig 8.1. The reduced boron diffusivity in SiGe is not believed to be due to a non-equilibrium under-saturation of silicon self-interstitials as is proposed for SiGeC, since SiGe does not “sink” interstitials as SiGeC does. Alternative explanations have been proposed for the germanium effect on diffusivity including local strain trapping [2] and band-gap effects on the defect level and carrier concentration [3-5]. However, none of these models accounts for the ultimate increase in diffusivity that the boron must have to reach the intrinsic boron diffusivity in pure germanium (Fig. 8.1) [6, 7]. An equally important challenge is developing a predictive model for the effect of the SiGe/Si transition on boron diffusion, e.g. segregation effects. Several models have been proposed [5, 8-10], however these remain relatively untested and there exist almost no reports of the effects of carbon on these properties. Therefore, significant work still remains to be done to understand the boron diffusivity in SiGe.

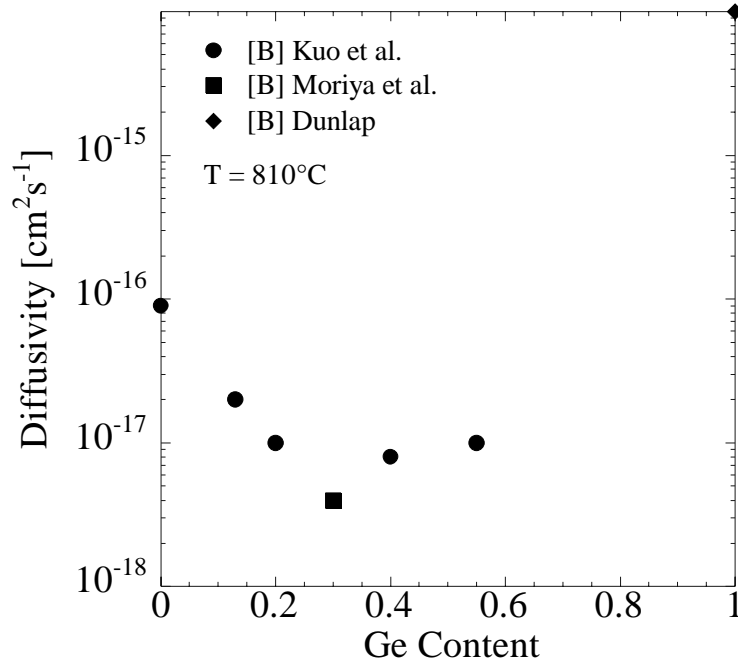


Figure 8.1. Boron diffusivity dependence on germanium content in strained $\langle 100 \rangle$ SiGe pseudomorphic to Si compared to the boron diffusivity in pure unstrained germanium [1,3,11] and pure silicon.

Finally two other critical questions from a technological stand-point that remain unresolved is the dependence of the intrinsic carbon diffusion and the rate of immobile carbon formation, e.g. precipitation, on germanium content. Despite these concerns and uncertainties, substitutional carbon incorporation used to control dopant diffusion remains an active and promising approach that is not yet fully explored. The technique has been successfully implemented in research device structures without detrimental electrical effects [12-14] and has been successful enough to now be developed for production in the case of the SiGeC HBT by companies like Motorola [15].

8.3 References

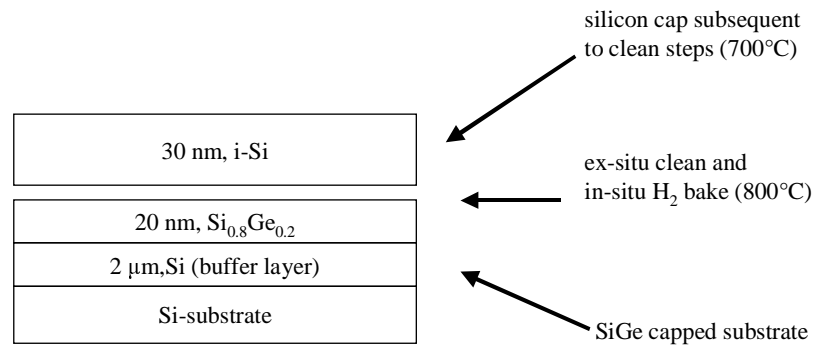
- [1] P. Kuo, J. L. Hoyt, J. F. Gibbons, J. E. Turner, and D. Lefforge, "Boron Diffusion in Si and SiGe," presented at Materials Research Symposium, 1995.
- [2] R. F. Lever, J. M. Bonar, and A. F. W. Willoughby, *J. Appl. Phys.*, vol. 83, pp. 1988, 1998.
- [3] N. Moriya, L. C. Feldman, H. S. Luftman, C. A. King, J. Bevk, and B. Freer, "Boron Diffusion in Strained SiGe Epitaxial Layers," *Phys. Rev. Lett.*, vol. 71, pp. 883, 1993.
- [4] S. M. Hu, D. C. Ahlgren, P. A. Ronsheim, and J. O. Chu, "Experimental Study of Diffusion and Segregation in a Si-(GeSi) Heterostructure," *Phys. Rev. Lett.*, vol. 67, pp. 1450, 1991.
- [5] S. M. Hu, "Diffusion and segregation in heterostructures: Theory, two limiting cases, and internal strain," *Phys. Rev. B*, vol. 45, pp. 4498, 1992.
- [6] B. L. Sharma, presented at Defects and Diffusion Forum, 1990.
- [7] W. C. J. Dunlap, *Phys. Rev.*, vol. 94, pp. 1531, 1954.
- [8] C.-H. Chen, U. M. Goesele, and T. Y. Tan, "Dopant diffusion and segregation in semiconductor heterostructures: Part 2. B in $\text{Ge}_x\text{Si}_{1-x}/\text{Si}$ structures," *Appl. Phys. A*, vol. 68, pp. 19-24, 1999.
- [9] J. Tersoff, "Forces on Charged Defects in Semiconductor Heterostructures," *Phys. Rev. Lett.*, vol. 65, pp. 887, 1990.
- [10] N. Moriya, L. C. Feldman, S. W. Downey, C. A. King, and A. B. Emerson, "Interfacial Segregation in Strained Heterostructures: Boron in $\text{Si}_{0.8}\text{Ge}_{0.2}/\text{Si}$," *Phys. Rev. Lett.*, vol. 75, pp. 1981, 1995.
- [11] W. C. Dunlap, *Phys. Rev.*, vol. 94, pp. 1531, 1954.
- [12] J. H. Osten, *Thin Solid Films*, vol. 367, pp. 101-111, 2000.
- [13] M. Yang, C.-L. Chang, M. Carroll, and J. C. Sturm, "25 nm p-channel vertical MOSFETs with SiGeC source/drains," *IEEE Electr. Dev. Letters*, vol. 20, pp. 301, 1999.
- [14] H.-J. Gossmann, C. S. Rafferty, G. Hobler, H. H. Vuong, D. C. Jacobson, and M. Frei, "Suppression of reverse short channel effect by buried carbon layer," presented at Technical Digest - International Electron Device Meeting, San Francisco, CA, USA, 1998.
- [15] B. Johnson, "Motorola ESTL plans to develop unique technology", 1999.

Appendix A

Growth Sequences

A.1 Low Temperature Clean Sample #2541

800°C, 1 minute, 10 torr clean used to clean a SiGe surface and grow a silicon cap on the uncapped SiGe. Cleaning sequence is the same used for the hydrogen bakes described in section 7.6.



Sequencer Table #0

Step #	Action	Comment
0	CONTROL ON&	Turn on control
1	SCAN(0.3)	Scan simulation
2	SET(SP7,0)	Override power zero
3	SET(SP4,0)	Turn off PID control
4	SET(SP0,0.6)	Zero loop counter
5	SET(DO0,0)	
6	SET(DO1,0)	Hydrogen select off
7	SET(DO2,0)	SiH4 select off
8	SET(DO3,0)	GeH4 select off
9	SET(DO4,0)	B2H6 select off
10	SET(DO5,0)	PH3 select off
11	SET(DO6,0)	Methylsilane (MS) select off
12	SET(DO7,0)	Dichlorosilane (DCS) select off
13	SET(DO8,0)	Disilane (DS) select off
14	SET(DO9,0)	SiH4 inject off
15	SET(DO10,0)	GeH4 inject off
16	SET(DO11,0)	B2H6 inject off
17	SET(DO12,0)	PH3 inject off
18	SET(DO13,0)	DCS/DS inject off
19	SET(AO0,0.21)	Hydrogen 1 slpm
20	SET(DO15,1)	Vac on
21	SET(DO1,1)	Hydrogen on
22	SET(AO1,0)	SiH4 MFC zero
23	SET(AO2,0)	GeH4 MFC zero
24	SET(AO3,0)	B2H6 MFC zero
25	SET(AO4,0)	PH3 MFC zero
26	SET(AO15,0)	DS MFC zero
27	SET(AO6,0.534)	DCS MFC 26 sccm
28	SET(AO7,0)	MS MFC zero
29	SET(AO8,0)	Pressure zero
30	SEQUENCER ON(0.3,1.0)	Start sequence #1

Sequencer Table #1

Step #	Action	Comment
0	SET(SP1,1)	Set layer number
1	SET(SP2, 0.0)	Reset loop counter
2	WAITUNTIL(AI24>0.5)	
3		
4		
5	SEQUENCER ON(0.3,5,0)	Call clean sequence
6	WAITUNTIL(SP2>0.5)	Clean sequence
7	SET(SP2,0.0)	Reset loop counter
8		
9	SET(AO8,0.6)	Pressure 6 torr
10	WAITUNTIL(AI28<6.5)	Pressure stabilize
11		
12		
13		
14		
15		
16	SEQUENCER ON(0.3,3,0)	Call cap sequence
17	WAITUNTIL(SP2>0.5)	Cap sequence
18	SET(SP2,0.0)	Reset loop counter
19		
20		
21		
22		
23		
24	RAMP(SP7,-0.4,0.0)	Lamps off
25		
26		
27		
28		
29	SEQUENCER ON(0.3,7,0)	Call shut down
30	WAITUNTIL(SP2>0.5)	Shut down

Sequencer Table #3

Step #	Action	Comment
0	SET(SP5,3.523)	Set T=700
1	SET(SP4,1.0)	Feed back on
2	WAIT(30)	Stabilize temperature
3		
4		
5		
6		
7		
8		
9		
10	SET(DO13,1.0)	DCS inject on
11	WAIT(900)	Cap layer
12	SET(DO13,0)	DCS inject off
13	WAIT(5)	Purge tube
14		
15		
16		
17		
18		
19		
20		
21		
22		
23	SET(SP4,0.0)	Feedback off
24		
25		
26		
27		
28		
29	SET(SP2,1.0)	End
30	END	

Sequencer Table #5

Step #	Action	Comment
0	SET(AO8,0.0)	Pump out
1	SET(AO11,1.0)	Low pressure select
2	WAITUNTIL(AI28<5.5)	Stabilize pressure
3	SET(AO0,0.617)	Hydrogen 3 slpm
4	SET(AO8,1.0)	Set pressure 10 torr
5	WAITUNTIL(AI28>5.5)	Stabilize pressure
6		
7		
8		
9		
10	WAIT(30)	Stabilize pressure
11		
12		
13	WAITUNTIL(AI24>0.5)	Go for cold values
14	SET(SP3,1)	Get cold values
15	WAIT(1)	
16	SET(SP3,0)	
17		
18		
19	RAMP(SP7,0.4,0.16)	Lamps on
20	WAIT(30)	Warm-up wafer
21	RAMP(SP7,0.4,0.19)	Approach 800 C
22	WAIT(30)	
23	SET(SP5,5.488)	Set T=800 C
24	SET(SP4,1.0)	Feed back on
25	WAIT(60)	Clean
26		
27		
28		
29	SET(SP2,1.0)	End sequence
30	END	

Sequencer Table #7

Step #	Action	Comment
0	SET(SP7,0)	Lamps off
1	SET(DO13,0)&	DCS inject off
2	SET(DO12,0)&	PH3 off
3	SET(DO11,0)&	B2H6 off
4	SET(DO10,0)&	SiH4 off
5	SET(DO9,0)&	GeH4 off
6	SET(DO7,0)&	DCS select off
7	SET(DO5,0)&	PH3 off
8	SET(DO4,0)&	B2H6 off
9	SET(DO3,0)&	SiH4 off
10	SET(DO2,0)&	GeH4 off
11	SET(DO1,0)&	H2 off
12	SET(AO8,0.0)&	Pump out
13	SET(AO7,0.0)&	B2H6 low
14	SET(AO6,0.0)&	DCS
15	SET(AO5,0.0)&	PH3 low
16	SET(AO4,0.0)&	PH3 high
17	SET(AO3,0.0)&	B2H6 high
18	SET(AO2,0.0)&	SiH4
19	SET(AO1,0.0)&	GeH4
20	SET(AO0,0.00)&	H2
21	WAITUNTIL(AI28<0.5)	Pump out
22	SET(D015,0)	Vac off
23	SEQUENCER OFF(0)	
24	SEQUENCER OFF(1)	
25	SEQUENCER OFF(2)	
26	SEQUENCER OFF(3)	
27	SEQUENCER OFF(4)	
28	SEQUENCER OFF(5)	
29	SEQUENCER OFF(6)	
30	SEQUENCER OFF(7)	

A.2 $\text{Si}_{1-x}\text{C}_x$ Sample Grown w/ Disilane #2963

SiC sample grown using the disilane process described in section 2.6.3 (see Fig. 2.9 for SIMS and Fig. 2.12 for XRD rocking curve).

7 nm, i-Si
30 nm, $\text{Si}_{0.996}\text{C}_{0.004}$
400 nm, Si (buffer layer)
Si-substrate

Sequencer Table #0

Step #	Action	Comment
0	CONTROL ON&	Turn on control
1	SCAN(0.3)	Scan simulation
2	SET(SP7,0)	Override power zero
3	SET(SP4,0)	Turn off PID control
4	SET(SP0,0.6)	Zero loop counter
5	SET(DO0,0)	
6	SET(DO1,0)	Hydrogen select off
7	SET(DO2,0)	SiH4 select off
8	SET(DO3,0)	GeH4 select off
9	SET(DO4,0)	B2H6 select off
10	SET(DO5,0)	PH3 select off
11	SET(DO6,0)	Methylsilane (MS) select off
12	SET(DO7,0)	Dichlorosilane (DCS) select off
13	SET(DO8,0)	Disilane (DS) select off
14	SET(DO9,0)	SiH4 inject off
15	SET(DO10,0)	GeH4 inject off
16	SET(DO11,0)	B2H6 inject off
17	SET(DO12,0)	PH3 inject off
18	SET(DO13,0)	DCS/DS inject off
19	SET(AO0,0.21)	Hydrogen 1 slpm
20	SET(DO15,1)	Vac on
21	SET(DO1,1)	Hydrogen on
22	SET(AO1,0)	SiH4 MFC zero
23	SET(AO2,0)	GeH4 MFC zero
24	SET(AO3,0)	B2H6 MFC zero
25	SET(AO4,0)	PH3 MFC zero
26	SET(AO15,0)	DS MFC zero
27	SET(AO6,0.534)	DCS MFC 26 sccm
28	SET(AO7,0)	MS MFC zero
29	SET(AO8,0)	Pressure zero
30	SEQUENCER ON(0.3,1.0)	Start sequence #1

Sequencer Table #1

Step #	Action	Comment
0	SET(SP1,1)	Set layer number
1	SET(SP2, 0.0)	Reset loop counter
2	SEQUENCER ON(0.3,6,0)	Call clean sequence
3	WAITUNTIL(SP2>0.5)	Clean sequence
4	SET(SP2,0.0)	Reset loop counter
5		
6		
7	SEQUENCER ON(0.3,5,0)	Call clean sequence
8	WAITUNTIL(SP2>0.5)	Clean sequence
9		
10	SET(SP5,2.89)	Set T=625
11	SET(SP4,1.0)	Feedback on
12	SET(SP2,0.0)	Reset loop counter
13		
14		
15		
16	SEQUENCER ON(0.3,4,0)	Call alloy layer sequence
17	WAITUNTIL(SP2>0.5)	Alloy layer
18	SET(SP2,0.0)	Reset loop counter
19		
20		
21		
22		
23		
24	RAMP(SP7,-0.4,0.0)	Lamps off
25		
26		
27		
28		
29	SEQUENCER ON(0.3,7,0)	Call shut down
30	WAITUNTIL(SP2>0.5)	Shut down

Sequencer Table #3

Step #	Action	Comment
0	WAIT(60)	
1	SET(AO6,0.54)	DCS 26 sccm
2		
3	SET(DO14,1)	Inject MS
4	WAIT(660)	SiC layer
5	SET(DO14,0)	MS Inject off
6		
7	SET(DO3,0)	Germane select off
8	SET(DO6,0)	MS select off
9	WAIT(15)	Grow Si w/ DS at 625 C
10		
11		
12	SET(DO8,0)	DS select off
13	WAIT(10)	Purge tube of DS & close hand valve
14	SET(DO7,1)	Open hand valve for DCS & Select
15		
16		
17	SET(SP5,3.53)	Set T = 700
18		
19	WAIT(1020)	Cap layer Si w/ DCS
20	SET(DO13,0)	DCS inject off
21		
22		
23	SET(DO7,0)	DCS select off
24		
25	WAIT(5)	Purge
26	SET(SP5,5.5)	Set T = 800 C
27	WAIT(300)	Anneal layer 5 minutes
28		
29	SET(SP2,1.0)	End
30	END	

Sequencer Table #5

Step #	Action	Comment
0	WAITUNTIL(AI24>0.5)	Go for buffer layer
1	SET(AO11,1)	Low P select
2	SET(AO8,0.6)	Pressure 6 torr
3	WAITUNTIL(AI28>0.55)	Stabilize pressure
4	SET(AO7,0.2)	MS flow 0.19 sccm
5	SET(DO6,1)	MS select on
6	RAMP(SP7,-0.4,0.23)	T ~ 800-850 C
7	SET(DO13,1)	Inject DCS
8	WAIT(600)	Buffer layer
9	SET(DO13,0)	Inject DCS off
10	RAMP(SP7,-0.4,0.0)	Lamps off
11	SET(DO7,0)	DCS select off
12	SET(AO6,0)	DCS MFC off
13		
14		
15		
16	SET(AO15,0.5)	Disilane 50 sccm
17	SET(DO8,1)	DS select on
18	WAITUNTIL(AI24>0.5)	Go for SiC layer
19	RAMP(SP7,0.4,0.27)	Lamps on
20	WAIT(5)	Warm-up
21	RAMP(SP7,-0.4,0.16)	
22	SET(AO8,1.0)	Pressure 10 torr
23	WAIT(15)	Stabilize
24		
25		
26	SET(DO13,1)	Inject DS
27		
28		
29	SET(SP2,1.0)	End
30	END	

Sequencer Table #6

Step #	Action	Comment
0	WAITUNTIL(AI24>0.5)	Go for clean
1	SET(AO11,0)	High pressure select
2	SET(AO8,0.25)	Pressure 250 torr
3	SET(AO0,0.817)	Hydrogen 4 slpm
4	WAITUNTIL(AI29>250)	Pressure stabilize
5		
6		
7	SET(SP3,1)	Get cold values
8	WAIT(1)	
9	SET(SP3,0)	
10		
11	SET(DO7,1)	DCS select on
12	RAMP(SP7,0.4,0.27)	Warm-up wafer ~900-1000 C
13	WAIT(120)	Clean 2 min
14	SET(AO8,0.22)	Pump out
15	WAIT(10)	
16	SET(AO8,0.17)	
17	WAIT(10)	
18	SET(AO8,0.12)	
19	WAIT(10)	
20	SET(AO8,0.07)	
21	WAIT(10)	
22	SET(AO8,0.0)	
23	SET(AO0,0.61)	Hydrogen 3 slpm
24		
25		
26		
27		
28		
29	SET(SP2,1.0)	End
30	END	

Publications and Presentations Resulting from this Thesis

Journal Articles

1. M.S. Carroll, C-L Chang, and J.C. Sturm "Complete suppression of boron transient-enhanced diffusion and oxidation-enhanced diffusion in silicon using localized substitutional carbon incorporation," *Appl. Phys. Lett.* **73**, 3695-3697 (1998).
2. M. Yang, C-L. Chang, M. Carroll, and J. C. Sturm, "25nm p-Channel vertical MOSFET's with SiGeC source-drains," *IEEE Elec. Dev. Lett.* **20**, pp. 301-303 (1999).
3. M.S. Carroll, J.C. Sturm, and M. Yang, "Low-temperature preparation of oxygen-and carbon-free silicon-germanium surfaces for silicon and silicon-germanium epitaxial growth by rapid thermal chemical vapor deposition," *J. Electrochem. Soc.* **147**, 4652-4659 (2000).
4. M. Yang, M. Carroll, J.C. Sturm, and T. Buyuklimanli, "Phosphorus doping and sharp profiles in silicon and silicon-germanium epitaxy by rapid thermal chemical vapor deposition," *J. Electrochem. Soc.* **147**, 3541-3545 (2000).
5. M. S. Carroll and J. C. Sturm, "Quantitative Measurement of the Surface Silicon Interstitial Boundary Condition and Silicon Interstitial Injection into Silicon during Oxidation", *Phys. Rev. B.* (submitted)
6. M. S. Carroll, J. C. Sturm, E. Napolitani, D. De Salvador, M. Berti, J. Stangl, G. Bauer, D. J. Tweet, "Diffusion Enhanced Carbon Loss from SiGeC Layers due to Oxidation", *Phys. Rev. Lett.* (submitted)

Refereed Conference Papers

5. M. Carroll, L.L. Lanzerotti, C.C. Chang, and J.C. Sturm, "Silicon epitaxial regrowth in RTCVD for passivation of reactive ion-etched Si/SiGe/Si microstructures," Tech. Prog. Elect. Mater. Conf., 16 (1997).
6. M. Carroll, L.L. Lanzerotti, C.C. Chang, and J.C. Sturm, "Silicon epitaxial regrowth in RTCVD for passivation of reactive ion-etched Si/SiGe/Si microstructures," Tech. Prog. Elect. Mater. Conf., 16 (1997).
7. M.S. Carroll, L.D. Lanzerotti, and J.C. Sturm, "Quantitative measurement of reduction of boron diffusion by substitutional carbon incorporation," Proc. Symp. Mat. Res. Soc., **527**, 417-422(1998).
8. (Invited) J.C. Sturm, M. Yang, C.L. Chang, and M.S. Carroll, "Novel Applications of rapid thermal chemical vapor deposition for nanoscale MOSFET's," Proc. Symp. Mat. Res. Soc. **525**, 273-281 (1998).
9. M.S. Carroll, C.L. Chang, J.C. Sturm, and T. Buyuklimanli, "Complete suppression of oxidation enhancement of boron diffusion using substitutional carbon incorporation," Ext. Abs. Elec. Mat. Conf, 14 (1998).
10. (Invited) J.C. Sturm., M. Yang, M.S. Carroll, and C.L. Chang, "Si_{1-x-y}Ge_xC_y Alloys: An Enabling Technology for Scaled High Performance Silicon-Based Heterojunction Devices," Proc. IEEE Silicon Monolithic Integrated Circuits in RF Systems, 1-2 (1998).
11. M. Carroll, M. Yang, and J.C. Sturm, "Ultrasharp phosphorus profiles in silicon epitaxy by low temperature rapid thermal chemical vapor deposition," Ext. Abs. Electrochem. Soc, p. XX (1999), and in Advances in Rapid Thermal Processing, Electrochem Soc, **99-10**, pp. XX (1999).
12. (Invited) J.C. Sturm, M. Yang, and M.S. Carroll, "Doped and undoped SiGeC layers for Dopant profile control in sub-100 nm vertical MOSFET's," Tech. Dig. Silicon Nanoelectronics Workshop, pp. 56-57 (1999).
13. E. Stewart, M. Carroll, C.L. Chang, and J.C. Sturm, "Boron segregation in polycrystalline Si_{1-x-y}Ge_xC_y alloys," Abs. Elec. Mat. Conf. pp. 18-19 (1999).

14. M. Yang, M.S. Carroll, and J.C. Sturm, "Doped vs. undoped SiGeC layers in sub-100 nm vertical p-channel MOSFET's," Dig. of Int. Conf. Silicon Epitaxy and Heterostructures pp. I5-I6 (1999).
15. M.S. Carroll, J.C. Sturm, and C-L Chang, "Quantitative measurement of reduction of phosphorus diffusion by substitutional carbon incorporation," Proc. Symp. Mat. Res. Soc. **568**, pp. 181-186, (1999).
16. M.S. Carroll, and J.C. Sturm, "Quantitative measurement of interstitial flux and surface super-saturation during oxidation of silicon," Proc. Symp. Mat. Res. Soc. Vol. XX, pp. XX, (2000).
17. (Invited) J.C. Sturm, M.S. Carroll, M. Yang, J. Gray, and E. Stewart, "Mechanisms and applications of the control of dopant profiles in silicon using $\text{Si}_{1-x-y}\text{Ge}_x\text{C}_y$ layers grown by RTCVD," Proc. Electrochem Soc., 2000-9, pp.309-320 (2000).
18. M.S. Carroll and J.C. Sturm, "Quantitative measurement of interstitial flux and surface supersaturation during oxidation of silicon," Symp. Mat. Res. Soc. (April, 2000)

Conference Presentations

19. M. Carroll, L.L. Lanzerotti, C.C. Chang, and J.C. Sturm, "Silicon epitaxial regrowth in RTCVD for passivation of reactive ion-etched Si/SiGe/Si microstructures," Electronic Materials Conference, Ft. Follins, CO, June, 1997.
20. M. Carroll, L.L. Lanzerotti, C.C. Chang, and J.C. Sturm, "Silicon epitaxial regrowth in RTCVD for passivation of reactive ion-etched Si/SiGe/Si microstructures," Tech. Prog. Elect. Mater. Conf., Ft. Collins, CO, June, 1997.
21. M.S. Carroll, L.D. Lanzerotti, and J.C. Sturm, "Quantitative Measurement of Reduction of Boron Diffusion by Substitutional Carbon Incorporation," Symp. Mat. Res. Soc., San Francisco, CA (April, 1998).
22. (Invited) J.C. Sturm, M. Yang, C.L. Chang, and M.S. Carroll, "Novel Applications of rapid thermal chemical vapor deposition for nanoscale MOSFET's," Symp. Mat. Res. Soc., San Francisco, CA (April, 1998).

23. M.S. Carroll, C.L. Chang, J.C. Sturm, and T. Buyuklimanli, "Complete suppression of oxidation enhancement of boron diffusion using substitutional carbon incorporation," Elec. Mat. Conf, Charlottesville, VA (June, 1998).
24. M. Yang, C.L. Chang, M. Carroll, and J.C. Sturm, "40-nm p-channel vertical MOSFET's with SiGeC source-drains," Device Research Conf., Charlottesville, VA (June, 1998).
25. (Invited) J.C. Sturm., M. Yang, M.S. Carroll, and C.L. Chang, " $\text{Si}_{1-x-y}\text{Ge}_x\text{C}_y$ Alloys: An Enabling Technology for Scaled High Performance Silicon-Based Heterojunction Devices," Proc. IEEE Silicon Monolithic Integrated Circuits in RF Systems, Anne Arbor, MI (Sept., 1998).
26. M.S. Carroll, J.C. Sturm, and C.L. Chang, "Quantitative measurement of reduction of phosphorus diffusion by substitutional carbon incorporation," Symp. Mat. Res. Soc., San Francisco, CA (April, 1999).
27. M. Carroll, M. Yang, and J.C. Sturm, "Ultrasharp phosphorus profiles in silicon epitaxy by low temperature rapid thermal chemical vapor deposition," Symp. Electrochem. Soc., Seattle, WA (May, 1999).
28. (Invited) J.C. Sturm, M. Yang, and M.S. Carroll, "Doped and undoped SiGeC layers for Dopant profile control in sub-100 nm vertical MOSFET's," Silicon Nanoelectronics Workshop, Osaka, Japan (June, 1999).
29. E. Stewart, M. Carroll, C.L. Chang, and J.C. Sturm, "Boron segregation in polycrystalline $\text{Si}_{1-x-y}\text{Ge}_x\text{C}_y$ alloys," Electronic. Mater. Conf., Santa Barbara, CA (June, 1999).
30. M. Yang, M.S. Carroll, and J.C. Sturm, "Doped vs. undoped SiGeC layers in sub-100 nm vertical p-channel MOSFET's," Int. Conf. Silicon Epitaxy and Heterostructures. Miyagi, Japan (Sept., 1999).
31. M.S. Carroll and J.C. Sturm, "Quantitative measurement of interstitial flux and surface super-saturation during oxidation of silicon," Symp. Mat. Res. Soc., San Francisco, CA (April, 2000).
32. (Invited) J.C. Sturm, M.S. Carroll, M. Yang, J. Gray, and E. Stewart, "Mechanisms and applications of the control of dopant profiles in silicon using Si_{1-x} -

$y\text{Ge}_x\text{C}_y$ layers grown by RTCVD,” Symp. Electrochem. Soc., Toronto, Canada (May, 2000).